SAPIENZA
UNIVERSITÀ DI ROMA

NUMERICAL SIMULATIONS OF ACOUSTIC RESONANCE OF SOLID ROCKET MOTOR

CANDIDATE
VIVIANA FERRETTI

TUTORS
PROF. MAURIZIO DI GIACINTO
PROF. BERNARDO FAVINI
DEPARTMENT OF MECHANICAL AND AEROSPACE ENGINEERING
SAPIENZA, UNIVERSITY OF ROME

XXIII CICLO

DOTTORATO DI RICERCA IN “TECNOLOGIA AERONAUTICA E SPAZIALE”
DEPARTMENT OF MECHANICAL AND AEROSPACE ENGINEERING
SAPIENZA, UNIVERSITY OF ROME

L'uomo attraversa il presente con gli occhi bendati. Può al massimo immaginare e tentare di indovinare ciò che sta vivendo. Solo più tardi gli viene tolto il fazzoletto dagli occhi e lui, gettato uno sguardo al passato, si accorge di che cosa ha realmente vissuto e ne capisce il senso.

M. Kundera, Gli amori ridicoli

ABSTRACT

The operative life of many large solid rocket motors (e.g. US Space Shuttle SRM, Ariane 5 P230 SRM, Titan SRM, P80 SRM, the five-segment test motor ETM-3) is characterized by the presence of sustained longitudinal pressure (PO, pressure oscillations) and thrust oscillations. Their frequency is close to the first, but sometimes also second or third, acoustic mode frequency of the combustion chamber. Although they do not compromise the motor life, such oscillations represent a point of interest. In case of coupling with the launcher structural modes, they can involve structural failures, interferences and payload damages. Further, thrust oscillations can result in guidance and thrust vector control complications and they can affect the motor performance.

The combustion chamber of an SRM can exhibit a vorticity generation in correspondence of propellant corner, obstacle or boundary layer at propellant surface. Once detached, this vorticity is convected by the flow and it impacts with downstream obstacles. This interaction generates acoustic signal that perturbs the vortex shedding process. The resonant coupling occurs if a combustion chamber acoustic mode is synchronized with the vortex shedding frequency. This condition corresponds to the generation of self-sustained pressure, then thrust, oscillations. These oscillations result from the complex feedback mechanism fed by vortex shedding and acoustic waves, and they are due to the coupling between *fluid-dynamics instabilities* and *acoustic resonant modes*.

Other forms of instabilities can occur in a solid rocket motor, such as combustion instabilities. An aspect that can affect the acoustic coupling is represented by two phase flow effects. In this context, purely acoustic coupling is considered, and these phenomena are neglected.

The acoustic coupling simulation requires models capable to describe both the acoustic and the vortical waves, including their interactions. To achieve a complete characterization of motor instability risk, it is important to obtain an accurate reconstruction of both oscillation amplitude and frequency. A complete description can be obtained by full numerical simulations, but CFD analysis require high computational costs and times, and present difficulties concerning the model definition. Usable for particular cases and documented situations, the obtained results are not so accurate. The fundamental char-

acteristics that make a reduced-order model a useful tool, are the reduced computational requirement and the possible improvement of relevant process understanding.

Rossiter [90, 91] developed a model that describes the aeroacoustic coupling as a feedback loop. Current calculations of SRM stability are based on a simple first-order perturbation solution. The classical approaches used in this context are the acoustic balance method, given in practical form by Culick [27], and the most complete Flandro's method [45]. Such methods, capable to predict the motor tendency to become unstable, do not provide informations on the instability level and on the system triggering. Other simplified models have been proposed by Howe [55], Hirshberg and Hulshoff [53] that analyzed the vortex sound production.

A particular attention has to be turned to the one-dimensional reduced order models derived by Matveev [78] and Jou & Menon [63, 81]. Matveev's model is based on a ODE system and it describes the acoustic modes excitation, accounting for the acoustic feedback on the vortex shedding. Jou and Menon developed a model for the evaluation of the coupled-mode oscillation frequency.

The main idea followed in this research is proposed by prof. B. Favini and F. Serraglia; their idea is the use a quasi-one dimensional model, for the flow field evolution in a solid rocket motor, where the vorticity dynamics is also described by a Q-1-D model. As far as we know, this is the first time this kind of modeling has been adopted in order to simulate aero-acoustical phenomenon. Several exploratory studies have been performed in the last few years on their approach, but the model reached a complete definition only in this doctoral thesis.

In the present work, the quasi-1D reduced order model *AGAR* (Aerodynamically Generated Acoustic Resonance) is developed in the aim of simulating SRM internal flows, and consequently pressure and thrust oscillations.

A model opted of simulating internal ballistics requires to be constituted of several sub-models as: *a)* grain burn back model for the propellant grain surface evolution with time (GREG, Grain REGression model) *b)* flow field evolution model (SPINBALL, Solid Propellant rocket motor INternal BALListics model) *c)* aero-acoustic simulation model (POX, it's not an acronym).

In order to validate the AGAR model and to verify its capability and its main characteristics, a first test case considered in this work is a cold flow in an axisymmetric ramjet combustor. This simple case allows a detailed analysis of the interaction between vortex dynamics and acoustic waves.

Then the model has been applied to a real case, represented by the P80 SRM, the first stage of the new European small launcher Vega. During its qualification and demonstration static firing tests, the motor has exhibited four different phases of pressure oscillations during the whole operative life.

The present Ph.D. dissertation is organized as follows.

CHAPTER 1 An overview of pressure oscillation phenomenology in a solid rocket motor is highlighted. To understand the origin of pressure oscillations, a presentation of the basic phenomena characterizing the aeroacoustic coupling is provided. The aeroacoustic resonance characterization is completed with the description of Rossiter's feedback loop model and its possible interpretation. Some notes about flute mode behavior, lock-in phenomenon and combustion instabilities are given. The vortical structure definition and identification criteria are also presented.

CHAPTER 2 The state of the art of the most important methods for aeroacoustic modeling are presented. After a general historical summary, the methods are described in terms of their fundamental features. Generalities are given about the full numerical simulations. Then Matveev's and Jou and Menon's reduced order models are introduced and analyzed.

CHAPTER 3 An overview of SRM aeroacoustic mathematical model is provided, with special care in the derivation and analysis of the vorticity equation. A description of *AGAR* quasi-one dimensional model is presented.

CHAPTER 4 The validation test case here presented is the simulation of cold flow in an axisymmetric combustor. A comparison with Jou and Menon's results is provided. The behavior and main characteristics of AGAR model are described, and an analysis of the interaction between vortex dynamics and acoustic waves is obtained.

CHAPTER 5 The simulation of the aeroacoustic phenomena of P80 solid rocket motor, first stage of Vega launcher, by AGAR model is considered. The experimental data and the numerical results are described, analyzed and compared.

CONTENTS

LIST OF FIGURES

NOMENCLATURE

$\mathbf{I}$	unit tensor
$\mathbf{n}$	normal vector
$\mathbf{q}$	heat flux
$\mathbf{q}_d$	dipole strength
$\mathbf{T}$	stress tensor
$\mathbf{u}$	velocity vector
$\mathbf{x}$	position vector
$\tilde{f}_{ab}$	acoustic balance source term
$\tilde{h}_{ab}$	acoustic balance source term
a	sound velocity
A_p	port area
B	integration constant
c_f	body force coefficient for Matveev model
c_p	specific heat at constant pressure
c_q	volumetric source coefficient for Matveev model
c_v	specific heat at constant volume
D	combustion chamber diameter
D_h	hydraulic diameter
E	total internal energy
e	total internal energy per unit of mass
F	body force per unit of mass

f	frequency
G	general variable
H	total enthalpy
h	enthalpy per unit of mass
IMF	intrinsic mode function
k	heat conductivity
k_R	ratio of vortex convection velocity and freestream velocity
k_n	wave number
L	combustion chamber length
L/D	length to diameter ratio
l_i	stand-off distance, distante between the shear layer initiating point and the impingement point
l_{vs}	distance on which the vortex accumulates vorticity, distance between two successive vortices
l_{vs}	vortex dimension
M	Mach number
m	stage number, number of vortices between the stand-off distance l_i
$m(t)_n$	empirical mode decomposition mean value
M_{inj}	surface injection Mach number
n	acoustic mode number
p	pressure
P_b	burning perimeter
P_c	comnustion perimeter
Q	volumetric source term per unit of volume
q_m	monopole strength
R	combustion chamber radius, channel radius

r	radius
r_b	propellant grain burning rate
r_k	empirical mode decomposition residue
Re	Reynolds number
S	surface
s	entropy per unit of mass
T	period, temperature
t	time
u, v, w	cartesian velocity component
u_R	fluid particle rotation velocity
V	volume
x, r, θ	cylindrical coordinates
x, y, z	cartesian coordinates
x_{obs}	obstacle position point
x_{vs}	vortex generation point
$\wp$	average acoustic power

Greek

α	Rossiter's phase delay factor
α_{cav}	cavity model calibration parameter
β	amplification coefficient
$\boldsymbol{\omega}$	vorticity vector
$\boldsymbol{\Psi}$	stream function
$\boldsymbol{\tau}$	viscous stress tensor
Δ	dilatation field
δ	delta function

δ_t	shear layer momentum thickness
η	dynamic viscosity
η_n	time varying amplitude of the mode
Γ	circulation
γ	gas constant
λ	cinematic viscosity
μ	dynamic viscosity
Ω	POX model vorticity variable
ω_f	angular frequency
ϕ	scalar potential
π	vortical fluctuation profiles across the shear layer for pressure in hydrodynamic stability analysis
ψ	stream function
ψ_T	specific Taylor constant
ψ_n	mode shape
ρ	density
σ	characteristic vortex dimension
τ	vortical fluctuation profiles across the shear layer for x-velocity in hydrodynamic stability analysis
θ	Hilbert phase function
ε	perturbation parameter
φ	vortical fluctuation profiles across the shear layer for y-velocity in hydrodynamic stability analysis
ξ	spatial variation of nondimensional hydrodynamic solution
ξ_p	partial spatial variation of nondimensional hydrodynamic solution for Flandro's method
ξ_{tot}	total spatial variation of nondimensional solution for Flandro's method

ζ	nondimensional hydrodynamic vorticity, calibration parameter for vorticity equation source term

Superscripts and Subscripts

$'$	fluctuating, acoustic component
$\bar{\ }$	mean component
$\tilde{\ }$	spatial variation of an unsteady component
a	acoustic
BL	relative to acoustic boundary layer
c	relative to combustion chamber
cav	cavity
CC	relative to combustion phenomenon
d	dump combustor
FT	relative to flow turning
h	hydrodynamic
ig	igniter gases
in	inlet duct
inj	injection
N	relative to the nozzle
n	relative to acoustic mode number
NC	relative to nozzle convective part
NR	relative to nozzle radiation part
p	propellant combustion gases
s	relative to cavity or submergence region
TP	relative to two-phase flow
vs	relative to vortex or to vortex shedding phenomenon
0	relative to reference state

ACKNOWLEDGEMENTS

The present activities were partially financed by ESA/ESRIN.

The authors would like to thank Avio, Europropulsion, CNES, ELV and ESA. The development and production of Vega SRMs are mainly due to AVIO Group S.p.A. (Colleferro Factory). Avio is prime contractor for the P80 SRM with a delegation to Europropulsion, France. The Program is managed by CNES/ESA.

PUBLICATIONS

SOME results of this doctoral research have appeared previously in the following publications:

PRESSURE OSCILLATIONS SIMULATION IN P80 SRM FIRST STAGE VEGA LAUNCHER, *V. Ferretti, B. Favini, E. Cavallini, F. Serraglia and M. Di Giacinto*, Accepted to: Joint Propulsion Conference & Exhibit, 2011, San Diego

VORTEX-SOUND GENERATED PRESSURE OSCILLATIONS SIMULATION IN INTERNAL FLOW BY MEANS OF Q-1D MODEL, *V. Ferretti, B. Favini, E. Cavallini, F. Serraglia and M. Di Giacinto*, EUCASS, the European Conference for AeroSpace Sciences, 2011, San Petersburg

NUMERICAL SIMULATIONS OF ACOUSTIC RESONANCE OF SOLID ROCKET MOTOR, *V. Ferretti, B. Favini, E. Cavallini, F. Serraglia and M. Di Giacinto*, 46th AIAA/ASME/SAE/ASEE Joint Propulsion Conference & Exhibit, 25-28 July 2010, Nashville, TN

QUASI 1-D MODELING OF SRM AEROACOUSTICS, *V. Ferretti, B. Favini, E. Cavallini, F. Serraglia and M. Di Giacinto*, Space Propulsion Conference 2010, San Sebastian, Spain

REPORTS

SOME results of this doctoral research have appeared previously in the following reports:

POX Q-1-D MODELING OF SRM AEROACOUSTIC, *Ferretti, V. and Favini*, Internal Report for ESA-ESRIN, Frascati, Italy, July 2009

1

SOLID ROCKET MOTOR AEROACOUSTICS

SOME solid rocket motors exhibit pressure oscillations during their operative life. After a general overview about the pressure oscillation issue, a description of the basic phenomena characterizing the aeroacoustic coupling is here provided, and the aeroacoustic resonance characterization is completed by the description of Rossiter's feedback loop model and its possible interpretation. Some notes about flute mode behavior, lock-in phenomenon and combustion instabilities are given. The vortical structure definition and identification criteria are also presented.

1.1 SOLID ROCKET MOTORS

A simple scheme of a generic solid rocket motor (SRM) and its fundamental components is presented in fig. 1.1.

The external motor structure is called *case*, it contains the propellant charge and serves as highly loaded pressure vessel. It's either made of metal or composite materials; the surfaces directly exposed to hot gases are protected by thermal protections or insulation layers.

The *grain* is the solid propellant charge that contains all the chemical species necessary for combustion; the central cavity is the port cavity, and the grain configuration determines the combustion chamber geometry. The main parameter characterizing the motor combustion chamber is the length (L) to diameter (D) ratio. The presence of slots, grooves, holes, or other geometric features determines different burning surface configuration; the propellant mass flow rate and the combustion chamber pressure depend, other on the burning rate, on the grain burning surface, so that by modifying the grain shape it is possible to obtain the desired pressure and thrust behavior. For this reason, very complex grain shapes are designed, and often three-dimensional regions are used. The most com-

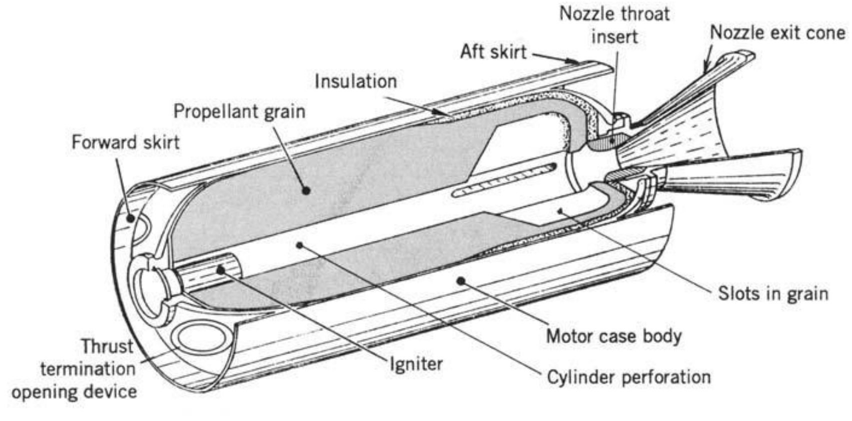

Figure 1.1: Generic SRM scheme (figure from: *Rocket Propulsion Elements*, G. P. Sutton and O. Biblarz).

mon three-dimensional regions are star-shaped or *finocyl*, where finocyl stands for fins on cylinder. The three-dimensional regions are generally placed at the forward end, head end, or at the aft end of the combustion chamber.

The *igniter* is a pyrogen charge, electrically activated, that provides the necessary energy for the combustion start. The grain ignition starts on the exposed inner surface, where the igniter hot gases impinge on the propellant surface. As the propellant burns out, the grain surface regresses along the normal direction to the surface itself, causing the grain port area increase.

The propellant combustion produces hot gases ($\sim$ 3500 K) that flow toward the aft end of the motor; they are then accelerated and ejected by the *nozzle*. To resist high temperatures and erosion, the nozzle is made out of high temperature materials, such as graphite or ablative materials. A nozzle partially included in the combustion chamber determines the presence of the *submergence region*, a volume delimited by the grain and the nozzle convergent part.

A *seal*, typically placed in the nozzle throat section, protects the combustion chamber from the external environment; the diaphragm is removed when a prescribed differential pressure is reached.

The whole operative life of a solid rocket motor (overall combustion time) can be divided in three different phases: *Ignition Transient*, *Quasi Steady State* and *Tail Off* (fig. 1.2).

1.2 Solid rocket motor pressure oscillations

Solid rocket motors having large length (L) to diameter (D) ratio (i.e. $L/D > 9-10$, as US Space Shuttle SRM [47], Ariane 5 P230 SRM [93], Titan SRM [16, 34] and the five-segment

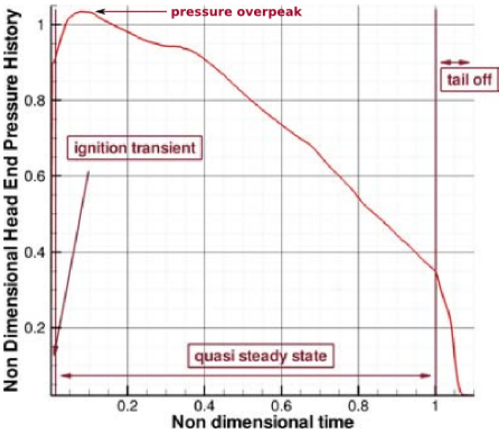

Figure 1.2: Head-end pressure time history

test motor ETM-3) exhibit sustained pressure and thrust oscillations along the whole operative life.

Even if each motor shows different timing and duration of the oscillating phase, the pressure oscillations are described by some common features. The pressure fluctuations are generally not threatening for motor life but, in spite of this, the oscillations represent a point of interest. Their frequency is close to the first, but possibly also second or third, acoustic mode of the combustion chamber. They can involve interferences and payload damages as well as launcher and motor structural failures. Further, they can affect the motor performance and can imply guidance and thrust vector control complications. In the last part of its flight, the launcher is almost completely unloaded and the oscillations generate high levels of acceleration. The pressure oscillations are of the order of about 0.5 % of the mean value; due to the transfer function between pressure and thrust, the order of the thrust oscillations is about 5 % of the mean value. Indeed, the transfer function is variable with time and it increases with the time evolution.

The pressure oscillations result from the complex feedback mechanism fed by vortex shedding and acoustic waves, and are due to the coupling between *fluid-dynamics instabilities* and *acoustic resonant modes*.

1.3 Fluid-dynamics instabilities and vortex shedding

The solid rocket motors that typically show pressure oscillations are characterized by segmented grain, propellant corners and inhibitor rings. Each corner or protruding object (i.e: inhibitor rings) can be a point for fluid-dynamics instabilities origin and a vorticity production can occur if the generated shear layer becomes unstable. Therefore, the presence of an obstacle or of propellant surface discontinuities can involve vorticity generation [107, 106].

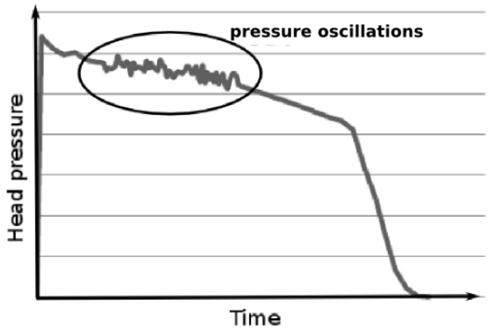

Figure 1.3: Pressure oscillations of a solid rocket motor.

Culick underlines the presence of a shear flow region adjacent to a surface with radial mass injection [27]; in a solid rocket motor such addition is related to the grain regression. In the shear region, the mass velocity vector is turned from radial to axial direction, as shown in fig. 1.4. This shear flow can generate vortical structures close to the surface: the profile is unstable and any perturbation will result in a breakdown into coherent vortical structures [104, 34, 18].

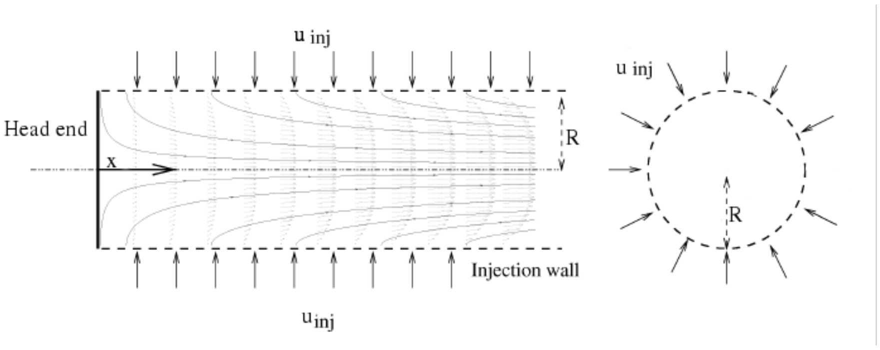

Figure 1.4: Sketch of a cylinder with radial mass addition.

In conclusion, three different kinds of vortex shedding phenomena can be identified in a solid propellant rocket motor: parietal, obstacle and corner vortex shedding. A sketch can be seen in fig. 1.5. The vortex shedding process is strongly affected by the presence of an external acoustic field, so that the acoustic waves provide a control signal for the hydrodynamic instability.

PARIETAL VORTEX SHEDDING (PVS) The parietal vortex shedding is due to purely hydrodynamical instability of the velocity profile. Vortical structures are generated near a boundary through which a flow enters a volume [29, 105, 64]; the boundary does not

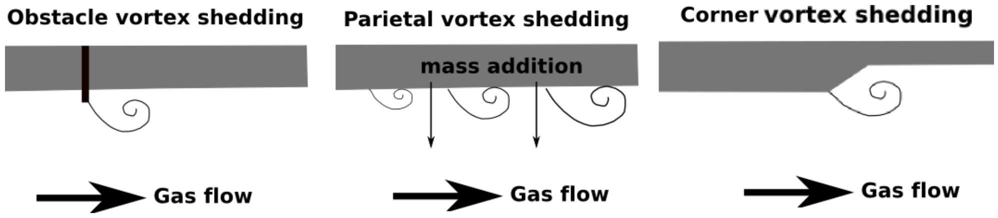

Figure 1.5: Vortex shedding phenomena.

present any particular geometrical feature. The transversal velocity component plays a major role in the instability mechanism [64].

This mechanism is related to Taylor/Culick's flow instability; these flows become unstable for sufficiently long distance along the combustion chamber (L/D > 5, a value almost independent from Reynolds number), so that it can be typically observed in large SRM. PVS is represented by the generation, along a wall, of vortical structures that grow spatially and interact with acoustic modes.

Corner vortex shedding (CVS) This kind of vortical structure is produced by a very unstable profile generated by the presence of a propellant sharp edge. The propellant corners determine the existence of highly sheared regions, and the shedding process is related to the Kelvin-Helmholtz instability.

Obstacle vortex shedding (OVS) In this mechanism the vortices are generated by a jutting obstacle (inhibitor rings, annular restrictors, ...) that can generate highly sheared flows, and consequently periodic vortex shedding. As the CVS, the obstacle vortex shedding is also related to the Kelvin-Helmholtz instability.

Once generated by one of the three mechanisms previously mentioned, the vortical structure is convected by the flow. Traveling downstream, the vortex is stretched and looses its energy of rotation [107, 82, 6].

During their movement, adjacent vortices tend to combine in a single vortex (*vortex pairing phenomenon*) [82, 99, 107, 74, 76]. This phenomenon is reduced by high values of dynamic viscosity, that also determine a more regular vortex shedding mechanism [65].

1.4 Vortex-obstacle interaction

Moving downstream in the combustion chamber, a vortex interacts with each obstacle and geometrical variation, such as inhibitor rings or annular restrictors. At the end, once reached the aft end of the combustion chamber, the vortex impacts on the nozzle nose.

Each time a vortex interacts with an obstacle, it generates an acoustic radiation; this sound production is a potential source for the observed pressure oscillations [35, 104, 34].

The velocity field can be considered composed by a potential (irrotational) and a solenoidal field (par. 3.2). The unsteady part of the potential flow component defines the *acoustic field* [52]. As indicated by Howe's vortex sound theory [55], the generated sound is proportional to the vortex convection velocity ($\mathbf{u}$), to the acoustic velocity ($\mathbf{u}'$), to the angle between $\mathbf{u}$ and $\mathbf{u}'$, to the vortex intensity and to the vorticity ($\boldsymbol{\omega}$) distribution close to the obstacle [6, 59]. At low Mach numbers, the average acoustic power $\wp$ can be expressed as:

$$\wp = -\bar{\rho}\,\langle \int_V (\,\boldsymbol{\omega} \times \mathbf{u}\,) \cdot \mathbf{u}' dV \rangle \tag{1.1}$$

where ρ is the density. A description of vortex-sound theory is presented in par. 2.3.

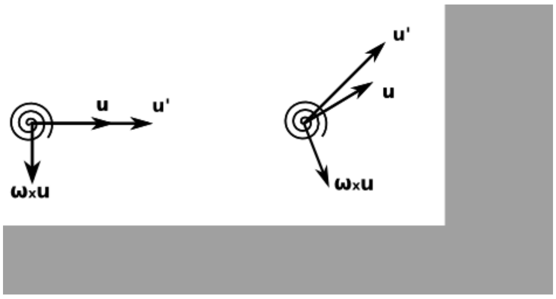

Figure 1.6: Vortex interaction with an obstacle (adapted from: [60]).

The amplitude of the sound production increases with the vortex circulation and the flow Mach number, while it decreases with the vortex height with respect to the obstacle [60]. The precise form of the sound signal is determined by the vorticity distribution and by the nozzle geometrical configuration [60]. Although different nozzle designs generate different amplitudes, the excitation of the same acoustic mode is obtained [4]. In particular, the submergence region increases the level of the generated sound, and acts as a pressure fluctuation amplifier. The nozzle cavity induces large velocity fluctuations at the cavity inlet, and this causes vortex oscillations. The pressure oscillation level increases almost linearly with the nozzle cavity volume [2, 5].

While a *monopole source* radiates sound equally in all directions, a *dipole source*, two monopole sources of equal strength but opposite phase, radiates sound along two preferential directions. The dipole source corresponds to the stronger kind of radiator. When a vortex interacts with an obstacle, there is an energy transfer from the vortex to the acoustic field, and it is described by a dipole source.

Two opposite dipoles correspond to a *quadrupole source*; the sound is radiated along four directions, but it is null at points equidistant from adjacent opposite monopoles. A quadrupole is a weak radiator, and it represents the sound generation due to the mere presence of a vortex.

A *pseudo-sound* production, that does not propagate and that is described by a quadrupole source, is associated to the vorticity [88]. The acoustic waves generated by the pseudo-sound only weakly interact with the motion of the vortical structures [45]. The pseudo-sound is the dominant component close to the vortex, but it rapidly decays and it becomes negligible if compared to the sound generation due to vortex interaction with an obstacle.

1.5 AEROACOUSTIC COUPLING

The acoustic resonance of a solid rocket motor results from a complex feedback mechanism that involves the interaction of *fluid-dynamics instabilities* and *acoustic resonant modes*. A scheme of the resonant coupling is shown in fig. 1.7. The hydrodynamic instability of the shear flow generates vortical structures that, once detached, are convected by the flow and interact with each obstacle in the combustion chamber (inhibitor rings, annular restrictors, nozzle,...). Each interaction determines an acoustic field excitation and a possible acoustical triggering of shear flow instability.

The vortex shedding is characterized by the vortex shedding frequency f_{vs}. The distance between the vortex generation point and the impingement point is defined *stand-off distance* l_i. The vortices are an independent source of acoustic waves and their occurrence merely excites the acoustic disturbance. The oscillation frequency corresponds to a free mode frequency[1]; it strongly depends on the speed of sound, and only weakly on the convective speed.

The acoustics of the combustion chamber is characterized by the acoustic frequency f_a:

$$f_a = (2n-1)\frac{a}{2L} \tag{1.2}$$

where n is the acoustic mode number, a is the speed of sound and L is the chamber length L^2. Each cavity in the combustion chamber is described by a proper acoustic frequency, that is defined as:

$$f_{a,cav} = (2n-1)\frac{a}{2l_i} \tag{1.3}$$

When a vortical disturbance couples at the boundary with the acoustic disturbance, the vortex shedding frequency is synchronized with the chamber acoustic modes ($f_{vs} = f_a$) and the *resonant coupling* occurs, leading to self-sustained *coupled-mode oscillations*. In this case, the duct acts like a resonator through its natural eigenmodes and the pressure fluctuation amplitude attains a maximum value. The coupled-mode frequency strongly depends on the vortical disturbance velocity, and consequently on the flow Mach number.

The aeroacoustic coupling is possible if the acoustic frequency lies in the range of the shear layer unstable frequencies. This aspect identifies the shear layer as a broad band amplifier that naturally tunes to available frequencies; the shear layer contraction, the

---

[1] For this kind of oscillations the sonic throat acts like a nodal point.

[2] The acoustic frequency of a tube with a single closed end can be expressed as $f_a = (2n-1)\frac{a}{4L}$, while for a tube with both ends closed or open it is $f_a = (2n-1)\frac{a}{2L}$.

time variation of shear-layer thickness, acts both as an amplifier and a frequency selector. In case of coupling, the acoustic field perturbs the shear layer, that modifies its thickness and tunes its frequency to the acoustic modes. In this case, an amplification of the velocity fluctuations in the shear layer occurs, and large-scale vortical structures are generated.

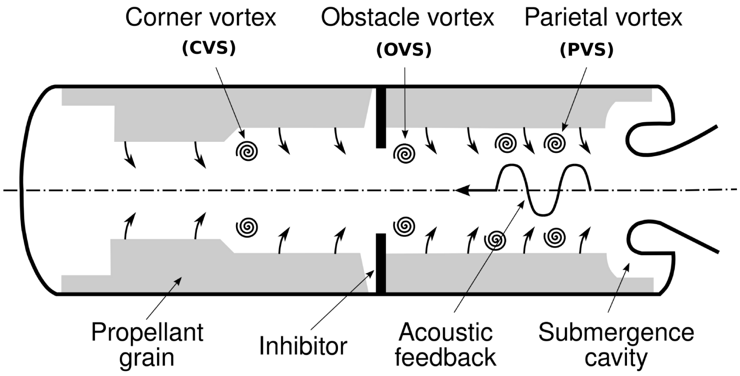

Figure 1.7: Aeroacoustics of a solid rocket motor (modified by [6]).

The resonant coupling could not be sustained without the presence of an obstacle downstream of the vortex generation point [30]. The presence of the obstacle is necessary for the energy transfer, described by a dipole source production, from the impinging vortex to the acoustic mode [92, 47], attained by the production of a dipole source.

As a vortex exchanges energy with the acoustic wave at the *impingement point*, the acoustic mode feeds back this energy to the vortical wave (shear flow instability) at the *receptivity point*, corresponding to the vorticity generation point [101, 50]. The receptivity of the shear flow to external modulation closes the loop with a new vortex generation.

The vortex generation process can be aided by the relative displacement between the vortex shedding point and the acoustic nodes. The vortex shedding triggering by the acoustic mode is more effective if the detachment point corresponds to an acoustic pressure node [16, 35]. It is possible to describe a node as a point where a constant value is maintained; each point where the maximum or minimum values are alternated corresponds to an *antinode*, respectively positive and negative. In fig. 1.8 the first three acoustic modes of a closed tube are shown. As it can be noted, an acoustic pressure node corresponds to an acoustic velocity antinode. A solid rocket motor can be only partially assimilated to a closed tube. Indeed, because of the sonic throat section, the combustion chamber end section is only characterized by a partial reflection.

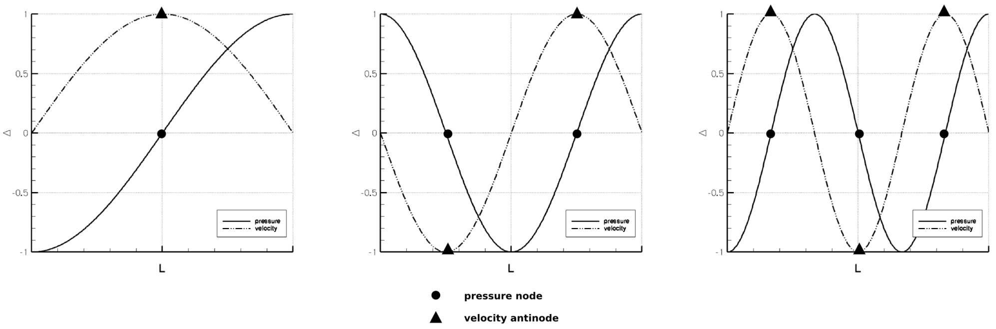

Figure 1.8: Acoustic modes for a closed tube.

1.6 ROSSITER'S MODEL

The first description of the *resonant oscillation* has been developed by Rossiter [90, 91]. He describes the aeroacoustic coupling as a feedback loop (fig. 1.9) whose fundamental steps are:

- *hydrodynamic instability of the shear flow*: vortical structures are generated by an unstable shear layer or surface instability; once detached, they are convected downstream by the flow
- *vortex interaction with an obstacle* (inhibitor rings, annular restrictors, nozzle,...)
- *acoustic source*: the vortex impingement on an obstacle generates an acoustic signal
- *acoustical response of the combustion chamber* and *acoustical triggering of shear flow instability*: the acoustic signal, reaching the shear layer initiation point, perturbs it and generates a new vortex
- *new vortex generation*: the new vortex rolls up, growths and travels downstream closing the loop

The feedback loop is described by two loops, the first (*Loop1*) related to the vortex shedding and the second (*Loop2*) to the acoustics. As previously seen, the resonant coupling occurs when the two loops are coupled ($f_{vs} = f_a$).

It is possible to distinguish between *deep cavities* and *shallow cavities*. A cavity of length l_i and diameter d is described by its *aspect ratio* l_i/d; if $l_i/d < 2$ a cavity is defined deep, while for $l_i/d = 4 \div 10$ it is a shallow cavity.

Rossiter proposes a semi-empirical formula for the prediction of the frequency peaks in high subsonic compressible flows, over deep cavities and for a flow characterized by $Re \propto 10^6$. He states that the type of flow pattern occurring in a cavity depends on its l_i/d ratio, while it is only weakly dependent on the Reynolds number.

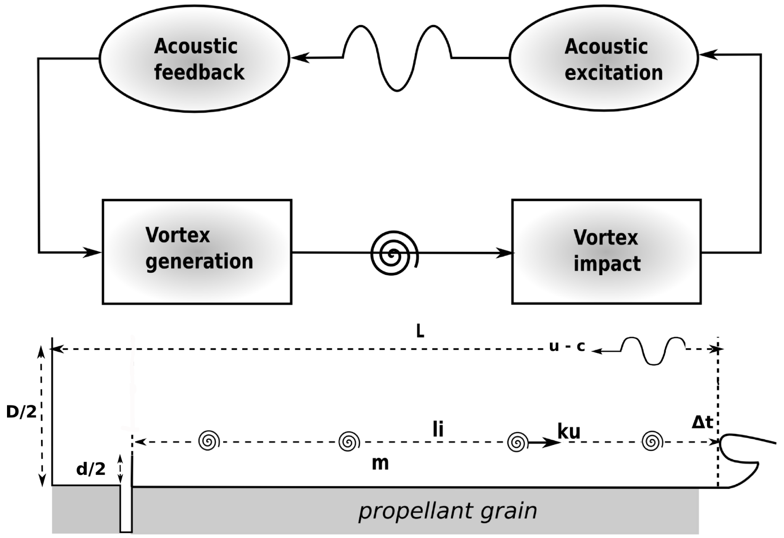

Figure 1.9: Aeroacoustic coupling.

The *stage number* (m) is defined as the number of vortices in a cavity of length l_i. Each vortex is convected with a velocity (u_{vs}) corresponding to a fraction of the freestream velocity (u).

The impingement of a vortex on the trailing edge of the cavity generates an acoustic pulse. The vortex shedding period (T_{vs}) corresponds to the sum of the vortex convection time, the pressure pulse propagation time and the time delay between the vortex collision and the acoustic pulse generation, all divided by the number of vortices.

Mathematically the feedback loop can be expressed as:

$$m\,T_{vs} = \frac{l_i}{k_R\,u} + \frac{l_i}{(a - u)} + \Delta t \tag{1.4}$$

where:

- k_R is a dimensionless empirical constant representing the ratio between the vortex convection velocity and freestream velocity:

$$u_{vs} = k_R\,u \tag{1.5}$$

- $l_i/(k_R u)$ is the vortex convection time, the time between vortex release and vortex impingement
- $l_i/(a - u)$ is the propagation time of the pressure pulse, the time for the acoustic signal, generated by vortex impingement, to reach the shear layer initiation point
- Δt is the time delay between vortex impingement and acoustic signal generation.

Introducing a *phase delay factor* α, a dimensionless empirical constant, the time delay Δt can be expressed as:

$$\Delta t \;=\; \alpha\, T_{vs} \tag{1.6}$$

The vortex shedding frequency, which is the inverse of vortex shedding period, can be obtained from eq. 1.4:

$$f_{vs} \;=\; \frac{u}{l_i}\left(\frac{m \,-\, \alpha}{\frac{M}{1-M} \,+\, \frac{1}{k_R}}\right) \;=\; \frac{u}{l_i}\left(\frac{m - \alpha}{M \,+\, \frac{1}{k_R}}\right) + \circ(M^2) \tag{1.7}$$

where the Mach number $M = u/a$ is introduced.

Rossiter obtains a set of values that provides a good estimate, with respect to the experimental data, for a large range of deep cavities: $k_R = 0.61 - 0.66$ and $\alpha = 0.25$ [90]. If a shallow cavity is considered ($L/D = 4$), the values are: $k_R = 0.57$ and $\alpha = 0.25$. For a shallow cavity ($L/D = 10$), the phase delay factor is $\alpha = 0.58$.

Rossiter's model underlines the coupling between the fundamental acoustic mode and the vortex shedding. A mean flow velocity decrease corresponds to a vortex shedding frequency decrease, until it is decoupled from the acoustic mode. At this point, the coupling condition is achieved with an increase of the number of vortices over the length l_i (m), corresponding to a shedding frequency increase.

Rossiter's equation, a quite simple model, is rather successful in predicting resonant frequency values, while it does not give any information about the oscillation amplitude. Although it is not fully predictive, it is quite useful to analyze firing test experimental data.

1.7 Flute mode behavior and lock-in

The acoustic resonance condition corresponds to a synchronization of the vortex shedding and the acoustic modes frequency ($f_{vs} = f_a$). While the acoustic frequency is a motor characteristic, the shedding frequency depends on the internal flow evolution.

Solid propellant motors are in general characterized by a decrease of the mean flow velocity with time evolution. Several theoretical and experimental studies point out the typical behavior shown in fig. 1.10. Once attained a resonance configuration, the resonant frequency decreases with the grain burn back, because of the reduction of the mean flow velocity. When moved away from resonant conditions, a frequency jump occurs and the system brings back itself to a different resonant configuration, characterized by a different number of vortices [44, 68, 107, 87, 100]. As visible in fig. 1.10, the oscillations appear grouped in tracks, that exhibit decreasing frequencies and sudden jumps around the acoustic frequency.

The frequency decrease with the burn time is an indication of a phenomenon depending on the axial flow velocity. The frequency jumps represent a system adjustment to the

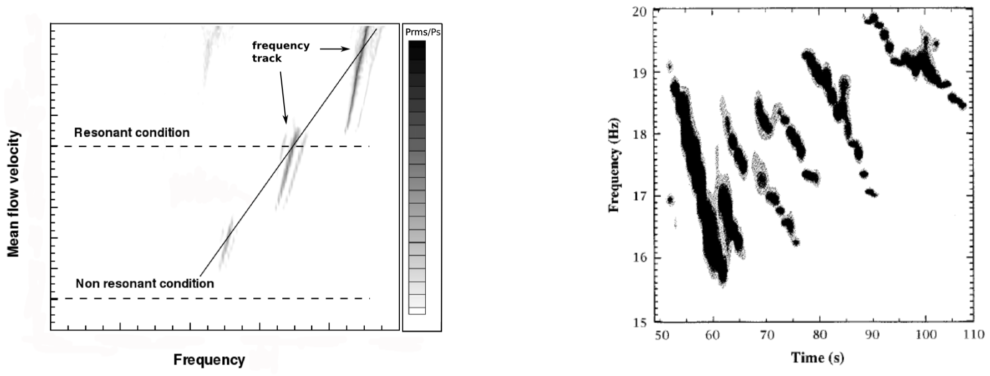

(a) Velocity vs Frequency (figure from: [6])

(b) Frequency vs Time (QM3 static firing test, figure from: [34])

Figure 1.10: Flute mode behavior.

changing conditions in the combustion chamber. When the vortex shedding frequency f_{vs} falls too far away from the acoustic frequency f_{ac}, an increase in the number of vortices occurs to bring back the driving frequency in the acoustic range. This is a typical *flute-mode behavior* [103, 48] and it is considered as an evidence of the hydrodynamic origin of the oscillations. A measure of the frequency shift associated with variations of the mean flow velocity, established that the ratio f_{vs}/u remains constant [16].

The attraction of the vortex shedding frequency to the acoustic frequency and the shift of the shedding frequency, due to the change of the mean flow velocity, describe the *lock-in phenomenon*. The lock-in represents the adjustment, in order to remain in a resonant configuration, of the *Loop 1* to the frequencies of the *Loop 2*.

1.8 A Rossiter's model interpretation

Delprat [31] proposes an *a posteriori* analysis of Rossiter's equation, eq. 1.7, based on a signal processing interpretation. This analysis combines a nonlinear distortion and an amplitude modulation.

The spectral analysis of the unsteady pressure signal measured inside a cavity, of length l_i and diameter d, reveals the presence of a sequence of peaks. Such peaks do not correspond to the cavity acoustic mode frequencies, defined as:

$$f_a = (2n-1)\frac{a}{4l_i} \tag{1.8}$$

The spectrum of the signal appears non harmonic, and consecutive peaks are separated by interval of constant frequency value (fig 1.11).

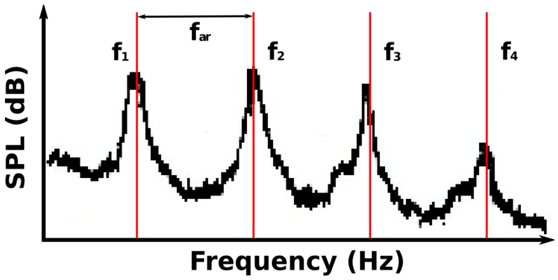

Figure 1.11: Delprat spectrum interpretation (from: [31]).

The interval between two consecutive frequency peaks corresponds to the *fundamental aeroacoustic loop frequency*:

$$f_{ar} = f_{vs}^{n+1} - f_{vs}^{n} = \frac{1}{T_{vs}} = \frac{u}{l_i}\left(\frac{1}{M + \frac{1}{k}}\right) \tag{1.9}$$

Rossiter introduces a phase delay factor (α) to express the time delay between vortex impingement and acoustic signal emission as a function of vortex shedding period T_{vs} (par. 1.6). If α is defined as a *frequency ratio* instead of a phase lag, it is possible to define a frequency f_b, function of the fundamental aeroacoustic loop frequency f_{ar}, as:

$$f_b = \alpha f_{ar} \tag{1.10}$$

The vortex shedding frequency is then expressed as:

$$f_{vs}^{n} = (m - \alpha) f_{ar} = m f_{ar} - f_b \tag{1.11}$$

This expression suggests that the spectrum predominant peaks modeled by Rossiter, represent the difference between the fundamental frequency of the physical phenomenon (f_{ar}) and a lower frequency (f_b). The generation of such components is related to the existence of a nonlinear process. The signal appears to be modeled by a two-step process: first a nonlinear distortion of a wave with a frequency f_{ar}, then an amplitude modulation of the resulting signal by a wave with a frequency f_b. The spectral content corresponds to a mixing of the aeroacoustic frequency loop (f_{ar}) and a sequence of Rossiter modes.

It has to be noted that the fundamental frequency f_{ar} is not a dominant peak and it is generally not visible, as indicated by eq. 1.11 and showed in fig. 1.11.

As seen in par. 1.6, the vortex convection velocity is a fraction, represented by the parameter k_R, of the mean flow velocity ($u_{vs} = k_R u$). Different k_R values can produce the same spectral content despite a significant frequency shift on some modes (eq. 1.11).

1.9 VORTEX DEFINITION AND IDENTIFICATION

Coherent vortical structures are generally defined as bounded regions of flow with some common properties. These common features are not always the same and they do not appear with regularity in space and time. Because of this variability, different vortex definitions and identification criteria have been developed.

Rossiter used the term vortex to indicate a "region of intense vorticity resulting from the local rolling up of the shear layer separating the cavity from the external stream" [90].

Several definitions are related to vortices in terms of the streamlines that characterize these structures. Lugt presented a definition of vortical as "the rotating motion of a multitude of material particles around a common center [72]. Robinson followed an analogous idea declaring that a vortex "exists when instantaneous streamlines mapped onto a plane normal to the vortex core exhibit a roughly circular or spiral pattern" [89]. The same definition was adopted by Anthoine, that described the vortex as "a region where the instantaneous flow is rotating around its center and which can be advected with a certain velocity" [6]

Vorticity appears a natural choice for a vortex definition or identification, even if the identification is complicated because of the impossible distinction between pure shearing and swirling motion. Using Hussain definition, "a coherent structure is a connected turbulent fluid mass with instantaneously phase-correlated vorticity over its spatial extent" [62].

A vortex can be described and identified by different parameters, all defined on a plane perpendicular to the vortex core. The fundamental characteristics are: vortex center position, transport velocity, vortex diameter, vorticity peak, vorticity distribution[3], circulation and enstrophy $\left(En = \int_S \omega^2 dS\right)$. It has to be noted that the center of a vortex corresponds to a local pressure minimum and a vorticity peak.

A first identification criterion is represented by the localization of the pressure minimum corresponding to the vortex center, but an experimental pressure map is a quite difficult task to obtain.

A second criterion is the detection of the vorticity peak, also related to the vortex center; while a vortex center always corresponds to a vorticity peak, a vorticity peak does not necessarily corresponds to a vortex center, and this represent a limiting aspect.

Several other methods are used for the vortex identification, but the most widely used is the analysis of the gradient of the velocity field, although it does not discriminate between small and large vorticity.

---

[3] The vorticity is a Galilean invariant of the velocity and it is not affected by an additional transport velocity.

1.10 COMBUSTION INSTABILITIES AND STRUCTURAL DYNAMICS

Several theoretical and experimental studies on combustion show that the reaction velocity depends on pressure and temperature values. At the same time, the combustion dynamics is strongly affected by the oscillation frequency of such values, and in some case the combustion becomes an amplification factor for the pressure instabilities.

In a solid rocket motor the combustion process is supposed to be concentrated in a thin layer close to the propellant surface. When combustion takes place in a confined volume (i.e: adjacent to the propellant surface) it may cause the development of pressure oscillations. If these oscillations are related to unsteady heat release, they are called *combustion instabilities*. Several studies concerning vortex shedding phenomena demonstrate that the combustion instability is related to the coupling between acoustic field and combustion energy release. The acoustic-thermal instability is enhanced if the heat release and the pressure perturbation fluctuation are in phase.

The effects related to real combustion, as the presence of solid particles, are referred to as *distributed combustion*.

Aluminum particles are commonly added in solid propellants, such as HTPB/AP/Al, in a proportion that can reach 20%. This addition provides an higher temperature of the combustion products and, correspondingly, higher performance. The aluminum agglomerates are ejected from the propellant surface and burn in the gas phase.

A dispersed inert phase damps the pressure oscillations thanks to the velocity and thermal lag between gas and particles [97, 29]. However, linear stability analysis of a two-phase flow with parietal injection showed that inert particles can also drive the instabilities [40]. Furthermore, studies on the combustion instability experienced by a motor subjected to parietal vortex shedding, show that inert particles enhance the combustion instability and generate higher oscillation amplitude [36, 10]. The damping or driving effect is also a function of particle diameter, mass fraction and particle distribution [36]. Despite the influence on the oscillation amplitude, two phase flow effects do not modify the oscillation frequency content.

The particles are concentrated between consecutive vortices and this agglomeration leads to *bundles* of particles that pass through the nozzle. These bundles determine larger perturbation without any frequency modulation; the amplitude increase is proportional to the volume of the bundle [11].

Other phenomena of secondary importance can be observed in a solid rocket motor: a damping effect is related to the accumulation and melting of aluminum particles at the propellant surface [95, 86], while a driving effect is represented by the distributed combustion of the aluminum particles [36, 14].

Other aspects that affect this kind of instabilities are the combustion temperature, the motor geometrical features, the interaction with the hydrodynamic instabilities and the flow conditions. This makes the combustion instability a complex phenomenon requiring specific studies and analysis.

The effects related to the dynamic coupling with both the propellant and the launcher structural dynamics are not taken into account; the propellant and the structures are considered as rigid body.

In the present work, the attention is focused on the purely aeroacoustic coupling and the only considered instability is generated by vortex shedding. Other instabilities that can occur in a solid rocket motor, such as combustion instability and structural dynamics, are neglected.

2

AEROACOUSTIC MODELING

The simulation of the pressure oscillation instabilities requires to consider both the acoustic and the vortical waves, including their interactions.

In this chapter, the state of the art of the aeroacoustic modeling is presented, and the fundamental features of the most important methods are described: acoustic balance method, vortex sound theory and acoustic analogy, hydrodynamic stability analysis, Flandro's and Anthoine's models, Hulshoff's theory.

Two reduced order models are then analyzed in details, the first derived by Matveev and the second developed by Jou and Menon.

2.1 STATE OF THE ART OF THE AEROACOUSTIC MODELING

Lighthill's analogy (1952, [69, 70]) is a first attempt to describe the acoustic field and the sound production due to vortex pairing. The inhomogeneous wave equation, obtained for a medium at rest, is based on the analogy of how the flow-induced/generated noise can be described; the acoustic sources are represented by acoustically equivalent source terms. Lighthill's approach only provides an estimate of the sound production.

The first description of the acoustic resonance mechanism is represented by Rossiter's model (1964, [91]), already presented in par. 1.6.

Powell (1964, [85]) developed a model for the vortex sound production, the incompressible *vortex-sound theory*.

The acoustic balance technique, an asymptotic expansion method, was proposed by Hart & McClure (1965, [51]), for the linear analysis of the chamber acoustic modes stability. This method was developed and completed by Culick (1966-1973, [26, 28]) and it is presented in par. 2.2.

Culick's studies (1966, [27]) demonstrated that the mass injection from the propellant surface, that generates a shear flow, represents one of the vorticity generation processes observed in a solid rocket motor. The vortex pairing phenomenon and the tendency of adjacent vortices to combine was described by Michalke (1972, [82]).

Flandro and Jacobs (1973, [46]) first mentioned the idea that the vortex shedding is a source of acoustic energy.

They showed the instability risk due to hydrodynamic instability of the flow sheared regions, and associated the presence of pressure oscillations both to this aspect and to the coupled response of the motor.

A generalization of Powell's theory is represented by Howe's *vortex-sound theory* (1975, [55]). This acoustic analogy expresses the perturbations due to the interaction of vortical disturbance with an obstacle. A description of this theory is presented in par. 2.3.

A model for the excitation of the cavity acoustic modes by vortex shedding was developed by Blevins (1977, [13]).

Culick (1979, [30]) demonstrated that in order to sustain the resonant coupling and to have acoustic feedback, the presence of an obstacle, downstream of the shedding point, is required. The evidence of the sound production related to the interaction between vortex and obstacles was showed by Howe (1980, [56, 58]). He underlined that this sound generation is associated to the deviation of the transport velocity vector from the acoustic streamlines, as also confirmed by Dunlap's studies (1981, [35]). The energy transfer from the vortical field to the acoustic modes, corresponding to the vortex-obstacle interaction, was pointed out by Schachemann (1980, [92]). The vortex shedding excitation of the acoustic field was confirmed by the experimental data analysis of the Titan 34D SRM developed by Brown (1981, [16]).

Brown and Dunlap (1981, [16, 35]) pointed out that vortex shedding triggering by the acoustic modes is related to their relative position, so that it is more effective if the shedding occurs where the acoustic pressure features a node. Brown also described the flute mode behavior of a solid rocket motor.

With their experimental tests, Culick & Magiawala (1979, [30]), Mason (1979, [77]), Dunlap & Brown (1981, [35]) and Nomoto & Culick (1982, [84]) demonstrated the coupling between the periodic vortex shedding frequency and the acoustic modes of the combustion chamber.

Flandro (1986, [45]) developed the most important method used for the stability analysis of solid rocket motors. The linear theory of *Flandro's model*, presented in par. 2.5.1, describes the vortex-acoustic interaction. The model is based on the *hydrodynamic stability analysis* developed by Lin (1955, [71]), presented in par. 2.5. The flute mode behavior was also studied by Flandro (1986, [44]).

The vortex-acoustics coupling with a mean flow was analyzed, basing on Howe's sound theory, by Bruggeman et al. (1989, [17]) and Hourigan et al. (1990, [54]).

Flatau and Van Moorhem (1990, [47]) analyzed the US Space Shuttle SRM experimental data showing, also for this motor, the vortex shedding excitation of the acoustic field. Their studies also involved CFD simulations of the motor internal flowfield, and pointed out the acoustic excitation by vortex-obstacle interaction.

Kuentzmann (1991, [68]) and Vuillot (1993, [107]) proposed studies about the flute-mode behavior.

In order to extract acoustic informations from the results obtained by numerical simulations, Jou and Menon [81, 63] developed a reduced *one-dimensional model*, suitable for the evaluation of the coupled-mode oscillation frequency. A detailed description of this model is provided in par. 2.10.

A theoretical model, based on the vortex-sound theory, was developed by Anthoine (2001, [4, 5]) to study the effect of the nozzle cavity volume on the resonance level; it is presented in par. 2.6.

Another reduced *one-dimensional model* was proposed by Matveev (2003, [80, 78]); it describes the excitation of the acoustic modes accounting for the acoustic feedback on the vortex shedding process. A detailed description of this model is presented in par. 2.11.

The computational fluid dynamics (CFD) and the full Navier-Stokes equations have been used in order to obtain a complete description and understanding of the aeroacoustic process in a solid rocket motor. CFD numerical simulations have been presented by Lupoglazoff (1992, [74]) and Vuillot (1993, [107, 104]). Full numerical simulations were used by Vuillot et. al (1993, [107, 106]) and Kourta (1997, [66]) to simulate the internal flowfield of the Titan IV SRMU, while Nesman (1995, [83]) used them for the analysis of the Space Shuttle SRM. A fundamental result of Vuillot's analysis is the characterization of the vorticity production due to obstacle, surface discontinuity and natural instability of the main profile. The role of the vortex-nozzle interaction as a potential source for the generation of pressure oscillations was also analyzed. The stretching of the vortical structure with the motion toward the impingement point was also pointed out. Full numerical simulations were proposed by Anthoine (2000, [3]) and Hulshoff (2001, [60]) for the analysis of vortex-nozzle interaction; Anthoine et al. (2000, [3]) demonstrated the effect of the submergence region as a sound amplifier. Numerical simulations have been also used by Dotson (1997, [34]) for studies on the Titan IV SRMU. Casali's numerical simulations also dealt with the instabilities due to parietal vortex shedding (1998, [18]). Kourta (1996, [65]) showed that the dynamic viscosity value can affect the resonant coupling mechanism, for example limiting the vortex pairing phenomenon.

Several experimental tests have been performed in order to characterize the different phenomena involved into the acoustic resonance. As shown by the static firing tests analysis developed by Scippa, the Ariane 5 P320 SRM is characterized by the presence of pressure oscillations (1994, [93]). Couton (1999, [25]) experimental analysis[1] showed that

---

[1] The test case was featured by a rectangular two-dimensional channel with wall injection, obstacles and submerged nozzle; a cold flow was considered.

the wall injection of mass flow rate modifies the acoustic amplification level. The experimental set up VECLA has been developed by ONERA to investigate the characteristics of injection-driven flow and of parietal vortex shedding (1999, [9]). The experimental set up employed at VKI and TUE, part of the ASSM program related to Ariane 5 solid rocket motor aeroacoustics, is oriented to the sound generation analysis (2000, [2]). Experimental tests presented by Anthoine et al. (2001, [4]) demonstrated that a duct, with a diaphragm that generates vorticity, acts as a resonator through its natural eigenmodes. Experimental tests are often carried out with cold flows, thus describing pure aeroacoustic coupling without any combustion effects.

2.2 ACOUSTIC BALANCE METHOD

First proposed by Hart & McClure [51], then developed by Culick [26, 28], the acoustic balance technique is an asymptotic expansion method. Its main feature is a linear analysis of the chamber acoustic mode stability.

Each variable can be considered divided into a mean ($\overline{G}$) and a fluctuating ($G^{'}$) component:

$$G(\mathbf{x}, t) = \overline{G}(\mathbf{x}) + G^{'}(\mathbf{x}, t) \tag{2.1}$$

related by the ε parameter so defined:

$$\varepsilon = \frac{|G^{'}(\mathbf{x})|}{|\overline{G}(\mathbf{x}, t)}| \ll 1 \tag{2.2}$$

Two perturbation parameters are considered for the linearization process, ε, defined in eq. 2.2, and the mean Mach number $\overline{M}$. The equations are divided into successive power of ε, that characterizes the instability and is used for the oscillation amplitude. $\overline{M}$ is instead used to simplify the equations. The following particular problems can be described by different ε and $\overline{M}$ combinations:

- $\varepsilon = 0$; $\overline{M}$: steady and incompressible flow
- ε; $\overline{M} = 0$: acoustics without mean flow
- ε; $\overline{M}$: linear coupling of the mean flow and the acoustics

$\varepsilon\overline{M}$ is the lower order that permits the instability description.

The fluctuating component $G^{'}$, once introduced an *amplification coefficient* β, is defined as:

$$G^{'} \propto e^{\beta t} \tag{2.3}$$

Being the acoustic balance method a linear analysis, the total amplification can be expressed as the sum of particular amplification coefficients β_i:

$$\beta = \sum_i \beta_i \tag{2.4}$$

A specific coefficient β_i is introduced for each considered phenomenon: two-phase flow (β_{TP}), combustion (β_{CC}), nozzle interaction (β_{NC}, β_{NR}), flow turning (β_{FT}), acoustic boundary layer (β_{BL}), etc. Detailed analysis of the terms related to combustion, nozzle interaction and two-phase flow effects can be found in the literature [105].

The acoustic modes are initially approximated with the hypothesis of rigid walls, uniform speed of sound and propagation through a medium at rest. The acoustic problem can be reduced to the Helmhotz equation:

$$\Delta\tilde{p} + \frac{\omega_{f,n}^2}{a^2}\,\tilde{p} = 0 \qquad \textit{in the cavity} \tag{2.5}$$

$$\frac{\partial\tilde{p}}{\partial\mathbf{n}} = 0 \qquad \textit{on the surface} \tag{2.6}$$

where a is the speed of sound, $\mathbf{n}$ is the normal direction, $\omega_{f,n}$ is the angular frequency of the n-th mode and $\tilde{p}$ is related to the acoustic pressure p' by the following relation:

$$p' = \tilde{p}\, e^{\,i\omega_f t} \tag{2.7}$$

The effects related to the incompressible mean flow, to the burning surfaces and to the nozzle, modify the eq. 2.5 into:

$$\Delta\tilde{p} + \frac{\omega_{f,n}^2}{a^2}\,\tilde{p} = \tilde{h}_{ab} \qquad \textit{in the cavity} \tag{2.8}$$

$$\frac{\partial\tilde{p}}{\partial\mathbf{n}} = -\tilde{f}_{ab} \qquad \textit{on the surface} \tag{2.9}$$

and the acoustic pressure p' is adjusted to:

$$p' = \tilde{p}\, e^{\,(i\omega_f+\beta)t} \tag{2.10}$$

where the angular frequency is $\omega_f = 2\pi f + i\beta$. The $\tilde{h}_{ab}$ and $\tilde{f}_{ab}$ source terms can be expressed as:

$$\tilde{h}_{ab} = \left(i\,\frac{\omega_f}{a^2}\right)\tilde{\mathbf{u}}\cdot\nabla\tilde{p} - \tilde{\rho}\,\nabla\cdot(\tilde{\mathbf{u}}\cdot\nabla\tilde{\mathbf{u}} + \tilde{\mathbf{u}}\cdot\nabla\tilde{\mathbf{u}}) \tag{2.11}$$

$$\tilde{f}_{ab} = \mathbf{n}\cdot[\,i\omega_f\tilde{\rho}\,\tilde{\mathbf{u}} + \tilde{\rho}(\tilde{\mathbf{u}}\cdot\nabla\tilde{\mathbf{u}} + \tilde{\mathbf{u}}\cdot\nabla\tilde{\mathbf{u}})] \tag{2.12}$$

Taking a volume average, it is possible to obtain a direct expression of ω_f as:

$$\frac{\omega_f^2 - \omega_{f,n0}^2}{a^2}\,E_{n0}^2 = -\frac{i\,\omega_{f,n0}}{a}\int_S\left[\tilde{\rho}\,a\left(\tilde{\mathbf{u}}\cdot\frac{\mathbf{n}}{\tilde{p}}\right) + M_{inj}\right]\tilde{p}_{n0}^2\,dS \tag{2.13}$$

where the subscript 0 is referred to a reference state, M_{inj} is the surface injection Mach number and E_n is defined as:

$$E_n^2 = \int_V \tilde{p}_n^2\,dV \tag{2.14}$$

The term $\left(\tilde{\rho} a \tilde{\mathbf{u}} \cdot \frac{\mathbf{n}}{\tilde{p}}\right)$ represents the surface admittance.

The eq. 2.13 is obtained with the hypothesis of alignment between the velocity field and the acoustic pressure gradient:

$$\tilde{\mathbf{u}} \sim \tilde{\mathbf{u}}_n = \frac{i}{\tilde{\rho}\,\omega_{f,n}} \nabla \tilde{p}_n \tag{2.15}$$

corresponding to the assumption of an irrotational field for the unsteady velocity. This condition causes several limitations to the method, that is not suitable in case of vortex shedding or propellant side injection[2].

The use of the acoustic balance method requires the determination of the reference acoustic mode, the evaluation of the stability integrals and the knowledge of propellant response function, nozzle admittance and size of the particulate phase.

If the linearized equations of motion are considered, the method provides a solution in terms of reference acoustic mode perturbation[3]. This condition establishes a strong dependence on the acoustic field.

A strong restriction to the application of this method is the absence of some sources of instabilities, such as vortex shedding. Further, although useful in order to understand and to isolate each phenomenon, it does not provide a reliable evaluation of the oscillation amplitude, which causes limitations to the model predictive capability.

2.2.1 VORTEX SHEDDING SOURCE TERM FOR THE ACOUSTIC BALANCE METHOD

As mentioned previously, the acoustic balance method does not take into account some sources of instability, such as vortex shedding. A first attempt to introduce the vortical structures into this method was proposed by Brown [15], but any development has been given.

Vuillot [104, 105] proposed the introduction of the following additional source terms with the main purpose to model the vortex shedding effects and to introduce the acoustic coupling in the acoustic balance method.

The unsteady velocity field, not aligned with the acoustic pressure gradient, is assumed composed by the acoustic component and the vortical fluctuation. The vortex shedding source term, derived from the linearization of the term $\mathbf{u} \cdot \nabla \mathbf{u}$, is expressed as:

$$\tilde{\rho}\left\{\int_V k_{n0}^2 [\tilde{\mathbf{u}} \cdot (\tilde{\mathbf{u}} - \tilde{\mathbf{u}}_{n0})] \tilde{p}_{n0} dV + \int_V (\tilde{\boldsymbol{\omega}}_0 \times \tilde{\mathbf{u}}) \nabla \tilde{p}_{n0} dV + \int_V (\tilde{\boldsymbol{\omega}}_0 \times \tilde{\mathbf{u}}) \cdot \nabla \tilde{p}_{n0} dV\right\} \tag{2.16}$$

with the notation adopted in the paragraph and the wave number k_n.

---

[2] Such cases are related to highly rotational velocity fields.

[3] The reference acoustic modes are obtained from the solutions of the homogeneous equations, obtained in absence of forcing function, two-phase flow and combustion effects.

The integrals in eq. 2.16 are difficult to evaluate and require the knowledge of the flow organization in the combustion chamber. The last integrand in eq. 2.16 is strictly related to the vortex shedding phenomenon; it presents significant contributions in correspondence of large values of $\tilde{\mathbf{u}}$ and $\boldsymbol{\omega}_0$. It also shows the phase relation between the impacting vortex and the acoustic field.

2.3 VORTEX-SOUND THEORY AND ACOUSTIC ANALOGY

The sound production in a solid rocket motor is related to the interaction between the vortices and the nozzle nose [45, 34], and to the deviation of the transport velocity vector from the acoustic streamlines [56]. The level of sound production is increased by the presence of cavities (i.e: submergence cavity) and the resonance level is higher for larger cavity volume [2, 5].

A first attempt to obtain an estimate of the pressure fluctuation order of magnitude is represented by *Lighthill's analogy* [69, 70]. The analogy is derived without any approximation from the Navier-Stokes equation. An inhomogeneous wave equation is obtained and the acoustic sources are represented by acoustically equivalent source terms. The vortices are considered as an independent source of acoustic waves, and their presence merely excites the acoustic disturbance. Lighthill's model is not useful when the presence of an external acoustic field has to be considered, and in general for high Mach number flows.

When the feedback from the acoustic field is not negligible, and in general for homentropic low Mach number flows, the incompressible *vortex-sound theory* developed by Powell [85] is more appropriate. The generalization to compressible theory was proposed by Howe [55]. While Powell derived the analogy for subsonic flow in free field condition, implying the hypothesis of a compact source (par. 3.2), Howe generalized it to internal flows and to arbitrary Mach number M. The vortex-sound theory assumes the knowledge of the vortical distribution, and deduces the aeroacoustic sound production from this knowledge [53].

Howe [55] derives an *acoustic analogy* to express the perturbations, in an internal flow, due to the convection of entropic and vortical dishomogeneities that interact with cross area variations. Two sections of a channel (height r_1 and r_2) are separated by a nozzle, as illustrated in fig. 2.1. The channel has an infinite length, so that it can be considered anechoic. A low Mach number is considered and, as for a solid rocket motor, a negative vortex circulation is assumed.

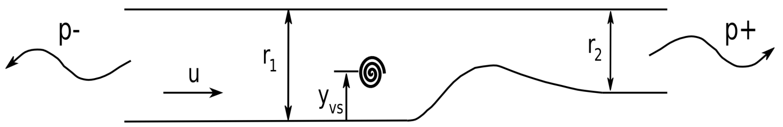

Figure 2.1: Sound production of vortex-nozzle interaction (figure from: [60]).

When the vortex interacts with an obstacle, an acoustic wave p^-, driving instability, is radiated upstream. The acoustic wave p^+, radiated downstream, can be neglected. For a Mach number $M \ll 1$, it is possible to consider the region of sound production, close to the obstacle, as a compact region. This assumption permits to derive an analytic expression for the p^- wave.

The mass conservation equation (eq. 3.1) can be combined with Crocco's equation[4] and, in case of low Mach numbers ($M < 0.3$), the far-field total enthalpy perturbation can be expressed as [55]:

$$H^- = \frac{r_2}{r_1(r_1 + r_2)\,(1 - M_2)} \cdot \int_V [(\boldsymbol{\omega} \times \mathbf{u} - T\nabla s) \cdot \mathbf{u}'] \, dV \tag{2.17}$$

where the entropy s is introduced and $\mathbf{u}'$ is the acoustic velocity vector, the irrotational part of the velocity field. The quantities in the square brackets are evaluated at a retarded time, proportional to the distance between the source and the far-field point at which the perturbation is measured. Such retard has negligible effects at low Mach numbers. The term $(1 - M_2)$ can be viewed as a *Doppler factor*.

For small enthalpy changes, the enthalpy perturbation can be indicated as:

$$H^- = \frac{p^-}{\overline{\rho}}\,(1 - M_1) + o(M^2) \tag{2.18}$$

For a homoentropic flow ($DS/Dt = 0$), with the eq. 2.18, the eq. 2.17 can be rewritten in terms of upstream pressure perturbation:

$$p_1^- = \frac{r_2}{r_1(r_1 + r_2)\,(1 - M_1)\,(1 - M_2)} \cdot \int_V \overline{\rho}\,[(\boldsymbol{\omega} \times \mathbf{u} - T\nabla s) \cdot \mathbf{u}'] \, dV \tag{2.19}$$

The eq. 2.19 represents the *Powell-Howe analogy*. For low M numbers, then for compact source regions, the acoustic perturbation is directly proportional to the *Lamb vector* $\boldsymbol{\omega} \times \mathbf{u}$. A dependence from the mean flow Mach number can also be noted. The pressure oscillation amplitude increases with the vortex circulation level and with the cavity volume; it is also affected by the vortex initial height with respect to the obstacle.

The eq. 2.19 is a generalization of Powell analogy [85] to confined uniform-flow conditions, derived for stagnant free-field conditions. It is obtained by combining the vortex-sound analogy for compact sources, developed by Howe, with the simulation of incompressible vorticity dynamics, introduced by Powell.

At low Mach numbers, the time average acoustic power $\wp$, moved from the the vorticity field to the acoustic field, can be expressed as [57]:

$$\wp = -\overline{\rho}\,\langle \int_V (\,\boldsymbol{\omega} \times \mathbf{u}\,) \cdot \mathbf{u}' dV \rangle \tag{2.20}$$

---

[4] $\frac{\partial \mathbf{u}}{\partial t} + \nabla H = -\,\boldsymbol{\omega} \times \mathbf{u} + T\nabla s$

where ρ is the density, $\boldsymbol{\omega}$ is the vorticity, V is the source volume (where $\boldsymbol{\omega} \neq 0$), $\mathbf{u}$ is the vortex transport velocity and $\mathbf{u}^{'}$ is the acoustic velocity component[5]. The acoustic power $\wp$ is stronger for higher acoustic fluctuations ($\mathbf{u}^{'}$); the most important factors that affect the sound production, in terms of magnitude and phase, are the vortex circulation and its initial position. The exact signal shape is also determined by the nozzle geometrical configuration and the vorticity distribution.

The sound production is due to the vortex cross of the acoustic streamlines ($\mathbf{u}^{'}$ direction): for parallel transport velocity vector $\mathbf{u}$ and acoustic streamline, no energy production occurs.

The Powell-Howe analogy can not be used for high Mach numbers. In this case, the main flow is altered by the compressibility effects alter the main flow and the source regions can not be considered compact.

2.4 HULSHOFF'S MODEL

Hulshoff [60] developed an approximate model to evaluate the compressibility influence on the acoustic coupling. Two different approaches were proposed, both for low ($M < 0.2$) and high ($M > 0.2$) Mach number flows.

Hulshoff's studies confirmed that the Powell-Howe analogy is a suitable tool for the evaluation of the sound production at low M numbers. In such cases, the amplitude and the phase of the produced sound are determined by the vortex circulation and position, by the vorticity distribution and by the nozzle geometry.

The non-compactness effects strongly affect the sound production at high Mach numbers, determining an increase of the pressure oscillation amplitude. Hulshoff also showed that in case of large vortex circulation, the vortex may be repelled from the nozzle.

LOW MACH NUMBER FLOWS ($M < 0.2$) To analyze low Mach number flows, Hulshoff [61] considered the purely inviscid sound-production effect; he used a vortex-blob potential-flow solution [67] and Howe's acoustic analogy [55].

The vortex-blob method is based on the solution of plane potential flows with a singularity distribution approach, that allows the computation of the vorticity dynamics. The discretization of the boundaries is realized with piecewise constant distributions of vorticity and sources; the source strength is determined by the locally specified normal velocity.

Each vortex in the domain is represented by a point vortex; its position is advanced in time using a fourth-order Runge Kutta technique in which the flow velocity is continually updated.

Hulshoff noted that a vortex approaching an obstacle deviates from the irrotational streamlines. This deviation produces a rotation ($\boldsymbol{\omega} \times \mathbf{u}$) opposed to the local irrotational

---

[5] $\langle\rangle$ denotes the time average over one period of oscillation.

velocity. His results also demonstrated that the perturbation amplitude is proportional to the vortex circulation and that it is influenced by the vortex height with respect to the obstacle.

HIGH MACH NUMBER FLOW ($M > 0.2$) Because of both the non-compact source effects and the mean-flow compressibility, the Powell-Howe analogy can not be used for the analysis of the high M number flows. For such cases, Hulshoff proposed a time-accurate numerical procedure for the Euler equations. It is based on a two-dimensional, second order-accurate finite volume method with scalar nonlinear artificial dissipation [60].

2.5 HYDRODYNAMIC STABILITY ANALYSIS

The *hydrodynamic stability analysis*, developed by Lin [71], relies on the linearization of the incompressible equations of motion around a known mean flow.

The *Orr-Sommerfeld equation* is obtained [12] with the assumption of parallel flow; if the viscosity is neglected, the *Rayleigh equation* is derived. As stated by Varapaev [102], the flow stability is strongly affected by radial mass injection, and this makes the hypothesis of parallel flow not realistic near the propellant surface.

For simplicity, a one-dimensional propagation along the x-axis is considered.

The velocity field is assumed divided into an acoustic ($u^{'}$) and a mean flow ($\overline{u}$) component:

$$u(t) = u^{'}(t) + \overline{u} \tag{2.21}$$

with $|u^{'}| \ll |\overline{u}|$. For a mean velocity profile given by $\overline{u}(y)$, the fluctuation can be expressed as:

$$u^{'} = B\,\tau(y)\,e^{i(\beta x - \omega_f t)} \tag{2.22}$$

$$v^{'} = B\,\varphi(y)\,e^{i(\beta x - \omega_f t)} \tag{2.23}$$

$$p^{'} = B\,\pi(y)\,e^{i(\beta x - \omega_f t)} \tag{2.24}$$

where ω_f is the angular frequency, B is an integration constant, $\tau(y)$, $\varphi(y)$, and $\pi(y)$ are the vortical fluctuation profiles across the shear layer and β is an amplification factor.

For any given angular frequency ω_f, with the spatial growth rate theory, the hydrodynamic stability analysis yields the following expression of the amplification factor:

$$\beta = \beta^{r} + i\beta^{i} \tag{2.25}$$

Once that β is obtained, $\tau(y)$, $\varphi(y)$, and $\pi(y)$ can be derived.

The hydrodynamic stability analysis has been used in different applications. At ONERA it is a tool for validation of internal aerodynamic codes [75], while at ONERA/CERT/DERAT it is used for the study of the shear layer, with the solution of the incompressible Orr-Sommerfeld equation [7].

2.5.1 FLANDRO'S METHOD

Flandro's method [45] is a linear theory based on the hydrodynamic stability analysis, used in order to obtain the vortex properties (wave length, convection speed, ...) at the shedding point.

Vortex-shedding additional terms are added to the acoustic balance method [45, 74, 104]. The vortex impact mechanism is modeled through a localized volumetric force. From the derivation of linearized equations, two vortical flow effects are identified: a negligible volume integral and a body force concentrated at the vortex location (dipole effect).

The flow is considered divided in three parts: the mean component, the acoustic component ($\mathbf{u}^{'}$, compressible and irrotational) and the hydrodynamic component ($\mathbf{u}^{''}$, incompressible and rotational).

The method is composed by four fundamental steps:

- determination of the shear layer velocity profile, responsible for the hydrodynamic instability
- with the use of the spatial growth rate theory, determination of the hydrodynamic stability of the velocity profile
- for an acoustic mode of given frequency, coupling of the vortical field with the acoustic field
- choice of an impact surface where the sound field, associated with the vortical flow, interacts with the acoustic field

The coupling procedure between the hydrodynamic solution and the acoustic field, third step, is based on the following first-order coupled equations for the non dimensional vorticity:

$$\zeta = \xi \, e^{-i\omega_f t} \tag{2.26}$$

$$\frac{\partial \zeta}{\partial t} = \frac{1}{M} \nabla \times (\mathbf{u}^{'} \times \overline{\boldsymbol{\omega}}) \tag{2.27}$$

where ζ is the non dimensional hydrodynamic vorticity, ξ is the spatial variation of non dimensional hydrodynamic solution and $\mathbf{u}^{'}$ is adimensionalized by the speed of sound. The obtained solution is indicated with ξ_p, and it is added to the hydrodynamic field to express the ξ_{tot} as follows:

$$\xi_{tot} = \xi_p + B\xi \tag{2.28}$$

the integration constant B can be found imposing $\xi_{tot} = 0$ at the origin of the shear layer.

The fourth step corresponds to the inclusion of the vortex-shedding effects into the acoustic balance method. The dipole effect at the vortex impact is modeled with a linear growth rate:

$$\beta_{vs} = \frac{\rho\, a^2}{2\, E_n^2} \int_{S_i} p'' \, \mathbf{u}' \cdot \mathbf{n} \, dS \tag{2.29}$$

where E_n is the energy related to the n-th mode, which is a function of the acoustic pressure p', and defined as:

$$E_n^2 = \int_V p'^{\,2} \, dV \tag{2.30}$$

The acoustic growth rate is defined as the product of two functions. The first is a scalar function defined by the shear-layer origin and the impingement point. The second is defined by the shear layer momentum thickness δ_t, the stand-off distance l_i and the Strouhal number St, referred to the shear layer momentum thickness δ_t[6].

Flandro's method is useful to understand the mechanisms that originate the vortex shedding driven oscillations. However, it is extremely sensitive to unknown details, such as the exact vortex origin. Any realistic value is obtained with this analysis, and its application is limited to qualitative analysis, based on the phase difference between the vortex impact and the acoustic field. Vuillot [107, 105] used this linearized model to study the Ariane 5 MPS P230 aeroacoustics, obtaining qualitatively correct results.

2.6 ANTHOINE'S MODEL FOR SUBMERGENCE INTERACTION

As noted, the vortex sound production is affected by the presence of a cavity and the induced pressure oscillation level depends on the cavity volume (par. 1.4). The major sound production in a solid rocket motor derives from the impingement of a vortex on the nozzle inlet.

Anthoine [4, 5] developed a theoretical model, based on the vortex-sound theory, for the effect of the nozzle cavity volume on the resonance level (par. 2.3).

The model is derived for a nozzle cavity characterized by a volume V_s and an entrance of cross-section S_s. The cavity length is assumed small if compared to the acoustic wave length L, and the section S_s is considered parallel to the chamber axis. The acoustic field is supposed to be harmonically oscillating, so that it can be expressed as:

$$\mathbf{u}' = |\mathbf{u}'| \, e^{\, i\, 2\pi f_a t} \tag{2.31}$$

function of the acoustic frequency f_a.

---

[6] The Strouhal number is defined as: $St = \frac{fL}{u}$.

In such configuration, the compressibility $dp^{'}/dt$ of the gas in the cavity induces an acoustic fluctuation $\mathbf{u}^{'}$ in the section S_s. For the mass conservation equation:

$$\rho_0 \mathbf{u}^{'} S_s \sim \frac{V_s}{a^2} \frac{dp^{'}}{dt} \tag{2.32}$$

where $\overline{\rho}$ is the reference state density. With the perfect gas law for the reference state[7] and for an harmonically oscillating acoustic field, the acoustic fluctuation becomes:

$$|\mathbf{u}^{'}| = \frac{2\,\pi\,f_a\,V_s}{\gamma\,S_s} \frac{|p^{'}|}{\overline{p}} \tag{2.33}$$

The acoustic power expression presented in eq. 2.20, allows to express the maximum acoustic power production as:

$$\wp_{max} \sim \overline{\rho}\,|\mathbf{u}^{'}||\mathbf{u}_{vs}| \int_V |\boldsymbol{\omega}|\, dV \sim \overline{\rho}\,|\mathbf{u}_{vs}|\,|\mathbf{u}^{'}|\,\pi D \Gamma \tag{2.34}$$

function of the vortex convection velocity, the acoustic fluctuation $\mathbf{u}^{'}$ and the circulation Γ[8]. The transport velocity $\mathbf{u}_{vs}$ can be approximated as a fraction of the mean flow velocity $\overline{\mathbf{u}}$:

$$\mathbf{u}_{vs} = \frac{\overline{\mathbf{u}}}{2} \tag{2.35}$$

The maximum pulsation level is obtained when the vortex passes in front of the cavity at the time corresponding to the maximum power generation. The *time fraction* in which the vortex travels in front of the cavity entrance T_s, compared to the vortex shedding period T_{vs}, is introduced into the eq. 2.34 by the following coefficient:

$$\frac{T_s}{T_{vs}} = \frac{h_c f_a}{\overline{\mathbf{u}}} \tag{2.36}$$

where h_c is the cavity entrance width. Assuming a time fraction $T_s/T_{vs} \ll 1$, the generated acoustic power is:

$$\wp \sim \overline{\rho} \frac{\overline{\mathbf{u}}}{2} \frac{2\,\pi\,f_a\,V_s}{\gamma\,S_s} \frac{|p^{'}|}{\overline{p}} \pi D \Gamma \frac{h_{vs}\,f_a}{\overline{\mathbf{u}}} \tag{2.37}$$

In the limit of the used hypotheses, the circulation can be expressed as:

$$\Gamma \sim l_{vs} \frac{\overline{\mathbf{u}}}{2} \sim \frac{\overline{\mathbf{u}}^2}{4\,f_a} \tag{2.38}$$

where l_{vs} is the distance where the vortex accumulates vorticity. l_{vs} is assumed to be equal to the distance between two successive vortices,so that is can be approximated as:

$$l_{vs} \sim \frac{\overline{\mathbf{u}}}{2f_a} \tag{2.39}$$

---

[7] $\overline{\rho} a^2 = \gamma \overline{p}$

[8] $\Gamma = \int_S (\boldsymbol{\omega} \cdot \mathbf{n})\, dS$

With the eq. 2.38, 2.39 the eq. 2.37 can be rewritten as:

$$\wp \sim \frac{\pi}{4}\,\overline{M}^2\, f_a\, V_s\, |p'| \sim \frac{|p'|^2}{2}\,\frac{\pi D^2}{4}\,\frac{\overline{M}\,(\gamma-1)}{2\,\overline{\rho}\,\overline{a}} \tag{2.40}$$

where the fundamental dependences are on the mean flow Mach number $\overline{M}$, on the acoustic fluctuation $\mathbf{p}'$ and on the cavity volume V_s. The eq. 2.40 leads to:

$$\frac{|p'|}{p_0} \sim \frac{\pi\gamma}{\gamma-1}\, n\, M_0\, \frac{V_s}{V_c} \tag{2.41}$$

where n represents the mode number.

The model shows that the sound production is a continuous process. As expected from the vortex-sound theory, the cavity volume plays an important role for the pressure fluctuations magnitude; the evolution of the maximum sound pressure level is approximately linear with the nozzle cavity volume and depends on the nozzle design. The fluctuation level is amplified each time the excited frequency is close to an acoustic mode frequency. When resonance occurs, the sound pressure level is a linear function of the Mach number, the excited mode number and the nozzle cavity volume.

The effect of different nozzle geometries is also analyzed by Anthoine [3]. In the same Mach number range, for each analyzed nozzle configuration the same acoustic mode is excited, and the only difference is the obtained pressure oscillation level.

The amplitude prediction obtained by this model is too large by almost two orders of magnitude, so that it provides a qualitative prediction.

2.7 ANTHOINE'S MODEL FOR THE M NUMBER AT MAXIMUM SOUND GENERATION

Anthoine [2] presented an analytical model for the mean flow Mach number $\overline{M}$ related to the maximum sound production. This model is based on Rossiter's approach, and it is obtained considering the vortex shedding generated by the presence of an inhibitor (obstacle vortex shedding).

The model provides a relation that links the Mach number $\overline{M}$, at which the acoustic coupling is predicted to occur, to the excited mode number n, to the stage number m, to the relative position of the inhibitor x_{vs}, compared to the total length L, and to the inhibitor diameter D_{vs} compared to the chamber diameter D:

$$\overline{M} = \frac{C_{vc}}{2k_v}\left(\frac{n}{m-0.25}\right)\left(\frac{x_{vs}}{L}\right)\left(\frac{D_{vs}}{D}\right) \tag{2.42}$$

C_{vc} is the vena contracta coefficient of the jet generated by the inhibitors and k_v is the ratio of the vortex transport velocity to the jet velocity (from experimental data $C_{vc} = 0.68$ and $k_v = 0.47$).

2.8 NUMERICAL METHOD

The description of the instabilities until now considered, requires models capable to characterize both the acoustic and the vortical waves, including their non-linear interactions. Different phenomena have to be considered: acoustic field and propagation of the acoustic waves, internal and nozzle flow, acoustically forced vorticity waves and vortex-shedding, flow instabilities and their non-linear growth, two-phase flow effects and the coupling with propellant combustion and structural elements.

The full numerical solution of the compressible Navier-Stokes equations provides the needed framework. The numerical simulations developed in the last years drew further informations about the aeroacoustic process in a solid rocket motor [2] (i.e: classification of the flow regimes that led to motor instabilities, Taylor's flow instability origin, ...).

Lupoglazoff [73, 74, 76] and Vuillot first established the feasibility of the full numerical approach; they also underlined that such approach is able to reproduce the frequency cascade phenomenon. These studies demonstrated that a stabilization can be obtained by decreasing the shear layer critical frequency below the first acoustic mode. Also Tissier and Kourta [65, 66] used computational fluid dynamics for numerical simulation of the unsteady internal flow.

In a such complex context, a meaningful numerical solution remains a difficult task within acceptable limits. CFD numerical simulations are quite expensive, require high computational times, and the obtained results are usually usable only for particular geometries. This aspect limits the use of full numerical approach to documented situations and makes the a priori prediction not feasible in every situation.

A usable predictive tool has to provide the frequency and the amplitude of the pressure oscillation. The choice of the proper model has its limit in the physics included in each used model and in the required input. Currently, these models are capable to predict frequency values in good agreement with the available experimental data; notwithstanding this, the obtained amplitude prediction is generally an overestimation.

All these aspects make the full numerical simulation not suitable as predictive tool, but mainly for the physical mechanisms analysis.

2.9 REDUCED ORDER MODELS

Although very powerful, the full numerical approaches provide global results that require some form of analysis. The presence of non-linear interactions between different phenomena is one of the obstacle when specific results are analyzed, understood, validated and accepted. In this case the CFD analysis can be combined with reduced order models.

The fundamental characteristics that make a reduced-order model a useful tool, are the reduced computational costs and times, the possible improvement of relevant process understanding and their applicability to design optimization and control theories applications.

Rossiter's model (par. 1.6) [91] is the first reduced order model that has been realized; based on simple considerations, it is a correlation, with empirical parameters, for the amplified frequency. A limit of this model is represented by its limited usefulness in case of transient processes.

Blevins [13] developed a model for the excitation of cavity acoustic modes by vortex shedding from a cylinder. An acoustic source is introduced at the vortex detachment point, but the model does not take into account the acoustic feedback on the vortex shedding process.

Also the complex theory proposed by Flandro (par. 2.5.1) [45] is a reduced order model for vortex-acoustic interaction, but it only describes the stability of a solid rocket motor.

Bruggeman et al. [17] proposed a model for the vortex-acoustics coupling in ducts with a mean flow. They used an energy approach based on Howe's sound theory.

Howe's theory is also used in the model developed by Hourigan et al. [54].

All these models allow the analysis of some aspects or phenomena characterizing the vortex-acoustic interaction, but they still require significant computational costs [17, 54]. Frequently, they are only able to describe the steady-state processes [34, 91].

In order to analyze the results obtained by numerical simulations and to extract information on the physical processes that lead to pressure oscillation, Jou and Menon [81, 63] developed a *one-dimensional* model.

Another simple *one-dimensional* model was also proposed by Matveev [80, 78] for the description of vortex induced acoustic instability.

Matveev's and Jou and Menon's models present quite different approaches, but their common feature is to be a one-dimensional model.

2.10 JOU AND MENON'S MODEL

The reduced order model presented by Jou and Menon [81, 63] is a *one-dimensional model* developed for the analysis of the results obtained by full numerical simulations, and for the extraction of informations on the physical processes that lead to the presence of pressure fluctuations. The model describes and explains the interaction between the acoustic wave and the vortical disturbance, and provides a method for the approximative evaluation of the coupled mode frequencies. It has been derived for an axisymmetric combustor.

Lighthill's analogy [69, 70] is a wave equation where the acoustic sources are represented by acoustically equivalent source terms (the acoustic sources are represented by a distribution of quadrupole sources). It is possible to express this analogy by using the velocity potential ϕ and the source term contribution to the dilatation field $\Delta_s^{'}$:

$$\nabla^2\phi - \frac{1}{a^2}\frac{D^2\phi}{Dt^2} = \Delta^{'} \tag{2.43}$$

The source term contribution $\Delta_s^{'}$ in the source region is greater than the propagation term, that is consequently neglected. The method requires the acoustic source behavior extracted from the numerical simulation, and assumes that the small-scale sources can be considered compact.

Instead of the acoustic potential ϕ, the acoustic pressure $p^{'}$ is chosen as acoustic variable. The eq. 2.43 can be rewritten as:

$$\frac{1}{a^2}\frac{\partial^2 p^{'}}{\partial t^2} - \frac{\partial^2 p^{'}}{\partial x^2} = \rho\frac{\partial\Delta^{'}}{\partial t} \tag{2.44}$$

It has to be noted that, in case of low subsonic flows, the convection of the acoustic disturbances by the mean flow is neglected.

The vortices are assumed small, compared to the acoustic wavelength. Assuming a sampling volume corresponding to the entire nozzle region, the dilatation field at the vortex impact is written as:

$$\Delta^{'} = -\alpha\,\omega(x_N)\,\frac{\partial}{\partial x}\delta(x - x_N) \tag{2.45}$$

with the transfer coefficient α, the nozzle location x_N and the vorticity ω. The minus sign in eq. 2.45 suggests that the generated dipole and the vorticity fluctuation are out of phase of π rad.

The following convective equation is assumed for the vortical disturbance:

$$\frac{\partial\omega}{\partial t} + u_{\nu s}\,\frac{\partial\omega}{\partial x} = \sigma\omega \tag{2.46}$$

where σ represents a growth rate model for the spatial growth of vortical disturbance. The convective velocity $u_{\nu s}$ consists of two parts: the phase speed of the vortical disturbance (it is the dominant part, almost 0.6 of the mean flow velocity) and the convection of vorticity by acoustically induced velocity, a contribution that, assumed small, is neglected in the model.

In this one dimensional model, the detailed vorticity dynamics is lost.

The eq. 2.44 is applied separately to the dump combustor region and to the inlet duct; the solution is matched by the continuity condition:

$$p_d = p_{in} \qquad \text{at } x = 0 \tag{2.47}$$

$$D_d^2\frac{\partial p_d}{\partial x} = D_{in}^2\frac{\partial p_{in}}{\partial x} \qquad \text{at } x = 0 \tag{2.48}$$

where the dump plane is located at $x = 0$, D_d and D_{in} are the diameters of the dump plane and of the inlet duct, p_d and p_{in} are the corresponding pressure.

A boundary condition of constant stagnation pressure p_{in} is applied at the inlet; this condition is expressed in term of homogeneous boundary condition by linearization of the steady-state isentropic relation:

$$\frac{p_{in}}{p} + \gamma M \frac{u^{'}}{a} = 0 \tag{2.49}$$

The boundary condition does not add energy to the acoustic oscillations in the domain; such condition has a damping effect on the acoustic waves and does not generate spurious acoustic waves.

The nozzle and the supersonic regions are replaced by a dipole source in the acoustic equation.

At the trailing edge x_0, the following condition is applied:

$$\omega_{x_0} = -\beta u^{'} = 0 \tag{2.50}$$

where β is a transfer function. The acoustic velocity $u^{'}$ is related to the acoustic pressure gradient:

$$\bar{\rho}\frac{\partial u^{'}}{\partial t} = -\frac{\partial p_d^{'}}{\partial x} \tag{2.51}$$

where $p_d^{'}$ is the acoustic pressure.

The vorticity dynamics and the acoustic oscillation are coupled through the dipole source and the boundary conditions. The system of equations is homogeneous and the eigensolution can be expressed by:

$$\begin{bmatrix} p \\ \omega \end{bmatrix} = \begin{bmatrix} \tilde{p}(x) \\ \tilde{\Lambda}(x) \end{bmatrix} e^{ift}$$

Considering the non dimensional variables, but maintaining the same nomenclature, the eq. 2.46 can be integrated to obtain:

$$\tilde{\omega} = a_5 e^{-i\frac{fx}{M} + \frac{\sigma x}{M}} \tag{2.52}$$

where σ is the already introduced vortical disturbance growth rate, and a_5 is an integration constant.

The Green's function for the acoustic equation is given by a retarded potential; the particular solution of eq. 2.44 is given by:

$$p_p = \pm\alpha\omega^{''}(t - |x - x_n|) \qquad x < x_n, \quad x > x_n \tag{2.53}$$

where $^{'}$ represents the derivative with respect to the argument; only the region $x < x_n$ is of interest.

With the particular solution of eq. 2.53, the general solution of the forced acoustic equation in the dump region is expressed as:

$$\tilde{p}_d = a_3 e^{ifx} - a_4 e^{-ifx} \pm a_5 \frac{\Lambda}{\beta} F e^{-if|x-x_n|}] \tag{2.54}$$

where a_3 and a_4 are integration constants and:

$$F = f^2 e^{\frac{ifx_n}{M}} \tag{2.55}$$

Λ is a non dimensional interaction parameter that describes the overall interactions between acoustic oscillation and vorticity dynamics. Λ is defined as:

$$\Lambda = \alpha\beta e^{\frac{\sigma}{M} x_N} \tag{2.56}$$

and it is here assumed of constant value[9].

The obtained expression for the acoustic pressure in the inlet duct is:

$$\tilde{p}_{in} = a_1 e^{ifx} + a_2 e^{-ifx} \tag{2.57}$$

where a_1 and a_2 are integration parameters.

Because of the homogeneous boundary conditions, the eigenvalue f can be obtained imposing a null determinant. The eigenvalue problem contains four different physical parameters: the convective Mach number, the inlet duct length, a geometrical parameter and the overall interaction parameter Λ defined in eq. 2.56.

The characteristic condition can be simplified as:

$$\left(\frac{R+1}{R-1} - \frac{1+M}{1-M} e^{2ift}\right)(2\Gamma_m + 1) - \left(\frac{2R}{R-1}\right)(1+\Gamma_m)\left(1 + \frac{1+M}{1-M} e^{2ift}\right) = 0 \tag{2.58}$$

where:

$$\Gamma_m = F\Lambda e^{-if} \tag{2.59}$$

The frequency f is a complex number, and absolute instability is possible when $Im(f) < 0$.

Some of the approximations introduced in the model can affect the obtained solution. The most important are the assumption $u_{vs} = (0.5 - 0.6)u$ and the absence of acoustic waves convected by the mean flow.

The model provides a method for an approximate evaluation of the coupled modes frequency. It represents a tool to understand the acoustic/vortex interaction, but it does not clearly demonstrate the physical mechanism of this interaction.

---

[9] It is not independent from the acoustic frequency f; the assumption of a constant Λ does not significantly affect the real part of the eigenvalue f.

2.11 MATVEEV'S MODEL

The reduced order model derived by Matveev [80, 78], based on a system of ordinary differential equations, describes the acoustic mode excitation accounting for the acoustic feedback on the vortex shedding process. The developed formulation deals with isothermal flows only.

Matveev's model was developed for a circular duct with a pair of ring baffles, even if it can be applied to geometrical configuration where the vortex generation point and the impingement region can be clearly identified.

In order to maintain a reduced order approach, some assumptions are considered. The most important one is the use of a *one-dimensional* acoustic theory, justified because the longitudinal mode is the fundamental one.

Both the mean flow and the oscillating component Mach number is assumed to be small. The only considered acoustic disturbance is the vortex impingement on the obstacle, and the vortex properties are supposed to be unchanged until its impingement.

The vortex sound generation is modeled through a volumetric source Q, per unit of volume, and a body force F, per unit of mass; they can be respectively considered as a monopole and as a dipole.

The one-dimensional wave equation for the pressure fluctuation p', in absence of losses and with the introduction of the source Q and the force F, becomes:

$$\frac{\partial^2 p'}{\partial t^2} - a^2 \frac{\partial^2 p'}{\partial x^2} = \rho a^2 \left(\frac{\partial Q}{\partial t} - \frac{\partial F}{\partial x} \right) \tag{2.60}$$

The perturbations p' and u', with an expansion through eigen-acoustic modes p'_n and u'_n, are expressed as:

$$p' = \sum_n p'_n(x,t) = \overline{p} \sum_n \eta_n(t) \psi_n(x) \tag{2.61}$$

$$u' = \sum_n u'_n(x,t) = \sum_n \frac{\dot{\eta}_n(t)}{\gamma\, k_n^2} \frac{d\psi_n(x)}{dx} \tag{2.62}$$

where $\overline{p}$ is the mean pressure, k_n is the wave number, $\eta_n(t)$ is the time-varying amplitude of the n-mode and $\psi_n(x)$ is the n-mode shape.

A small nonorthogonality is assumed for the eigenmodes and a linear mode damping ξ_n is introduced. The eq. 2.61, multiplied by $\psi_n(x)$ and integrated over the entire volume, provides a dynamic equation for each mode:

$$\frac{d^2\eta_n}{dt^2} + 2\xi_n \omega_{fn} \frac{d\eta_n}{dt} + \omega_{fn}^2 \eta_n = \gamma \frac{\int \psi_n \left(\frac{\partial Q}{\partial t} - \frac{\partial F}{\partial x} \right) dx}{\int \psi_n^2 \, dx} \tag{2.63}$$

with the linear mode damping ξ_n and the angular frequency ω_{fn}.

As seen, larger vortex circulations determine a greater energy transfer to the acoustic field; the forcing terms of the wave equation are then assumed proportional to the vortex circulation Γ, which is representative of the vortex intensity. If the vortex collision instantaneously occurs and it is localized in space and time, the forcing terms, with delta functions in space and time, are expressed as:

$$Q = c_q \sum_j \Gamma_j \delta(x_{ob} - x_j)\delta(t - t_j) \tag{2.64}$$

$$F = c_f \sum_j \Gamma_j \delta(x_{ob} - x_j)\delta(t - t_j) \tag{2.65}$$

where the summation is over the shed vortices, x_{ob} is the obstacle position, x_j is the vortex position and t_j is the vortex impingement moment. c_q and c_f are two forcing coefficients whose values are obtained from experimental data fitting.

In the time interval $(t_{j-1}; t_{j+1})$, with the eq. 2.64, the dynamics equation for the nth mode, eq. 2.63, becomes:

$$\ddot{\eta}_n + 2\xi_n\omega_n\dot{\eta}_n + \omega_n^2\eta_n = c_{qn}\psi_n(x_{ob})\Gamma_j\frac{d\delta}{dt}(t - t_j) + c_{fn}\frac{d\psi_n}{dx}(x_{ob})\Gamma_j\delta(t - t_j) \tag{2.66}$$

with:

$$c_{qn} = c_q\frac{\gamma}{E_n^2} \tag{2.67}$$

$$c_{fn} = c_f\frac{\gamma}{E_n^2} \tag{2.68}$$

The obtained system describes an harmonic oscillator until the impact at t_j, when $\dot{\eta}_n$ and η_n present a jump. While a delta function source term determines a jump of the velocity, a jump in both velocity and displacement is generated by a force proportional to a delta function derivative. At the vortex time impingement t_j, both the mode amplitude and velocity present a discontinuous change, describing a typical *kicked oscillator* behavior.

The model is completed by a dynamic model for the vortex generation in unsteady flows. A quasi-steady hypothesis is considered for the vortex shedding in a flow with an oscillatory component [80]. At the obstacle position, the velocity at the outer edge of the boundary layer is composed by a mean flow velocity[10] and an acoustic component $(u(t) = \overline{u} + u^{'}(t))$. The vortex circulation growth can be expressed as:

$$\frac{d\Gamma}{dt} = \frac{u^2}{2} \tag{2.69}$$

In analogy with the steady case, the vortex separation is assumed to occur when the circulation reaches a critical value, defined by the momentary flow velocity. The

---

[10] The mean flow velocity is the velocity averaged over the duct cross section at the shedding point.

circulation critical value Γ_{sep} is defined as a function of the characteristic dimension D and of the steady-flow Strouhal number St:

$$\Gamma_{sep}(t_j) = u(t_j)\frac{D}{2\,St} \tag{2.70}$$

The dependence on both the mean flow velocity and on the oscillating component at the vortex generation point, underlines the acoustic oscillation feedback on the vortex shedding phenomenon. The feedback is then described by both the vortex growth model (eq. 2.69) and the critical circulation criterion (eq. 2.70). Obviously, this velocity dependence determines a vortex shedding oscillating behavior.

The model is capable of predicting the fundamental phenomena here considered, such as the lock-in phenomenon. The shed vorticity is neglected, and this makes the model not useful when such phenomenon is quite important (for example in case of anti-symmetric vortex shedding,...).

The determination of the introduced forcing coefficients strongly affects the model prediction of the acoustic instability.

The model has been completed to consider an unsteady heat release (common in liquid propellant motors with premixed combustor) [79]; in this case, the sudden heat addition is treated as an acoustic disturbance.

The fluctuating pressure time evolution is also provided. A signal spectral analysis provides the pressure oscillation frequency content.

The model appears able to qualitatively demonstrate aeroacoustic phenomena, such as the lock-in of the dominant sound frequency in a certain range of the mean flow velocity.

3

MATHEMATICAL MODELS AND THEIR NUMERICAL IMPLEMENTATION

An overview of SRM aeroacoustic mathematical model is provided in this chapter. A quasi-one dimensional aeroacoustic model is here presented (POX model); in addition to the description of each submodel that is part of the model, a particular attention is directed to the derivation of the adopted one-dimensional vorticity equation.

The structure of AGAR (Aerodynamically Generated Acoustic Resonance) model, a quasi-one dimensional model developed for the simulation of the flow time evolution in solid rocket motors, is then presented.

3.1 CONSERVATION LAWS AND CONSTITUTIVE EQUATIONS

The mass, momentum and energy conservation laws can be expressed as[1] [1, 52]:

$$\frac{\partial \rho}{\partial t} + \nabla \cdot (\rho \mathbf{u}) = 0 \tag{3.1}$$

$$\frac{\partial (\rho \mathbf{u})}{\partial t} + \nabla \cdot (\rho \mathbf{u}\mathbf{u}) = \nabla \cdot \mathbf{T} \tag{3.2}$$

$$\frac{\partial (\rho E)}{\partial t} + \nabla \cdot (\rho \mathbf{u} E) = -\nabla \cdot \mathbf{q} - \nabla \cdot (\mathbf{T} \cdot \mathbf{u}) \tag{3.3}$$

where E is the total energy per unit of mass. The momentum equations for a viscous flow are called the *Navier-Stokes equations*.

---

[1] The only surface forces are considered, while the volumetric body forces are neglected.

$\mathbf{T}$ is the fluid stress tensor, that can be decomposed into the pressure term and the viscous stress tensor $\boldsymbol{\tau}$:

$$\mathbf{T} = -p\mathbf{I} + \boldsymbol{\tau} \tag{3.4}$$

For a *Newtonian fluid*, the viscous stress tensor is expressed as:

$$\boldsymbol{\tau} = \lambda(\nabla \cdot \mathbf{u})\mathbf{I} + \mu \left[\nabla\mathbf{u} + (\nabla\mathbf{u})^T\right] \tag{3.5}$$

that represents a relationship between $\boldsymbol{\tau}$ and the deformation rate of the fluid element (*rate-of-strain tensor* $\left(\nabla\mathbf{u} + \nabla\mathbf{u}^T\right)$).

The momentum equation for an inviscid flow ($\boldsymbol{\tau} = 0$) becomes the *Euler's equation*:

$$\frac{\partial \rho\mathbf{u}}{\partial t} + \nabla \cdot (\rho\mathbf{u}\mathbf{u}) = -\nabla p \tag{3.6}$$

The heat flux, using the *Fourier's law*, can be related to the temperature gradient as:

$$\mathbf{q} = -K\nabla T \tag{3.7}$$

A *thermically perfect gas* is a gas that verifies the following *equation of state*:

$$p = \rho R T \tag{3.8}$$

for a perfect gas, both the specific internal energy and the specific enthalpy are function of temperature only[2]. A perfect gas where the specific heats, c_p and c_v, are constant is defined a *calorically perfect gas*.

If an adiabatic and frictionless flow is considered ($k = 0$ and $\mu = 0$), the flow is defined *isentropic* and the energy conservation equation becomes:

$$\frac{\partial(\rho E)}{\partial t} + \nabla \cdot (\rho\mathbf{u}H) = 0 \tag{3.9}$$

where H is the total enthalpy. The eq. 3.9 can be also expressed as:

$$\frac{\partial s}{\partial t} + \mathbf{u} \cdot \nabla s = 0 \tag{3.10}$$

where s is the entropy per unit of mass.

DILATATION RATE AND INCOMPRESSIBLE FLOW

The mass conservation law can be expressed in terms of the *material derivative*[3] as:

$$\frac{1}{\rho}\frac{D\rho}{Dt} = -\nabla \cdot \mathbf{u} = \Delta \tag{3.11}$$

where the *dilatation rate* $\Delta = -\nabla \cdot \mathbf{u}$ is defined as the rate of relative volume change. A null dilatation rate ($\Delta = -\nabla \cdot \mathbf{u} = 0$) characterizes an *incompressible flow*.

---

[2] $e = e(T)$

[3] $\frac{D}{Dt} = \frac{\partial}{\partial t} + \mathbf{u} \cdot \nabla$

SPEED OF SOUND

The *speed of sound* is defined as:

$$a = \sqrt{\left(\frac{\partial p}{\partial \rho}\right)_s} \tag{3.12}$$

For a calorically perfect gas, the speed of sound is a function of temperature only:

$$a = \sqrt{\gamma R T} = \sqrt{\gamma \frac{p}{\rho}} \tag{3.13}$$

If the eq. 3.12 is used, the expression of the equation of state (eq. 3.8), in differential form, becomes:

$$dp = a^2 d\rho + \left(\frac{\partial p}{\partial s}\right)_\rho ds \tag{3.14}$$

For an isentropic flow, the eq. 3.14 reduces to:

$$\frac{Dp}{Dt} = a^2 \frac{D\rho}{Dt} \tag{3.15}$$

where a^2 is not necessarily constant.

The Mach number is defined as the ratio of the flow velocity to the speed of sound:

$$M = \frac{u}{a} \tag{3.16}$$

3.2 ACOUSTIC FIELD

The vector velocity field $\mathbf{u} = \mathbf{u}(\mathbf{x}, t)$ can be considered divided into an irrotational and a solenoidal field:

$$\mathbf{u} = \nabla \phi + \nabla \times \mathbf{\Psi} \tag{3.17}$$

where ϕ is a *scalar velocity potential* and $\mathbf{\Psi}$ is a *vector stream function*. That components verify the following conditions:

$$\nabla \times (\nabla \phi) = 0 \tag{3.18}$$
$$\nabla \cdot \mathbf{\Psi} = 0 \tag{3.19}$$

It is possible to define a *potential line* as a line described by a constant value of the velocity potential; a *vortex line* is a line tangent everywhere to the $(\nabla \times \mathbf{u})$.

The velocity field of a *potential flow* is described by the only scalar velocity potential:

$$\mathbf{u} = \nabla \phi \tag{3.20}$$

From eq. 3.18 it is possible to obtain:

$$\nabla \times (\nabla \phi) = \nabla \times \mathbf{u} = 0 \tag{3.21}$$

and this implies that a potential flow is also an *irrotational flow*. For an incompressible potential flow, the velocity potential ϕ satisfies the Laplace equation:

$$\nabla \cdot \mathbf{u} = \nabla \cdot \nabla \phi = \nabla^2 \phi = 0 \tag{3.22}$$

The *acoustic field* is defined as the unsteady component of the irrotational flow field:

$$\mathbf{u}^{'} = \nabla \phi^{'} \tag{3.23}$$

A region that can be considered small if compared to acoustic wavelength is defined *acoustically compact region*[4] [5]. In an acoustically compact region the flow can be treated as an incompressible flow.

3.3 VORTICITY AND CIRCULATION

As seen in the previous paragraph (par. 3.2), the velocity field is considered composed by an irrotational and a solenoidal field, as indicated in eq. 3.17, 3.18, 3.19. While the acoustic field is related to the only velocity potential, it is possible to define a quantity described by the only vector stream function Ψ.

The *vorticity* $\boldsymbol{\omega}$ is defined as the curl of the velocity field and, if the eq. 3.18 is used, it can be expressed as[6]:

$$\boldsymbol{\omega} = \nabla \times \mathbf{u} = \nabla \times (\nabla \times \boldsymbol{\Psi}) = -\nabla^2 \boldsymbol{\Psi} \tag{3.24}$$

$\boldsymbol{\omega}$ is directed along the axis of fluid rotation. The vorticity is a Galilean invariant quantity, independent from the convection velocity.

An *irrotational flow* in each point verifies the following condition:

$$\boldsymbol{\omega} = 0 \tag{3.25}$$

A line tangent everywhere to the local vorticity is defined a *vortex line*. The surface composed by all the vortex lines passing through a closed curve is defined a *vortex flux* (tube). The strength of a vortex flux corresponds to the integral of the vorticity across a cross-section of the tube.

The *circulation* Γ is defined as:

$$\Gamma = \oint_{\partial S} \mathbf{u} \cdot dl \tag{3.26}$$

---

[4] With a similar definition it is possible to define a *compact source*.

[5] Such condition is verified, for example, in regions near singularities characterized by large spatial gradients.

[6] $\nabla \times (\nabla \times A) = \nabla(\nabla \cdot A) - \nabla^2 A$

where S is a closed curve in the flow field. The circulation can be expressed as a function of the vorticity $\boldsymbol{\omega}$ as follows:

$$\Gamma = \oint_{\partial S} \mathbf{u} \cdot dl = \int_S (\nabla \times \mathbf{u}) \cdot dS = \int_S (\boldsymbol{\omega} \cdot \mathbf{n})\ dS \tag{3.27}$$

and the vorticity can be viewed as a circulation per unit area.

3.4 VORTICITY EQUATION

The vorticity dynamics is described by the *vorticity equation*, obtained from the curl of the momentum conservation equation.

The momentum conservation equation (eq. 3.2) for a newtonian fluid (eq. 3.5, 3.4) becomes:

$$\frac{\partial(\rho\mathbf{u})}{\partial t} + \nabla \cdot (\rho\mathbf{u}\mathbf{u}) = \nabla \cdot \mathbf{T} = \nabla \cdot (-p\mathbf{I} + \boldsymbol{\tau}) \tag{3.28}$$

For a flow characterized by a constant dynamic viscosity ($\mu = const$), it is possible to consider the Helmholtz decomposition[7]:

$$2\nabla \cdot \boldsymbol{\tau} = \nabla(\nabla \cdot \mathbf{u}) + \nabla^2\mathbf{u} = 2\nabla(\nabla \cdot \mathbf{u}) - \nabla \times \boldsymbol{\omega} \tag{3.29}$$

that can be used in eq. 3.28 to obtain:

$$\frac{\partial(\rho\mathbf{u})}{\partial t} + \nabla \cdot (\rho\mathbf{u}\mathbf{u}) = (2\mu + \lambda)\nabla(\nabla \cdot \mathbf{u}) - \mu\nabla \times \boldsymbol{\omega} - \nabla p \tag{3.30}$$

With the mass conservation equation, eq. 3.1, and the Stokes hypothesis[8], the eq. 3.30 can be rewritten as:

$$\frac{D\mathbf{u}}{Dt} + \frac{1}{\rho}\nabla p = \frac{4}{3}\nu\nabla(\nabla \cdot \mathbf{u}) - \nu\nabla \times \boldsymbol{\omega} \tag{3.31}$$

where ν represents the cinematic viscosity.

For each term of eq. 3.31, the following relations are obtained:

$$\nabla \times \left(\frac{D\mathbf{u}}{Dt}\right) = \frac{\partial\boldsymbol{\omega}}{\partial t} + \nabla \times (\boldsymbol{\omega} \times \mathbf{u}) = \frac{D\boldsymbol{\omega}}{Dt} - \boldsymbol{\omega} \cdot \nabla\mathbf{u} + \boldsymbol{\omega}\nabla \cdot \mathbf{u} \tag{3.32}$$

$$\nabla \times \frac{\nabla p}{\rho} = \frac{\nabla\rho \times \nabla p}{\rho^2} \tag{3.33}$$

$$\nabla \times [\nabla(\nabla \cdot \mathbf{u})] = 0 \tag{3.34}$$

$$\nabla \times [\nabla \times \boldsymbol{\omega}] = \nabla(\nabla \cdot \boldsymbol{\omega}) - \nabla^2\boldsymbol{\omega} = -\nabla^2\boldsymbol{\omega} \tag{3.35}$$

---

[7] $\nabla^2 A = \nabla(\nabla \cdot A) - \nabla \times (\nabla \times A)$

[8] $\lambda = -\frac{2}{3}\mu$, $\nu = \frac{\mu}{\rho}$

The *vorticity equation* can be at last expressed as:

$$\frac{D\boldsymbol{\omega}}{Dt} = \frac{\partial\boldsymbol{\omega}}{\partial t} + \mathbf{u}\cdot\nabla\boldsymbol{\omega} = \boldsymbol{\omega}\cdot\nabla\mathbf{u} - \boldsymbol{\omega}\nabla\cdot\mathbf{u} - \frac{\nabla\rho\times\nabla p}{\rho^2} + \nu\nabla^2\boldsymbol{\omega} \tag{3.36}$$

that can be rewritten in divergence form as:

$$\frac{\partial(\rho\boldsymbol{\omega})}{\partial t} + \nabla\cdot(\rho\boldsymbol{\omega}\mathbf{u}) = \rho\boldsymbol{\omega}\cdot\nabla\mathbf{u} - \rho\boldsymbol{\omega}\nabla\cdot\mathbf{u} - \frac{\nabla\rho\times\nabla p}{\rho} + \mu\nabla^2\boldsymbol{\omega} \tag{3.37}$$

Different contributions can be distinguished in eq. 3.36.

VORTEX STRETCHING OR TILTING ($\boldsymbol{\omega}\cdot\nabla\mathbf{u}$) This term represents the vorticity stretching or tilting due to the velocity gradient. Its projection along the x-axis of a cylindrical coordinates system, then for plane or axisymmetric cases:

$$(\boldsymbol{\omega}\cdot\nabla\mathbf{u})\cdot\mathbf{n}_x = \omega_x\frac{\partial u_x}{\partial x} + \omega_r\frac{\partial u_x}{\partial r} + \frac{\omega_\theta}{r}\frac{\partial u_x}{\partial\theta} \tag{3.38}$$

permits to distinguish between:

- a first term that represents the vortex stretching due to a velocity gradient parallel to the vorticity direction. For the momentum conservation, if a vortex is stretched, its vorticity has to increase, with an auto-amplification that does not need of any external source.
- a second and a third term, related to transversal velocity gradients, that rotate the vorticity. These terms represent the vortex tilting.

FLUID COMPRESSIBILITY ($\boldsymbol{\omega}(\nabla\cdot\mathbf{u})$) This term corresponds to the stretching of vorticity due to the volume dilatation; the vorticity is concentrated or dispersed by the presence of a local compression or expansion.

BAROCLINIC TERM $\left(\frac{\nabla\rho\times\nabla p}{\rho^2}\right)$ The baroclinic term is a source of vorticity only in case of not parallel gradients of pressure and density. For barotropic fluid or in case of constant density the term does not exist.

VISCOUS TERM ($\nu\nabla^2\boldsymbol{\omega}$) This term accounts for the vorticity diffusion due to the viscous effects; for inviscid fluids the term does not exist. The generation or dissipation of vortical structures is a function of fluid motion.

If the viscous term and the baroclinic contribution are neglected, the vorticity equation can be simplified as:

$$\frac{\partial(\rho\boldsymbol{\omega})}{\partial t} + \nabla\cdot(\rho\boldsymbol{\omega}\mathbf{u}) = \rho\boldsymbol{\omega}\cdot\nabla\mathbf{u} - \rho\boldsymbol{\omega}\nabla\cdot\mathbf{u} \tag{3.39}$$

3.5 Aeroacoustic model

In the previous chapter, different reduced order models for the description of the acoustic resonance have been presented. The most important are Rossiter's model (par. 1.6) and the one-dimensional models developed by Jou and Menon(par. 2.10) and by Matveev (par. 2.11). The last two models can be compared to the aeroacoustic POX model here presented.

Due to the geometrical configuration of the combustion chamber of a SRM, the most important modes are longitudinal. This justifies the idea to use a one-dimensional model, thus neglecting the transverse modes.

The main idea to derive a quasi-one dimensional model for the flow field evolution in a solid rocket motor has been proposed by B. Favini and F. Serraglia. The vorticity dynamics is described by a Q-1-D model. Several exploratory studies have been performed in the last few years on their approach, on the quasi-one dimensional modeling of pressure oscillations and dealing with the analysis of the aeroacoustics of solid rocket motors.

As shown by the linearized analysis of Chu and Kovasznay [23], the propagation of small disturbances in a compressible fluid can be decomposed in three components: the acoustic, the entropy and the vorticity waves. In a recent research activity, a model for the analysis of the acoustic, entropy and vorticity modes has been presented [49]. A formal analysis and derivation of a quasi-one dimensional model has been also proposed [98].

An analytical model for the aeroacoustic coupling description is here presented and a quasi-one dimensional expression for the vorticity equation is derived. POX model has been already presented in some articles [43, 42], and a detailed description of each submodel can be found in the Internal Report for ESA-ESRIN [41]. POX model application to different test cases has been also provided in these papers.

The aeroacoustic model has to describe both the acoustic and the vortical waves, including their interactions. It has to consider the vortex generation, growth, convection and detachment, the excitation of the acoustic field by vortex impact/interaction with an obstacle and vortex shedding excitation by the acoustic field.

The POX model is composed by the following submodels:

- a model to determine the vortex dynamics (creation, growth, convection and destruction)
- a model to evaluate the acoustic field excitation by the vortex shedding phenomenon
- a model to estimate the acoustically forced vortex generation

The vorticity convection by the flow is described by a quasi-one dimensional equation. The acoustic mode excitation by the vortex impingement is modeled with the introduction of source terms in the gasdynamic model.

3.5.1 VORTICITY EQUATION

The expression of the vorticity equation for a newtonian fluid without viscous terms has been provided in eq. 3.39:

$$\frac{\partial(\rho\boldsymbol{\omega})}{\partial t} + \nabla \cdot (\rho\boldsymbol{\omega}\mathbf{u}) = \rho\boldsymbol{\omega} \cdot \nabla\mathbf{u} - \rho\boldsymbol{\omega}\nabla \cdot \mathbf{u} \tag{3.40}$$

where $(\boldsymbol{\omega} \cdot \nabla\mathbf{u})$ represents the stretching or tilting term and $(\boldsymbol{\omega}\nabla \cdot \mathbf{u})$ describes the compressibility effect.

For the POX model, the vorticity equation has to be expressed in a quasi-one-dimensional form, obtained with the expression of the eq. 3.40 in cylindrical coordinates and with the integration on a control volume.

VORTICITY EQUATION IN CYLINDRICAL COORDINATES

The first step to obtain the vorticity equation in a quasi-one-dimensional form, is the expression of eq. 3.40 in cylindrical coordinates.

Each term of the vorticity equation can be expressed in cylindrical coordinates as:

$$\begin{aligned}
\nabla \cdot (\rho\boldsymbol{\omega}\mathbf{u}) \quad = \quad & \left[\frac{\partial(\rho u_x \omega_x)}{\partial x} + \frac{\partial(\rho u_r \omega_x)}{\partial r} + \frac{1}{r}\frac{\partial(\rho u_\theta \omega_x)}{\partial \theta} + \frac{\rho u_r \omega_x}{r}\right] \mathbf{e}_x + \\
& \left[\frac{\partial(\rho u_x \omega_r)}{\partial x} + \frac{\partial(\rho u_r \omega_r)}{\partial r} + \frac{1}{r}\frac{\partial(\rho u_\theta \omega_r)}{\partial \theta} + \frac{\rho u_r \omega_r}{r} - + \frac{\rho u_\theta \omega_\theta}{r}\right] \mathbf{e}_r + \\
& \left[\frac{\partial(\rho u_x \omega_\theta)}{\partial x} + \frac{\partial(\rho u_r \omega_\theta)}{\partial r} + \frac{1}{r}\frac{\partial(\rho u_\theta \omega_\theta)}{\partial \theta} + \frac{\rho u_r \omega_\theta}{r} - + \frac{\rho u_\theta \omega_r}{r}\right] \mathbf{e}_\theta
\end{aligned}$$

$$\begin{aligned}
\rho\boldsymbol{\omega} \cdot \nabla\mathbf{u} \quad = \quad & \left[\rho\omega_x \frac{\partial u_x}{\partial x} + \rho\omega_r \frac{\partial u_x}{\partial r} + \frac{\rho\omega_\theta}{r}\frac{\partial u_x}{\partial \theta}\right] \mathbf{e}_x + \\
& \left[\rho\omega_x \frac{\partial u_r}{\partial x} + \rho\omega_r \frac{\partial u_r}{\partial r} + \frac{\rho\omega_\theta}{r}\frac{\partial u_r}{\partial \theta} - \frac{\rho u_\theta \omega_\theta}{r}\right] \mathbf{e}_r + \\
& \left[\rho\omega_x \frac{\partial u_\theta}{\partial x} + \rho\omega_r \frac{\partial u_\theta}{\partial r} + \frac{\rho\omega_\theta}{r}\frac{\partial u_\theta}{\partial \theta} - \frac{\rho u_r \omega_\theta}{r}\right] \mathbf{e}_\theta +
\end{aligned}$$

$$\begin{aligned}
\rho\boldsymbol{\omega}\nabla \cdot \mathbf{u} \quad = \quad & \left[\rho\omega_x \frac{\partial u_x}{\partial x} + \rho\omega_x \frac{\partial u_r}{\partial r} + \frac{\rho\omega_x}{r}\frac{\partial u_\theta}{\partial \theta} + \frac{\rho u_r \omega_x}{r}\right] \mathbf{e}_x + \\
& \left[\rho\omega_r \frac{\partial u_x}{\partial x} + \rho\omega_r \frac{\partial u_r}{\partial r} + \frac{\rho\omega_r}{r}\frac{\partial u_\theta}{\partial \theta} - \frac{\rho u_r \omega_r}{r}\right] \mathbf{e}_r + \\
& \left[\rho\omega_\theta \frac{\partial u_x}{\partial x} + \rho\omega_\theta \frac{\partial u_r}{\partial r} + \frac{\rho\omega_\theta}{r}\frac{\partial u_\theta}{\partial \theta} - \frac{\rho u_r \omega_\theta}{r}\right] \mathbf{e}_\theta +
\end{aligned}$$

The $\mathbf{e}_x$, $\mathbf{e}_r$ and $\mathbf{e}_\theta$ are the axial, radial and azimuthal versor respectively.

For an axisymmetric flow[9], it is possible to obtain a scalar equation in conservative form:

$$\frac{\partial(\rho\omega_\theta)}{\partial t} + \frac{\partial(\rho\omega_\theta u_x)}{\partial x} = -\frac{\partial(\rho\omega_\theta u_r)}{\partial r} - \rho\omega_\theta\frac{u_r}{r} - \rho\omega_\theta\frac{\partial u_r}{\partial r} - \rho\omega_\theta\frac{\partial u_x}{\partial x} \tag{3.41}$$

The terms on the right hand side of eq. 3.41 depend on u_r, r and on the radial derivative.

The $(\rho\omega_\theta u_r)_r$ term represents a radial addition while $\left(\rho\omega_\theta\frac{u_r}{r}\right)$ is the deformation contribution. The term $(\rho\omega_\theta u_{x,x} - \rho\omega_\theta u_{r,r})$ is related to the compressibility effect.

QUASI-ONE DIMENSIONAL FORM OF THE VORTICITY EQUATION

The vorticity equation has been expressed in cylindrical coordinates (eq. 3.41).

A cell of thickness Δx and with a mean value of the port area A_p is considered. The variables can be considered uniform on each cell.

With an integration on the port area, the following expression is obtained from eq. 3.41:

$$\begin{gathered}\int_{A_p}\frac{\partial(\rho\omega_\theta)}{\partial t}\,dA_p + \int_{A_p}\frac{\partial(\rho\omega_\theta u_x)}{\partial x}\,dA_p = \\ -\int_{A_p}\frac{\partial(\rho\omega_\theta u_r)}{\partial r}\,dA_p - \int_{A_p}\rho\omega_\theta\frac{u_r}{r}\,dA_p - \int_{A_p}\rho\omega_\theta\frac{\partial u_r}{\partial r}\,dA_p - \int_{A_p}\rho\omega_\theta\frac{\partial u_x}{\partial x}\,dA_p\end{gathered} \tag{3.42}$$

For the terms on the left side, the following expressions are considered:

$$\int_{A_p}\frac{\partial(\rho\omega_\theta)}{\partial t}dA_p = \frac{\partial(\overline{\rho\omega_\theta}A_p)}{\partial t} \tag{3.43}$$

$$\int_{A_p}\frac{\partial(\rho\omega_\theta u_x)}{\partial x}dA_p = \frac{\partial(\overline{\rho\omega_\theta u_x}A_p)}{\partial x} \tag{3.44}$$

From eq. 3.42, the vorticity equation can be written as:

$$\begin{aligned}\frac{\partial(\rho\omega_\theta A_p)}{\partial t} + \frac{\partial(\rho\omega_\theta u_x A_p)}{\partial x} &= -\int_{A_p}\frac{\partial(\rho\omega_\theta u_r)}{\partial r}\,dA_p - \int_{A_p}\rho\omega_\theta\frac{u_r}{r}\,dA_p \\ &\quad -\int_{A_p}\rho\omega_\theta\frac{\partial u_r}{\partial r}\,dA_p - \int_{A_p}\rho\omega_\theta\frac{\partial u_x}{\partial x}\,dA_p = \\ &\quad S_{\omega 1} + S_{\omega 2} + S_{\omega 3} + S_{\omega 4}\end{aligned} \tag{3.45}$$

that can be put in a compact form as:

$$\frac{\partial(\rho\omega_\theta A_p)}{\partial t} + \frac{\partial(\rho\omega_\theta u_x A_p)}{\partial x} = S_\omega \tag{3.46}$$

---

[9] For an axisymmetric case:$u_\theta = 0$, $\frac{\partial}{\partial\theta} = 0$

where the S_ω source term remains to be properly modeled[10]. The source terms represent the radial addition ($S_{\omega 1}$), the deformation contribution ($S_{\omega 2}$) and the compressibility effect ($S_{\omega 3}$ and $S_{\omega 4}$).

POX MODEL VORTICITY EQUATION

The deformation and the compressibility effects are not considered in the POX model, and the source terms $S_{\omega 2}$, $S_{\omega 3}$ and $S_{\omega 4}$, defined in eq. 3.45, are then neglected.

The only source term that has to be modeled is the radial addition term ($S_{\omega 1}$). Its effect is here related to the corner contribution; obstacle and parietal vortex shedding phenomena are not described. $S_{\omega 1}$ is then expressed as:

$$S_{\omega 1} = \rho \frac{d\Gamma}{dt} \tag{3.47}$$

and it exists only in correspondence of the corner where the vortex generation occurs.

With these assumptions, the vorticity equation becomes:

$$\frac{\partial(\rho \omega_\theta A_p)}{\partial t} + \frac{\partial(\rho \omega_\theta u_x A_p)}{\partial x} = \rho \frac{d\Gamma}{dt} \tag{3.48}$$

For a Q-1-D model, the notation can be simplified. The velocity component u_x can be indicated as u and the vorticity component ω_θ as ω. In order to further simplify the adopted notation, the Ω variable, that describes the vortex intensity, is defined as:

$$\Omega = \rho \omega A_p \tag{3.49}$$

The vorticity equation (eq. 3.48) can then be rewritten as:

$$\frac{\partial\, \Omega}{\partial t} + \frac{\partial\, (\Omega\, u)}{\partial x} = \rho\, \dot{\Gamma} \tag{3.50}$$

3.5.2 VORTEX CREATION AND GROWTH

In order to simulate the aeroacoustic coupling, the influence of the acoustic field on the vortex shedding phenomenon (vortex creation, growth and detachment) has to be described. This task is here obtained with a definition of the vortex properties as a function of time varying flow conditions; the vortex intensity is then dependent on the acoustic wave.

Clements [24] developed a study for the vortical structures behind a step. He showed that the vortex circulation growth can be defined as the shed vorticity, per unit of time, integrated over the boundary layer thickness.

---

[10] In a quasi-one dimensional model, the integral terms that exhibit u_r, r and radial derivative have to be modeled.

The velocity at the outer edge of the boundary layer is assumed composed by the mean flow velocity $\overline{u}$ and acoustic component $u^{'}$; the rate of circulation production can be approximated by:

$$\dot{\Gamma} = \frac{d\Gamma}{dt} = u^2(t) \tag{3.51}$$

A vortex is here described by its circulation and dimension. With the previous assumptions, the rates of variation, u_Γ for the circulation and $u_{l_{vs}}$ for the dimension, can be expressed as:

$$u_{l_{vs}} = u(t) \tag{3.52}$$

$$u_\Gamma = k_\Gamma \, u^2(t) \tag{3.53}$$

where k_Γ is a calibration parameter and u_Γ is a fraction of the rate of circulation production introduced in eq. 3.51.

The dimension and the circulation of a vortex are defined in terms of the flow velocity $u(t)$, underlining the acoustic influence on vortex shedding. Each time a vortex detachment occurs, both the vortex dimension and the circulation return to zero.

3.5.3 VORTEX DETACHMENT CRITERION

As the vortex creation and growth, the vortex shedding is also influenced by the external acoustic field. The detachment criterion is then also developed as a function of time varying flow conditions, underlining the role of the acoustic feedback on the vortex shedding dynamics.

The detachment criterion is defined from the local pressure evolution $p(t)$ at the shedding point[11]. The vortex separation is imposed each time the pressure at the shedding point satisfies the following conditions:

$$\frac{d^2p}{dt^2} = 0 \tag{3.54}$$

$$\frac{dp}{dt} \Rightarrow \text{local minimum} \tag{3.55}$$

In order to understand these conditions, both velocity and pressure evolutions are supposed to present a periodic sinusoidal behavior. In this case, a vortex detachment is imposed each time the $p(t)$, evaluated at the vortex generation point, presents a descending node (fig. 3.1). This assumption is in agreement with experimental and theoretical studies presented in literature [16, 35, 8], that state the occurrence of vortex detachment in correspondence of a positive velocity antinode (velocity relative maximum that corresponds to a pressure descending node).

This detachment criterion requires an initiation; the separation of the first two vortices is a forced separation to an imposed frequency.

---

[11] Any kind of control is imposed on the velocity behavior.

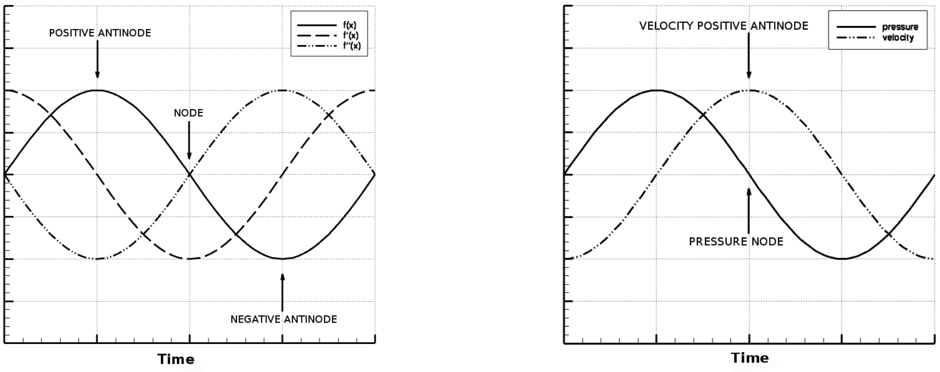

(a) Signal node and antinode.

(b) Pressure node and velocity antinode.

Figure 3.1: Vortex detachment condition.

3.5.4 ACOUSTIC EXCITATION

Each time a vortex interacts/impinges with an obstacle, it excites the acoustic field. This excitement is described by the introduction of source terms in the Euler equations (eq. 3.59). Three source terms $\dot{m}_{vs}$, $\dot{q}_{vs}$, $\dot{e}_{vs}$, respectively for the mass, momentum and energy equation, need to be modeled.

The $\dot{m}_{vs}$ is assumed to be zero, and the vortex impingement only generates momentum and energy source terms.

As shown by Howe's vortex sound theory [55], the sound production is due to the vortex crossing of the acoustic streamlines, and it is larger for larger angle between the two directions. These observations, combined with a dimensional analysis, determine the following expression for the source terms:

$$\dot{m}_{vs,i} = 0 \tag{3.56}$$

$$\dot{q}_{vs} = \Omega \frac{u}{A_p} \left(\frac{dA_p}{dx} \right)^2 \tag{3.57}$$

$$\dot{e}_{vs} = \rho u \dot{q}_{vs} = \frac{\rho \Omega}{A_p} \left(u \frac{dA_p}{dx} \right)^2 \tag{3.58}$$

The influence of the vortex intensity is represented by the Ω dependence, while the effect of the angle between the vectors is described by the $\frac{dA_p}{dx}$ term.

As shown in eq. 3.56, the sound generation is active each time a vortex interacts with a geometrical variation, characterized by a $\frac{dA_p}{dx} \neq 0$.

The vortices, convected by the mean flow, are expelled through the nozzle.

3.6 Structure of the AGAR model

AGAR (Aerodynamically Generated Acoustic Resonance) model [43, 42] is a *quasi-one-dimensional reduced order model* for the simulation of the flow time evolution in solid rocket motors. The analysis of the obtained pressure and thrust oscillations permits to characterize these oscillations, both for the amplitude and the frequency content.

Two-phase flow effects are neglected. In order to consider vortex shedding phenomenon due to purely acoustic phenomenon, the combustion heat release is assumed to have a negligible effect if compared to the acoustic phenomenon, that corresponds to neglect the effect of the combustion instability.

In order to simulate the fundamental phenomena that describe the functioning of a SRM, AGAR model requires the following submodels:

- a gasdynamic model to describe the flow evolution inside the combustion chamber (propagation of acoustic waves)
- a model to evaluate the combustion rate of ignited propellant grain to evaluate the mass addition from burning surface
- a model to determine the evolution of chamber geometry caused by the burning surface regression
- an aeroacoustic model able to consider both the influence of the acoustic field on vortex creation, growth and detachment and the excitation of the acoustic field by vortex shedding phenomenon

The two already developed models, *SPINBALL* [19, 37, 22, 20, 21, 94, 39, 38, 33, 32] and *GREG* [19, 37, 22, 20, 21], are respectively used as the gasdynamic and the grain burn back model. They are described in par. 3.7 and 3.8. The adopted aeroacoustic model is the POX model, already described in par. 3.5.

3.7 SPINBALL model

The gasdynamic model adopted in the AGAR code is the *SPINBALL* (Solid Propellant rocket motor INternal BALListics) model, created for the analysis of solid rocket motor internal ballistics.

It is already completely developed and a complete and detailed description of SPINBALL and SPIT can be found in [19, 37, 22, 20, 21, 94, 39, 38, 33, 32]. A brief description of SPINBALL main features is here provided.

SPINBALL derives from an improvement of SPIT (Solid Propellant rocket motor Ignition Transient) model, created for the analysis of the ignition transient of SRM. The fundamental upgrade of SPINBALL, compared to SPIT, is the numerical simulation of all the combustion time, quasi-steady state and tail-off phase included.

SPINBALL is a quasi-1D unsteady gasdynamic model that assumes the flow as a non-reacting mixture of perfect gases, with thermophysical properties variable in space and time. The governing equations are discretized by a Godunov-type scheme, accurate at first or second order in space and time.

Several sub-models complete the main model and permits the description of all the driving phenomena occurring in a solid rocket motor:

- an ignition model
- an heat transfer model for convection and radiation
- a propellant ignition criterion
- a cavity model (for submergence region and slots)
- a grain combustion model

3.7.1 Gasdynamic model

Each different phenomenon that characterize each phase of the SRM functioning has to be considered in a gasdynamic model for the description of the whole combustion time.

Different gases have to be considered during the ignition transient: the igniter gas, the pressurizing gas and the grain combustion products. The presence of such gases in the combustion chamber affects the waves propagation, the contact discontinuity velocity and the energy content. The variation of the thermophysical properties can be neglected during the quasi-steady state and the tail off phase. During these phases, the most important effect is related to the combustion process non-ideality. The evolution of the burning surface, both in space and time, has to be accurately evaluated during each phase.

SPINBALL uses an unsteady *quasi-one-dimensional* Eulerian model with mass, momentum and energy addition and a geometrical evolution both in space and time. The thermophysical properties of the mixture of ideal gases are variable in space and time; they are evaluated using a thermodynamic standard model for mixtures. Two phase flow effects are neglected and a mixture of non reacting perfect gases is considered.

The mass produced by the propellant combustion is supposed to be added without any axial momentum, while a proper model is considered for the igniter mass. Moreover, the reactions due to the grain combustion are supposed to occur in an ideal thin layer on the grain propellant surface.

While SPIT is developed considering a mass conservation equation for each specie of the mixture, SPINBALL uses an *infinite-gases formulation* [19]. It allows the analysis of thermophysical properties variable in space and time, and it is not interested in the spatial time evolution of the single mixture gas (igniter, pressurizing gas or propellant combustion products). The mixture properties of each cell, space and time variable, are evaluated considering the mass fluxes of the mixture, coming from adjacent cells, at the left and at the right, and from the source terms of the grain combustion reactions, the igniter and the cavity model. Six mass conservation equations are considered: for the j-th cell, the (j+1)-th cell, the (j-1)-th cell, the propellant combustion product gases, the igniter combustion product gases, the cavity mixture gases exchanged by cavity; a sketch can be found in fig. 3.2. The properties are obtained by a weight average with coefficients defined by the concentrations of each mixture at the considered time marching step. For each cell, the source terms and the mixture composition are updated at every time step, without taking into account the previous configuration that bring to the actual configuration.

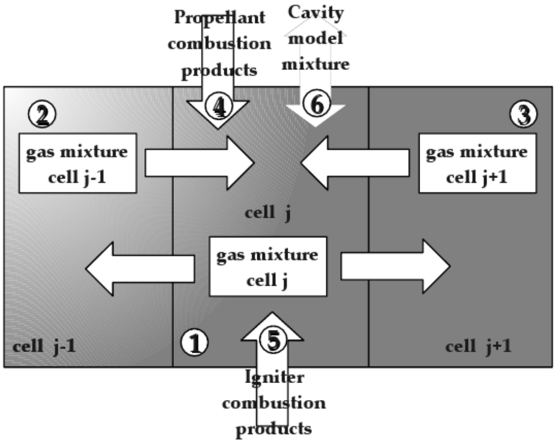

Figure 3.2: SPINBALL infinite gases formulation (figure from: [19]).

With the previous assumptions, the governing equations for a quasi-1D flow can be written as:

$$\begin{cases} \dfrac{\partial\left(\rho_i A_p\right)}{\partial t}+\dfrac{\partial\left(\rho_i u A_p\right)}{\partial x}=r_b P_b \rho_p+\dfrac{\dot{m}_s A_p}{V}+\dfrac{\dot{m}_{ig} A_p}{V}+\dot{m}_{vs} \qquad \text{for } i=1,\ldots,6 \\[2ex] \dfrac{\partial\left(\rho u A_p\right)}{\partial t}+\dfrac{\partial\left[\left(\rho u^2+p\right) A_p\right]}{\partial x}-p\dfrac{\partial A_p}{\partial x}=\dfrac{\dot{m}_{ig} A_p \bar{v}_{inj}}{V}+\dfrac{1}{2}\rho u^2 c_f+\dot{q}_{vs} \\[2ex] \dfrac{\partial\left(\rho e A_p\right)}{\partial t}+\dfrac{\partial\left[\left(\rho e+p\right) u A_p\right]}{\partial x}=r_b P_b \rho_p H_f+\dfrac{\dot{m}_{ig} A_p H_{ig}}{V}+\dfrac{\dot{m}_s A_p H_s}{V}+\dot{e}_{vs} \end{cases} \tag{3.59}$$

where A_p represents the combustion chamber port area, r_b the propellant burning rate, P_b the combustion perimeter, ρ_p the propellant density, $\dot{m}_s$ the cavity mass flow rate addition, $\dot{m}_{ig}$ is the igniter mass flow rate addition, v_{inj} the igniter jet velocity, c_f the friction coefficient[12], H_f is the grain combustion product enthalpy per unit mass, H_{ig} is

---

[12] The friction term is different from zero only at the nozzle and where the grain is not ignited.

the igniter product enthalpy per unit mass and H_s is the cavity gas enthalpy per unit mass.

The source terms $\dot{m}_{\nu s}$, $\dot{q}_{\nu s}$ and $\dot{e}_{\nu s}$ describe the acoustic field excitation by the vortex shedding. They have been described in par. 3.5.4 and their expressions can be seen in eq. 3.56. For the mass conservation equation, the source term is assumed $\dot{m}_{\nu s} = 0$.

The chemical reactions occurring in a solid rocket motor can not reach the ideal equilibrium point; this chance is considered by the introduction of a combustion efficiency. Once the grain combustion thermophysical properties are evaluated from the local pressure value, the combustion efficiency is extracted from a chemical equilibrium table.

The evolution of the cross-sectional port area evolution A_p does not include slots and submergence regions; their presence is treated by the mass and energy equation source terms.

3.7.2 INITIAL AND BOUNDARY CONDITIONS

The initial conditions correspond to the physical and geometrical conditions of the motor start-up. The geometrical configuration is determined by the grain, the nozzle and the igniter geometrical data. Other initial conditions are related to the initial state of the pressurizing gas.

The boundary conditions have to be distinguished before and after the seal breaking. The combustion chamber head section is always described by rigid wall conditions. Different boundary conditions characterize the aft end. A seal, located in the nozzle throat, protects the combustion chamber from the external contaminations and facilitates the motor pressurization. Once a certain differential pressure[13] is reached, the seal breaking occurs; from this point, the flow starts to exit from the combustion chamber through the nozzle. Therefore, the nozzle exit is described by wall conditions up to the seal breaking and by sonic conditions after the nozzle seal rupture.

3.7.3 CAVITY MODEL

The evaluation of the state inside both slots and submergence regions is obtained by means of a cavity model[14].

AGAR model treats the presence of a cavity with a 0-dimensional model. Two ordinary differential equations (ODEs), mass and energy conservation equations, are obtained by a volume average over the cavity volume. The model, derived from a SPIT upgrade, allows to treat variable thermophysical properties.

---

[13] The differential pressure is related to the difference between the internal and the external pressure value.

[14] A cavity is characterized by the presence of low speed flows and of recirculating zones.

At the n-th time step, it is possible to assume that the cavity properties, the grain propellant mass addition and the main flow field properties are known. The coupling between the flow field and the cavity state is ensured by evaluating the mass and energy exchange as a function of their pressure unbalance. The conservation equations are averaged on the cavity volume and the mass exchange is calibrated in order to obtain a delay corresponding to a finite mass transfer velocity. The adopted calibration parameter is indicated as α_{cav}.

3.7.4 BURNING RATE MODEL

Due to the propellant grain combustion, the burning surface recedes along a direction perpendicular to the surface itself. The *burning rate* is defined as the burning surface rate of regression.

The combustion processes are assumed very fast and occurring in an ideal thin layer close to the propellant surface. It's then possible to consider a non reacting mixture of perfect gases in the combustion chamber. The propellant combustion products are considered at chemical equilibrium.

The used burning rate model derives from semi-empirical expressions, where some parameters have to be imposed. They are generally obtained from experimental investigations.

The burning rate is composed by three different contributions: the quasi-steady term, related to the combustion chamber pressurization, the non-linear unsteady term, due to the pressurization rate, and the erosive term, caused by crosswise flowfield and by turbulence effects.

The non-linear unsteady contribution is not considered in the model; the total burning rate r_b is then expressed as:

$$r_b = r_{b_p} + r_{b_e} \tag{3.60}$$

where r_{b_p} is the quasi-steady term and r_{b_e} represents the erosive contribution.

The quasi-steady burning rate r_{b_p} is evaluated by the semi-empirical APN model, expressed by the Veille's - de Saint Robert's law [96] as:

$$r_{b_p} = a \left(\frac{p}{p_{ref}} \right)^{n} \tag{3.61}$$

where two semi-empirical parameters, a and n, are introduced and p_{ref} is a reference pressure. The values of a[15] and n[16] are obtained from experimental tests, and they depend on propellant composition and on its initial temperature.

---

[15] $a = a(p, T_i)$

[16] $n = n(p)$

The erosive burning rate r_{b_e} is described by Lenoir - Robilland's model, LR model, as modified by Lawrence[17] [96]:

$$r_{b_e} = \alpha \frac{(\rho u)^{0.8}}{D_h^{0.2}} e^{-\frac{\beta r_b \rho_p}{\rho u}} \tag{3.62}$$

$$= 0.0288 C_p \mu^{0.2} Pr^{-2/3} \frac{1}{\rho_p C_{pr}} \frac{T_f - T_s}{T_s - T_i} \tag{3.63}$$

$$D_h = \frac{4A_p}{P_w} \tag{3.64}$$

where D_h is the hydraulic diameter, Pr the Prandtl number, μ the dynamic viscosity, P_w the wet perimeter, T_f the final temperature, T_i the initial temperature and T_s is the propellant surface temperature. α and β are empirical parameters.

3.7.5 HEATING AND IGNITION OF THE PROPELLANT SURFACE

Only brief notes are here presented about the model adopted for the propellant surface heating and ignition. A detailed description and analysis can be found in [94, 39, 38, 33, 32].

IGNITION CRITERION

The propellant surface is considered ignited when the surface temperature attains an assigned value, the ignition temperature. A simple empirical dependence of the ignition temperature on the local pressure level has been considered.

CONDUCTION HEAT TRANSFER MODEL

An accurate evaluation of the grain pre-heating is required to obtain a precise ignition transient reconstruction.

The impingement of the igniter jets on the propellant surface defines the *impingement region*. This impingement is the main driving mechanism of the motor start-up. Because of the particular flow condition, a specific heat transfer model has to be considered. The impingement region is supposed to be circular, and its diameter is considered proportional to the igniter jet diameter. The heat exchange of this region is described by Martin's formulation.

The convective heat transfer that characterizes the standard region is evaluated by Gnielinsky's semi-empirical model.

RADIATIVE HEAT TRANSFER MODEL

In each region characterized by very low flow velocity, the convective heat transfer is negligible and the propellant ignition is mainly influenced by radiative heat transfer. A

---

[17] Lawrence's modification is useful for large solid rocket motor.

specific Gas Radiative Coefficient GRC is defined, and its expression combines the effects related to gas emissivity, trasmissivity and surface absorptivity. Further, the GRC is a function of the radiative gas pressure and temperature.

PROPELLANT HEATING EVALUATION

The determination of the propellant surface heating requires a specific model for the evaluation of the conduction heat transfer into the propellant grain. The classical unsteady 1D Fourier equation is coupled with the heat convection equation. An ordinary differential equation is obtained for the time history of the propellant surface temperature.

3.7.6 NUMERICAL INTEGRATION TECHNIQUE

A finite volume Godunov's scheme is used for the numerical discretization of the system in eq. 3.59. The first or second order accurate (ENO, Essentially Non Oscillatory) scheme is coupled with an exact Riemann solver, modified to take into account a mixture of different gases. The main characteristics of this method are the robustness and the capability to treat flowfield with propagation phenomena, strong discontinuities and source terms.

Godunov's scheme discretizes the conservation equations from the mathematical properties of the integrated PDEs. It can be considered a generalization of the characteristic method for problems with discontinuities; the weak solution that satisfies the entropy condition is naturally selected, even for problems with strong discontinuities.

The Euler's conservation equations can be written as:

$$\begin{cases} \dfrac{\partial U}{\partial t} + \dfrac{\partial F(U)}{\partial x} = 0 \\ \\ U(0,x) = U_0(x) \end{cases} \tag{3.65}$$

where the variables U and the fluxes F are respectively expressed as:

$$U = \begin{bmatrix} \rho \\ \rho u \\ \rho E \end{bmatrix} \tag{3.66}$$

$$F = \begin{bmatrix} \rho u \\ \rho u^2 + p \\ \rho u H \end{bmatrix} \tag{3.67}$$

The PDEs system, eq. 3.65, is non-linear, unsteady and hyperbolic[18]. It is closed by appropriate boundary conditions.

A uniform grid is considered $\left(\left[x_{j-\frac{1}{2}}; x_{j+\frac{1}{2}}\right]\right)$.

---

[18] The all eigenvalues of the Jacobian matrix $\left[A(U) = \frac{\partial F}{\partial U}\right]$ are real.

With an integration of the the system in a generic space and time domain $\left[x_{j-\frac{1}{2}}; x_{j+\frac{1}{2}}\right] \times [0; \Delta t]$, the following expression is obtained:

$$\int_{x_{i-1/2}}^{x_{i+1/2}} U(x, t+\Delta t) dx - \int_{x_{j-1/2}}^{x_{j+1/2}} U(x, t) dx + \int_{t}^{t+\Delta t} \left[F\left(x_{i+1/2}, t\right) - F\left(x_{i-1/2}, t\right)\right] dt = 0 \quad (3.68)$$

With the average of the conservative variable $\overline{U}$, evaluated in the generic domain $\left[x_{j-\frac{1}{2}}; x_{j+\frac{1}{2}}\right]$, the variable U at the time step n is expressed as:

$$U_j^n = \overline{U}_j\left(t\right) = \frac{1}{\Delta x} \int_{x_{j-1/2}}^{x_{j+1/2}} U\left(x, t\right) dx \quad (3.69)$$

The variable U at the time step $n+1$ is obtained by a discretized time marching solution:

$$U_j^{n+1} = U_j^n - \frac{\Delta t}{\Delta x}\left[F_{j+1/2}^n - F_{j-1/2}^n\right] \quad (3.70)$$

In order to ensure the algorithm stability, the time step Δt must be related to the spatial discretization Δx. The evaluation of the time step Δt has to guarantee that the three waves, generated at one interface for each Riemann's problem, do not reach the contiguous interfaces. This condition generates constant interface fluxes during the time interval Δt. Indicated with λ_{max} the fastest wave speed originated by Riemann's problem, the *Courant Friedrichs Lewy (CFL) condition* corresponds to impose the following condition:

$$\Delta t^n \leqslant \frac{\Delta x}{\lambda_{max}^n} \quad (3.71)$$

The space support x is discretized by N finite volumes of width Δx [19]. The approximation $\widetilde{U}(x, t)$ is obtained with a projection of the exact solution $U(x, t)$ on the discretized grid:

$$\widetilde{U}\left(t, x\right) = \sum_{j=1}^{N} \overline{U}_j\left(t\right) \cdot I_j\left(x\right) \quad (3.72)$$

where $\bar{U}_j(t)$ is the average of the exact solution at the time t over the j-th cell and $I_j(x)$ is the projector of the exact solution over the j-th cell.

VARIABLES RECONSTRUCTION AT THE CELL INTERFACES

For a given time step, a certain variables distribution in the cell has to be provided. It is used, in a second step, for the evaluation at the interfaces of the solution discontinue values.

---

[19] Δx can be non uniform.

The solution obtained by Godunov's scheme is a piecewise constant function, with constant cell values (projection of the solution on the cell points by the I_j operator). If a constant reconstruction is adopted, it is the U_j^n approximation. If a linear piecewise is required, a second order accuracy in space in used (the slope of the linear cell is determined with respect to the average value U_j, U_{j-1} and U_{j+1}). The use of linear reconstruction can generate spurious non physical oscillations, *Gibbs's phenomenon*, involving an unstable computed solution. A slope limiter, *Total Variation Decreasing* (TVD), has to be used to guarantee the numerical scheme stability.

LOCAL EVOLUTION OF THE SOLUTION AT THE CELL INTERFACES TO FIND INTERFACES FLUXES

For the local evolution evaluation, the flux vector has to be evaluated at the interfaces. The reconstruction provides two values of the solution at the same interface $x_{j+1/2}$ ($U^L_{(j+1)+1/2}$ and $U^R_{j+1/2}$). These values generate a Riemann's problem and its solution determines the flux value $F_{j+1/2}(t)$ at the interface.

TIME INTEGRATION OF THE CELL AVERAGE VARIABLES

A constant solution of the Riemann's problem determines constant fluxes in the time interval $[t^n; t^n + \Delta t]$. The eq. 3.70 provides a time marching expression for the solution computing.

The eq. 3.73 shows the obtained discretization for the system eq. 3.59, where S indicates the source terms.

$$
\begin{gathered}
\left\{ \begin{array}{c} \rho_i A_p \\ \rho u A_p \\ \rho E A_p \end{array} \right\}_j^{n+1} = \left\{ \begin{array}{c} \rho_i A_p \\ \rho u A_p \\ \rho E A_p \end{array} \right\}_j^{n} + \\
-\frac{\Delta t^n}{\Delta x} \left\{ \begin{array}{c} (\rho_i u A_p)^n_{j+\frac{1}{2}} - (\rho_i u A_p)^n_{j-\frac{1}{2}} \\ \left[\left(\rho u^2 + p\right) A_p\right]^n_{j+\frac{1}{2}} - \left[\left(\rho u^2 + p\right) A_p\right]^n_{j-\frac{1}{2}} + p_j^n \left(A^n_{p,j+\frac{1}{2}} - A^n_{p,j-\frac{1}{2}}\right) \\ (\rho u H A_p)^n_{j+\frac{1}{2}} - (\rho u H A_p)^n_{j-\frac{1}{2}} \end{array} \right\} + \\
+ \left\{ \begin{array}{c} S_i^n \\ S_2^n \\ S_3^n \end{array} \right\}
\end{gathered}
\tag{3.73}
$$

3.8 GREG MODEL

The *grain burn back analysis* is the study of the burning surface evolution with time. It makes available all the geometrical parameters required for the solution of the internal ballistics.

In AGAR code, the used grain burn back model is the 3D numerical model *GREG* (Grain REGression); a complete description of the model can be found in [19, 37, 22, 20, 21].

The use of a 3D model allows the analysis of complex 3D grain shapes (i.e: finocyl grains), also for 0-D or 1-D flow models. GREG provides to AGAR all the required Q-1D geometrical parameters, the space and time evolution of port area, cavities, burn and wet perimeter.

GREG model has to be coupled with the unsteady flowfield model. When the reduction of the computational costs is a priority, a decoupling between the grain burn back model and the flowfield model can be considered. An example is represented by the *off-line coupling* realized between SPINBALL and GREG. Before the execution of the numerical simulation, GREG model evaluates the grain burning surface, obtained with the assumption of a constant burning rate. This operation is made only once, and the model generates tables containing all the geometrical properties. During the simulation, SPINBALL uses the data contained in these tables with an interpolation procedure; the considered local burning rate is obtained from the APN and LR models (par. 3.7.4). The axial variation of the burning rate is considered during the flowfield solution. This approach introduces relevant approximations if the burning rate is strongly variable along the motor axis; these approximations can be high during the transient and the tail off phase, but they are negligible during the quasi-steady state.

3.9 COMMENTS

The quasi-one-dimensional vorticity equation adopted in the AGAR model is derived through a formal analytical process; the only assumption that has been introduced concerns the circulation definition of eq. 3.51.

The source terms of eq. 3.56, 3.57, 3.58 describe the coupling between the acoustics and the vorticity field. Their expression is obtained by using a phenomenological analysis and dimensional considerations.

These aspects show that the encountered difficulties are not related to the derivation of the one-dimensional model but to the nature of the vorticity field.

As noted, only the corner vortex shedding has been considered. Besides parietal and obstacle vortex shedding, other aspects are neglected, such as radial mass addition effect, tilting effects, combustion instabilities,...

4

NUMERICAL SIMULATION OF OSCILLATORY COLD FLOWS

In this chapter a validation test case for AGAR model is presented: the simulation of a cold flow in an axisymmetric ramjet combustor. The same test case proposed by Jou and Menon is performed and a direct comparison with their results is presented.

This cold flow simulation represents a simplified case, if compared to the simulation of the flow in a solid rocket motor. In this case any radial mass addition and combustion effect is considered. As for the several tests and simulations that have been performed employing cold flows, the aim is the description of the pure aeroacoustic coupling mechanism.

4.1 JOU AND MENON'S TEST CASE

Jou and Menon [81, 63] proposed a *one-dimensional model* for the analysis of the results obtained by full numerical simulations. The model also permits the extraction of informations on the physical processes that lead to the presence of pressure fluctuations. It describes the coupled modes and the interaction between the vortex dynamics and acoustic waves, providing an estimation of the pressure oscillation frequency. The model has been already described in par. 2.10, and it has been tested with the simulation of cold flows in an axisymmetric ramjet combustor.

The use of cold flow makes it possible to describe the pure aeroacoustic coupling neglecting the effects due to combustion instabilities. Any radial mass addition is present and the only corner vortex shedding is considered. The analysis of a such simple case allows the description of the simple coupling of vortex dynamics and acoustic waves; it represents a suitable tool in order to verify AGAR model behavior, characteristics and features, as well as to analyze its description of the aeroacoustic coupling.

A study on the effect of different inlet flow Mach numbers completes the analysis; Mach changes are achieved with variations of the nozzle throat area.

The data reported by Jou and Menon in their works [81, 63] do not permit a complete reconstruction of the performed test case. Some assumptions have to be made to complete the data set; obviously, the introduction of such hypotheses can influence the obtained results, especially for the quantitative aspects. The qualitative description of the considered phenomena is instead not affected.

The analyzed geometrical configuration is presented in fig. 4.1. A uniform grid of 400 cells is used for AGAR simulation ($dx = 0.0014$ m). With respect to the non dimensional axis, the step is located at 0.358 while the throat section is at 0.885. The step is discretized by 20 cells, and it is characterized by a height/length ratio of $h/l = 2.268$. Any information is provided about the nozzle profile, except the area values in the throat and in the exit section. The convergent and the divergent profile is then arbitrarily reconstructed.

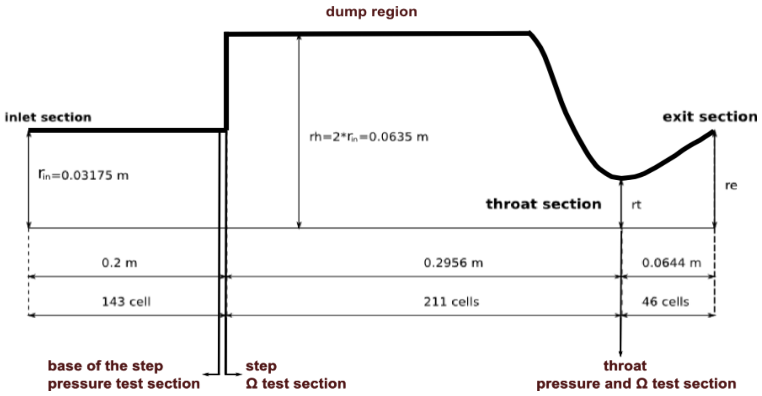

Figure 4.1: Test case geometry.

The used initial conditions are that of a quiescent flow at stagnation conditions.

Subsonic inflow conditions are imposed at the inlet entrance. As done by Jou and Menon, the flow at the inlet is assumed at an imposed total pressure and temperature, but the cited articles do not mention the adopted total condition at the inlet. It is impossible to deduce the pressure value and the choice is fully arbitrary. The total temperature value is instead determined by using the system acoustic frequency obtained by Jou and Menon. The half of the acoustic wavelength is defined by the distance between two pressure nodes, so that it is not related to the distance between the inlet and the throat section. While the nozzle throat correspond to a nodal point, another node is located in the dump region [81, 63].

The imposed value of total pressure and temperature are $T_0 = 290\mathrm{K}$ and $P_0 = 10\ \mathrm{bar}$. It is obviously expected that the pressure value can somehow determines quantitative differences with respect to Jou and Menon's results.

The start up of the simulation presented by Jou and Menon is obtained with an impulsive lowering of the exit pressure. Once the flow is established, the exit pressure is further lowered, and downstream of the throat the supersonic flow is reached. Then, if required, the inlet flow Mach number value can be changed by modifying the nozzle throat area. A different start-up method is used for AGAR simulation. The system is considered isolated from the external ambient by a seal, located in the throat section. At the initial configuration, the internal pressure is considered equal to the inlet total pressure, while the outside is assumed at the atmospheric pressure. After the seal breaking, the throat section impulsively reaches the sonic condition. Only when the system attains the stationary conditions, the vortex shedding is activated.

The fundamental aspect characterizing the pressure oscillation is the frequency content. The frequency content of a signal can be obtained by using the Fourier transform (a description of the Fourier transform can be found in appendix A).

Jou and Menon's [81, 63] reported results describe the frequency content of the pressure oscillation, evaluated at the base of the step, and of the vorticity fluctuation, considered at the nozzle entrance. In addition to these test sections, AGAR simulation results are also analyzed in terms of pressure oscillation at the nozzle throat section, and of vorticity fluctuation at the vortex detachment point.

In the POX model, the vorticity field is described by the Ω variable, as defined in eq. 3.49; the vorticity frequency content is then obtained by the Ω fluctuation analysis.

A comparison of both vorticity and pressure oscillations, evaluated in different sections of the system, provides additional informations about the considered phenomena and their dynamics.

The frequency of a resonant oscillation primarily depends on the speed of sound, and only weakly on the flow Mach number, while the frequency of a coupled mode is substantially function of the Mach number. The analysis of different inlet flow Mach numbers allows the identification of the nature of each frequency peak. Jou and Menon considered two different values: $M_{in} = 0.32$ and $M_{in} = 0.44$; the same values are analyzed with AGAR model simulations. A further step has been performed in order to determine the inlet Mach number involving the resonance condition.

In the following paragraph, a direct comparison of AGAR simulations with Jou and Menon's results is presented.

4.2 AGAR SIMULATION: INLET MACH NUMBER $M_{in} = 0.32$

The first test case analyzed by Jou and Menon is characterized by an inlet flow Mach number of $M_{in} = 0.32$. This value is obtained with a nozzle throat section of $A_t = 0.001649\ m^2$; the corresponding geometrical configuration can be seen in fig. 4.2.

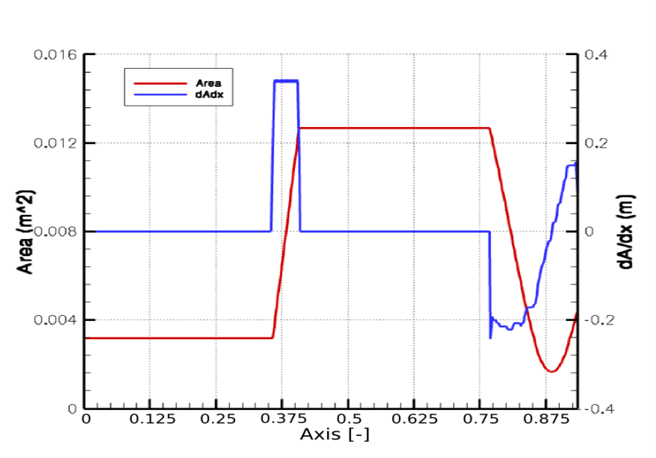

Figure 4.2: Geometrical characteristics in AGAR discretization.

The dA/dx distribution is directly related to the source terms that describe the acoustic field excitation (par. 3.5.4); each interaction with a $dA/dx \neq 0$ represents an acoustic source. As shown in fig. 4.2, two regions have to be considered in this sense, the nozzle inlet and the step.

4.2.1 VORTEX DETACHMENT CRITERION

The vortex detachment criterion adopted in AGAR model has been presented in par. 3.5.3.

The shedding conditions of this simulation are shown in fig. 4.3. The red lines correspond to the separation of a vortex, occurring in correspondence of a zero pressure second derivative and of a minimum of the first one. The pressure and velocity time evolutions do not exhibit sinusoidal behavior, and the imposed conditions determine a separation corresponding to a pressure negative antinode and a positive velocity antinode[1] .

4.2.2 SOURCE TERMS FOR ACOUSTICS EXCITATION AND VORTICITY EQUATION

The vorticity equation source term only exists at the vortex detachment point, the step position, as shown in fig. 4.4.

---

[1] From literature, the condition of positive velocity antinode is a forcing condition for vortex detachment.

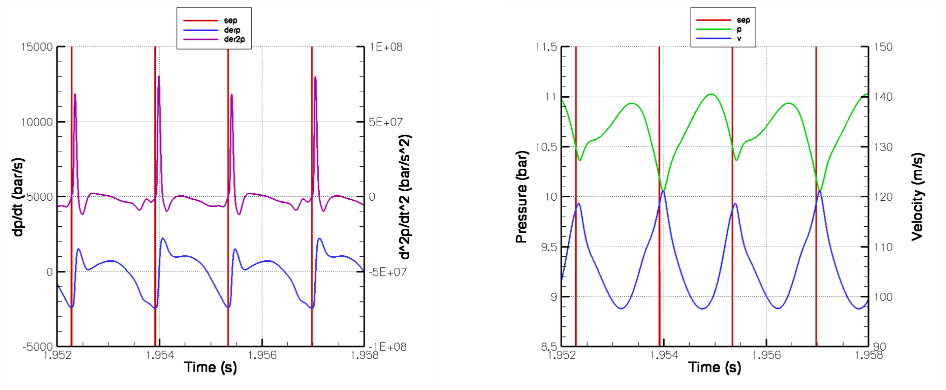

(a) Pressure time derivatives (b) Pressure and velocity

Figure 4.3: Vortex detachment condition at vortex detachment cell.

The source terms related to the acoustics excitation have a contribution in that regions characterized by a $dA/dx \neq 0$. In fig. 4.4 it can be seen that the acoustics is excited by vortex/obstacle interaction at the step and at the nozzle inlet.

4.2.3 Vorticity (Ω) distribution

The presence of a vortex corresponds to a vorticity (Ω) distribution local maximum, and the maximum number corresponds to the number of vortices in the system. In fig. 4.5, the vorticity (Ω) distribution obtained for this simulation is shown; the presence of six vortices can be noted.

The "non regular" envelopment of the vorticity distribution, characterized by different amplitudes and frequencies, underlines the non resonant configuration of this test case. A careful analysis shows the existence of different vortex detachment frequencies, with corresponding different intensities and dimensions of the separated vortices, as shown in fig. 4.5.

4.2.4 Pressure and velocity distribution

The pressure, velocity, speed of sound and Mach number distributions can be seen in fig. 4.6. The pressure distribution shows the presence of a node[2] at ~ 0.575 of the non dimensional axis; this node corresponds to an antinode in the velocity and Mach number distribution. The presence or these nodes/antinodes is clearly visible in the pressure and velocity time derivative distributions[3], fig. 4.7.

---

[2] A node corresponds to a point that exhibits a constant pressure value.

[3] The time derivative exhibits a node where a point presents a constant zero value.

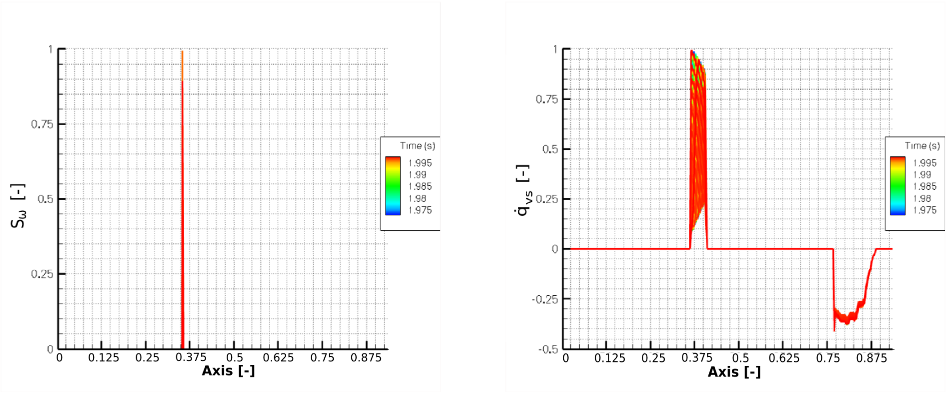

(a) Non dimensional vorticity (Ω) equation source term

(b) Non dimensional momentum equation source term

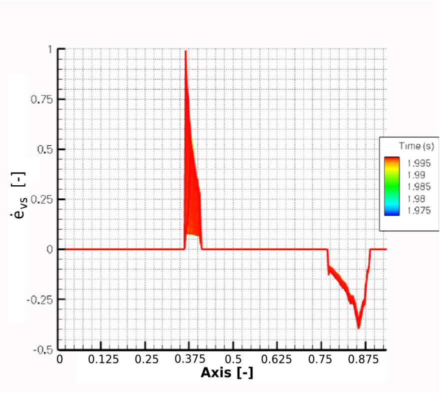

(c) Non dimensional energy equation source term

Figure 4.4: Source terms for vorticity (Ω) equation and acoustics excitation.

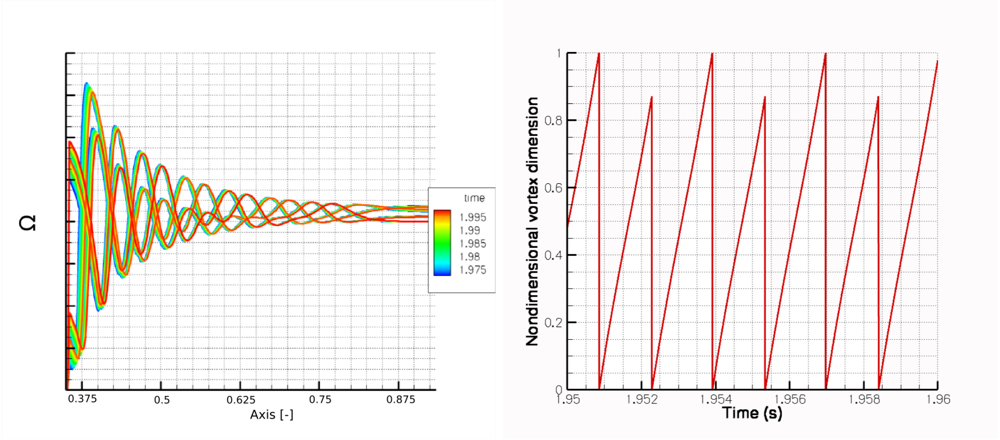

(a) vorticity (Ω) distribution (b) Vortex dimension

Figure 4.5: Vorticity (Ω) distribution and vortex dimension.

The relative position of acoustic node (~ 0.575) and vortex shedding point (~ 0.35) is a factor affecting the acoustic resonance; it is more effective if the detachment point is in correspondence of a pressure node.

4.2.5 PRESSURE AND VORTICITY (Ω) FLUCTUATIONS

The main and most important result is represented by the oscillation frequency content. In order to perform a direct comparison with the results presented by Jou and Menon, the pressure oscillation is evaluated at the base of the step, while the vorticity is analyzed at the nozzle throat section. A description of the dynamics of these phenomena is obtained also considering the pressure in the throat section and the vorticity at the vortex detachment point. In AGAR model the vorticity is represented by the Ω variable.

AGAR results, of both pressure and vorticity fluctuations, are shown in fig. 4.8; the red data are the same analyzed in Jou and Menon's study. Both the pressure and the vorticity exhibit a damping effect with the flow motion towards the nozzle. Different sections of the system are not characterized by the same frequencies.

The time variable amplitude, of both Ω and pressure fluctuation, describes a typical non resonant configuration.

The frequency content of each signal is shown in fig. 4.9. The frequency peaks obtained by Jou and Menon's simulation are indicated with the black vertical line.

The pressure at the base of the step exhibits two acoustic peaks. The first acoustic mode frequency is at ~ 650 Hz, and it is the most important contribution; the second acoustic mode presents a minor peak at ~ 1300 Hz. Two other peaks, ~ 330 and ~ 980 Hz, are related to the vortex shedding. The acoustic peaks are the fundamental

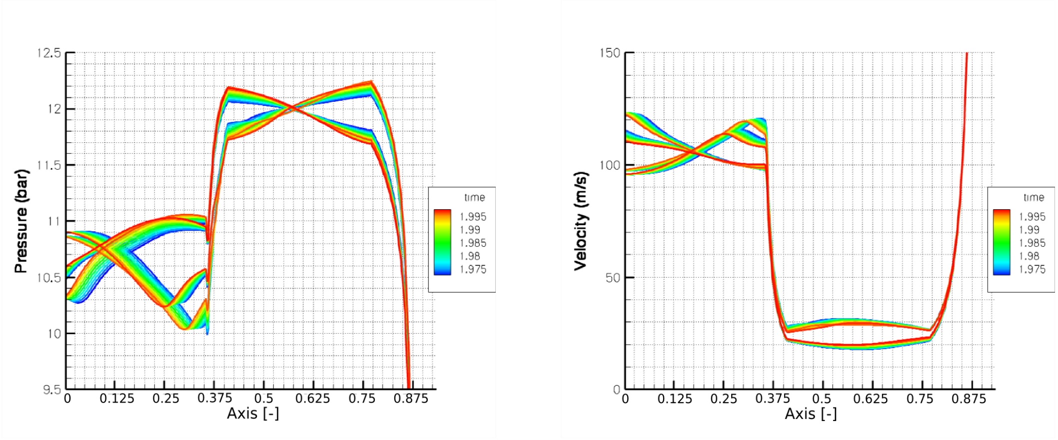

(a) Pressure (b) Velocity

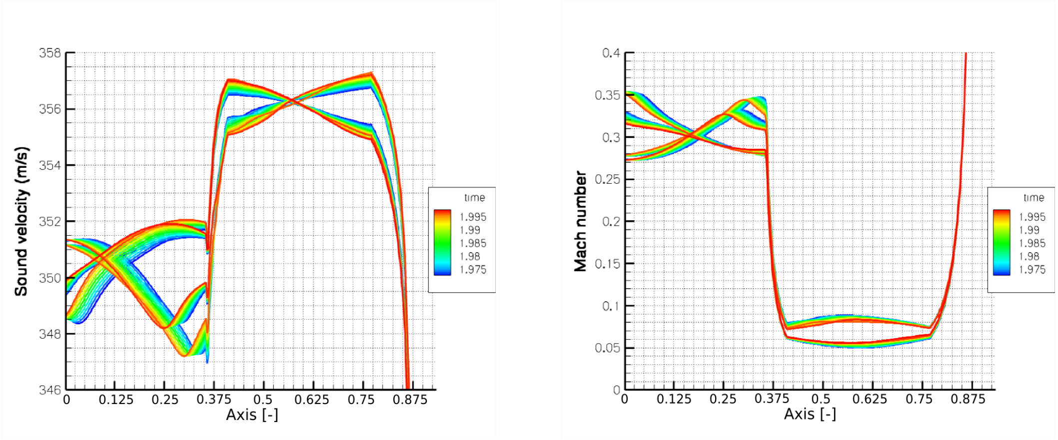

(c) Sound velocity (d) Mach number

Figure 4.6: Pressure, velocity, sound velocity and Mach number distribution.

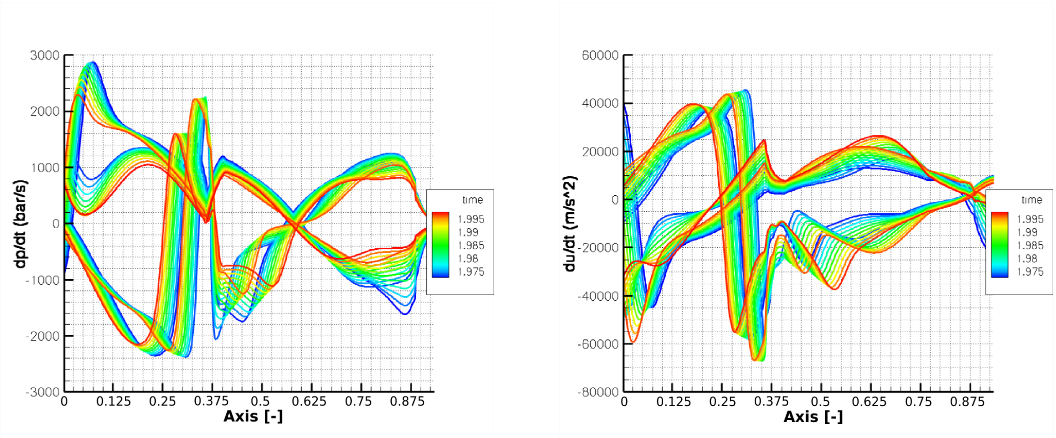

(a) Pressure time derivative (b) Velocity time derivative

Figure 4.7: Pressure and velocity time derivative distribution.

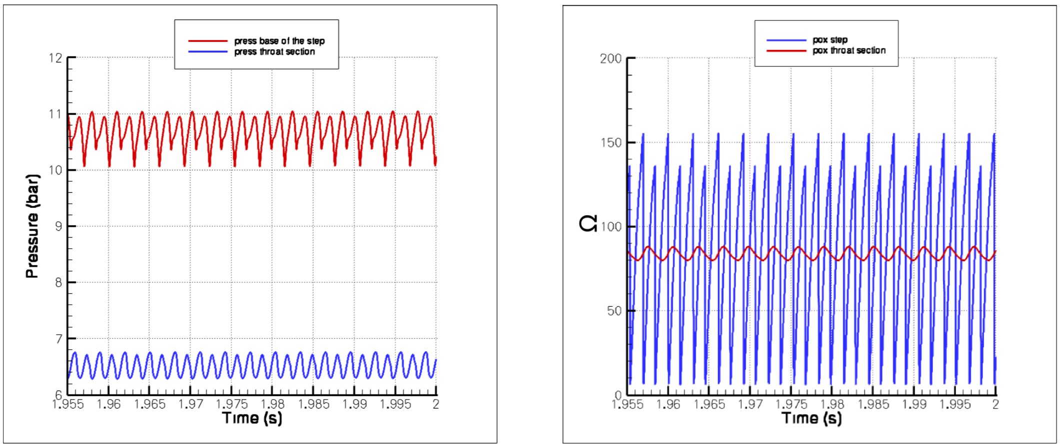

(a) Pressure (b) Vorticity (Ω)

Figure 4.8: Pressure and vorticity (Ω) time evolution.

components for the pressure spectrum both at the base of the step and at the nozzle throat. A comparison between the two sections shows a damping effect, higher for the vortex shedding frequencies than for the acoustic ones; while the pressure fluctuation at the base of the step is characterized by an amplitude of $\sim$ 1 bar, it decreases to $\sim$ 0.5 bar at the nozzle (this value is almost constant).

The same frequencies seen in the pressure spectra are visible in the vorticity (Ω) spectrum. Also for the vorticity at the detachment point the first acoustic mode is the most important contribution also for the vorticity at the detachment point, while it is almost completely damped at the nozzle throat section. In this section, the fundamental frequency is the vortex shedding peak at $\sim$ 330 Hz. This behavior underlines an energy passage, with the vortex convection towards the nozzle, from the acoustics to the vortical field.

The analyzed configuration does not exhibit a resonant condition. Indeed, the spectra in fig. 4.9 present both the frequencies related to the acoustics and to the vortex shedding (a resonant case is characterized by a single frequency peak).

The obtained phenomenological description and results are in agreement with Jou and Menon analysis. Some quantitative difference can be related to the assumption that has been used in order to complete the data set (e.g.: the inlet pressure value).

4.2.6 COMMENTS

AGAR simulation results show a correct description of the main phenomena characterizing the acoustic resonance; the obtained results are in good agreement with Jou and Menon's study. The assumptions used to perform this simulation, and related to the lack of some data, determine some quantitative difference (e.g.: the relative amplitude of the frequency peaks).

The results analysis shows a non resonant condition for the system in this configuration. Indeed, the spectra in fig. 4.9 exhibit both the frequencies related to the acoustics and to the vortex shedding.

4.3 INLET MACH NUMBER EFFECT

In addition to the test case characterized by an inlet Mach number of $M_{in} = 0.32$, Jou and Menon proposed another configuration with $M_{in} = 0.44$. AGAR simulation of this test case is here presented, and it is compared to their results.

Further, in order to develop a complete description of the Mach number effect, AGAR simulations are also developed for an inlet Mach number of: 0.25, 0.38, 0.55 and 0.7. This analysis allows to describe the shift towards, and from, the resonant condition. It also makes it possible to study the coupling mechanism between the acoustics and vortex

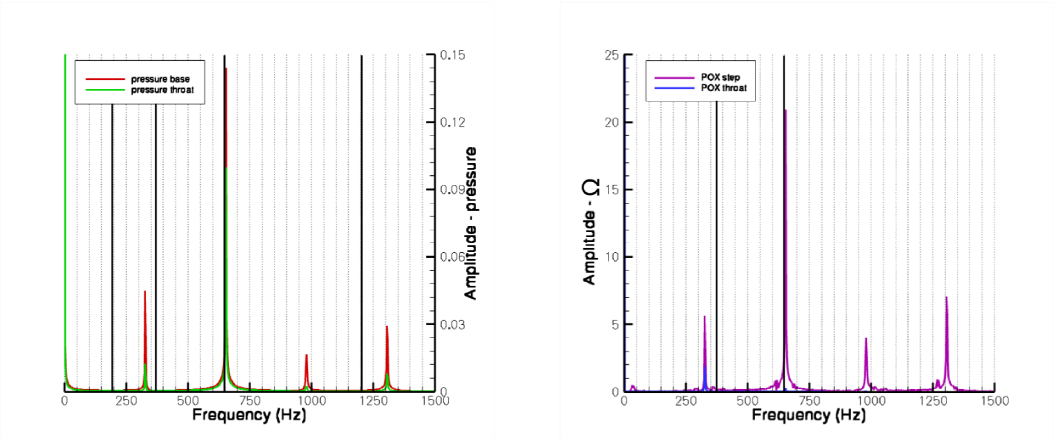

(a) Pressure spectrum. (b) Vorticity (Ω) spectrum.

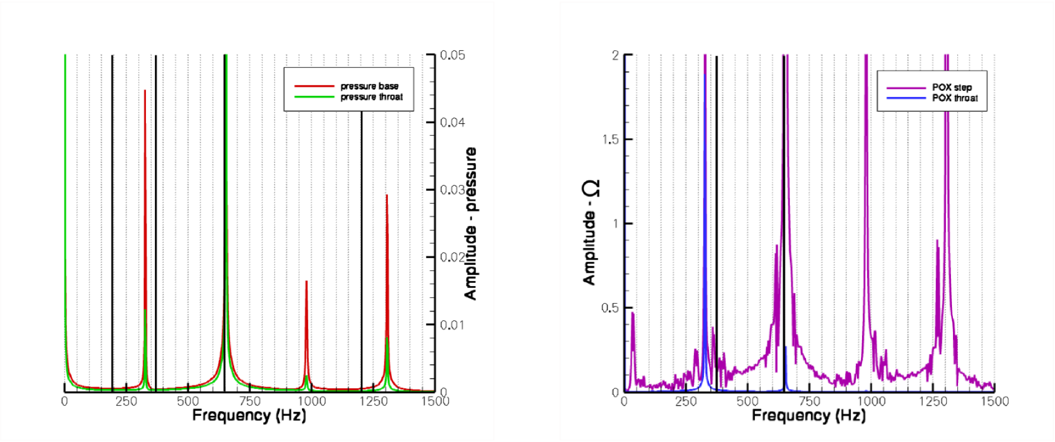

(c) Pressure spectrum zoom. (d) Vorticity (Ω) spectrum zoom.

Figure 4.9: Pressure and vorticity (Ω) spectrum.

shedding. Moreover, it makes it possible to distinguish between acoustic and vortex shedding nature of the peaks, that are respectively almost fixed and moving.

The inlet total pressure and temperature are maintained at the same values considered already considered for $M_{in} = 0.32$.

The change of the inlet Mach number is obtained with a variation of the nozzle throat area. The assumed geometrical configuration is unchanged until the nozzle nose; obviously the variation of the throat area involves variations of the nozzle geometry (port area and the relative dA/dx). The energy and momentum source terms, eq. 3.56, are proportional to dA/dx; different oscillation amplitudes are then expected for each test case. The geometrical configuration of each considered test case can be seen in fig. 4.10.

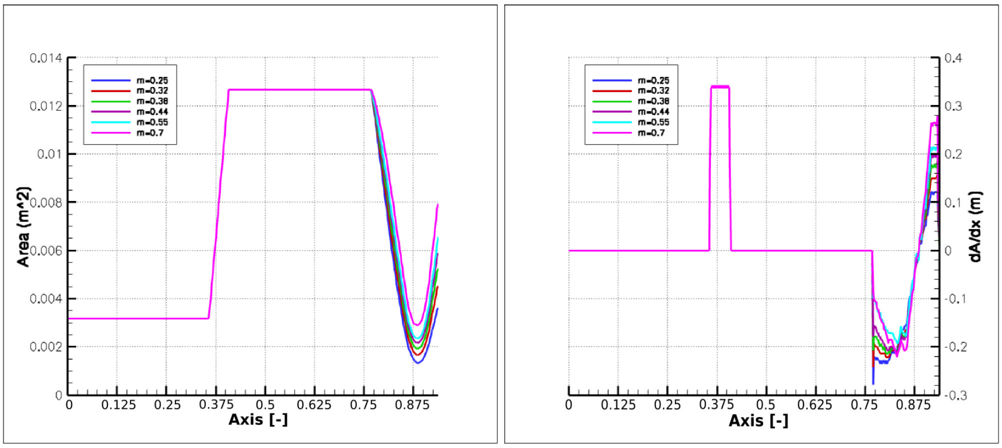

(a) Port area

(b) $\frac{dA}{dx}$

Figure 4.10: Test cases geometrical configuration.

4.3.1 VORTEX DETACHMENT CRITERION

The time evolution, of both pressure and velocity, at vortex detachment point is far from a sinusoidal behavior. As shown in fig. 4.11, the imposed detachment conditions do not necessarily identify a pressure descending node. The vortex separation occurs for a pressure local minimum and for a velocity local maximum; a separation occurring at velocity local maximum is in agreement with literature observations. Also in fig. 4.11, the resonant (M_{in}=0.38, 0.44, 0.55) and non resonant (M_{in}=0.25, 0.7) conditions can be distinguished, because of the complex frequency content of the non resonant cases.

The analysis of the detached vortex dimension simplifies the distinction between resonant and non resonant conditions. In fig. 4.12, the M_{in}=0.38, 0.44, 0.55 cases are described by the separation of vortices characterized by the same dimension, while the

M_{in}=0.25, 0.7 cases present different dimensions (related to the existence of more than a shedding frequency).

4.3.2 VORTICITY (Ω) DISTRIBUTION

The analysis of the vorticity (Ω) distribution, fig. 4.13, completes the description of the obtained solutions.

For M_{in}=0.25, 0.7, the vorticity (Ω) non regular envelopment is related to the detachment of vortices of variable intensity, and this corresponds to a non resonant condition. The other cases present a vorticity (Ω) distribution typical of resonant conditions.

The number of relative maxima corresponds to the number of detached vortices. This number is reduced by the increase of the M_{in} number. The resonance frequency has a slight shift from one case to another; the increase of the flow velocity, that corresponds to an increase of the vortex convection velocity, requires a lower number of vortices in order to obtain the same frequency value.

From the six vortices of the M_{in}=0.25 and M_{in}=0.38 cases, this number decrease to five for M_{in}=0.44 and M_{in}=0.7 and to four for M_{in}=0.55.

4.3.3 PRESSURE, VELOCITY AND SPEED OF SOUND DISTRIBUTIONS

Each test case that has been analyzed is characterized by a different geometrical configuration, then by different flow conditions. The pressure, velocity and speed of sound distributions are respectively shown in fig. 4.14, 4.15, 4.16.

The analysis of the pressure and velocity node position is aided by their time derivative distributions, presented in fig. 4.17 and 4.18.

With the increase of the M_{in}, the pressure distribution shows a moving back of the node position. The resonant cases exhibit mean pressure values higher than the non resonant ones. The same observations can be done for the speed of sound distribution.

The mean value of the flow velocity increases with the M_{in}; in correspondence of the pressure node, the velocity field presents an antinode that moves back for higher M_{in}.

While the node/antinode identification is quite simple for resonant coupling, it is quite difficult for non resonant cases.

4.3.4 PRESSURE AND VORTICITY (Ω) FLUCTUATIONS

The frequency content of both the pressure and the vorticity (Ω) fluctuation is in fig. 4.19, 4.20.

The main frequency peaks represent the first (~ 590-660 Hz) and the second (~ 1180-1330 Hz) acoustic mode. These components can be seen both at the base of the step

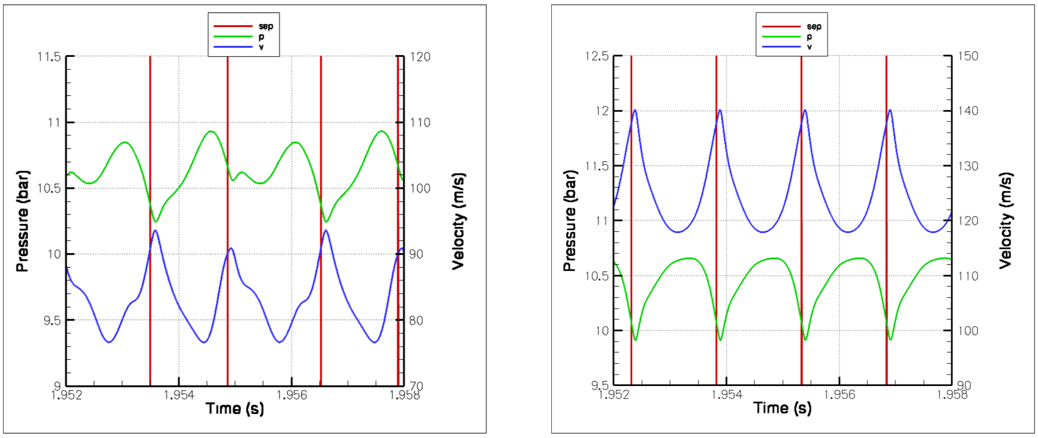

(a) M_{in}=0.25 (b) M_{in}=0.38

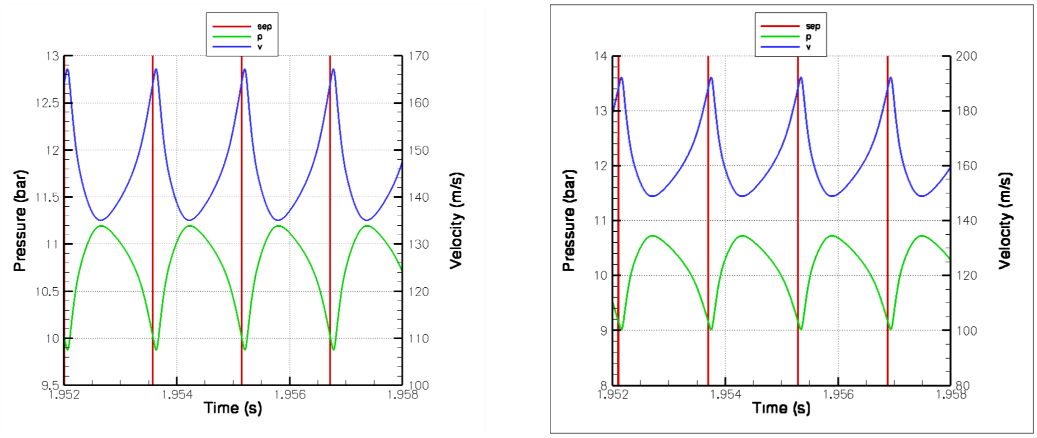

(c) M_{in}=0.44 (d) M_{in}=0.55

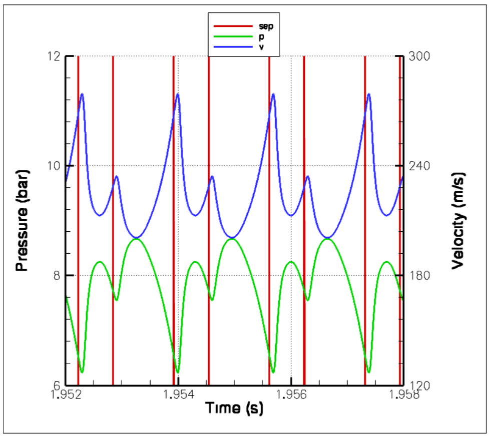

(e) M_{in}=0.7

Figure 4.11: Vortex detachment condition.

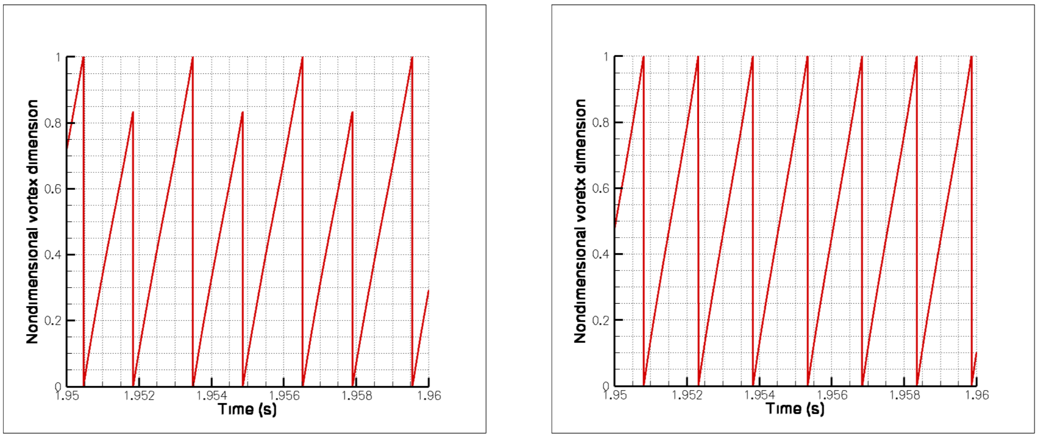

(a) M_{in}=0.25 (b) M_{in}=0.38

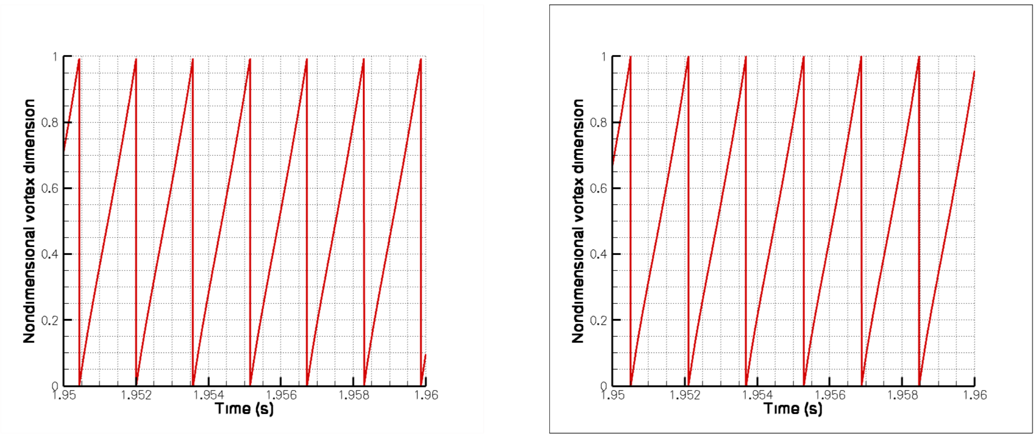

(c) M_{in}=0.44 (d) M_{in}=0.55

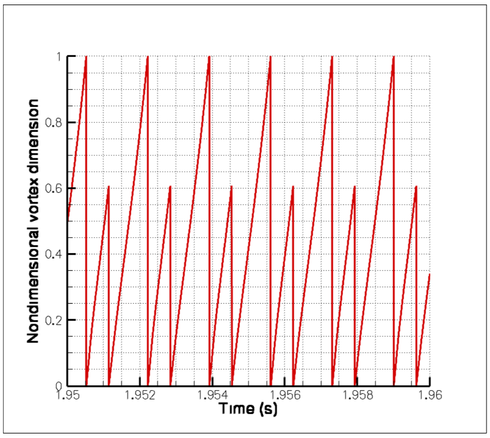

(e) M_{in}=0.7

Figure 4.12: Detached vortices dimension.

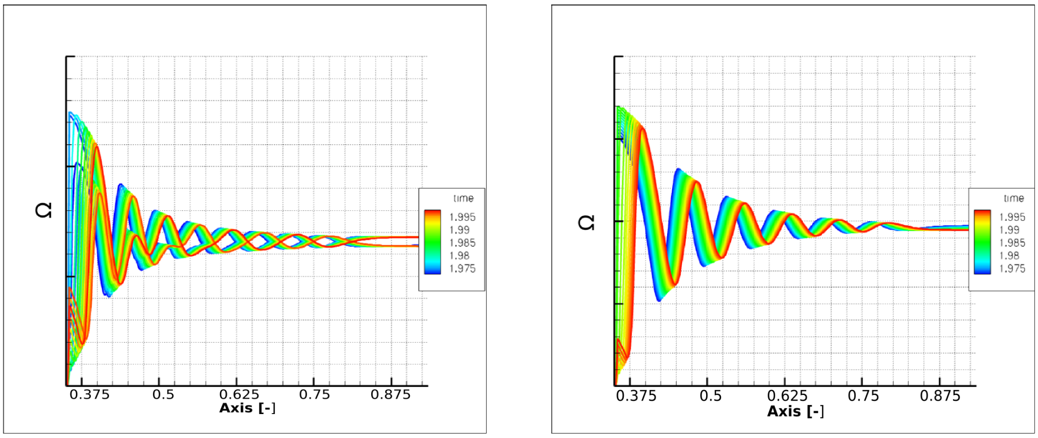

(a) M_{in}=0.25 (b) M_{in}=0.38

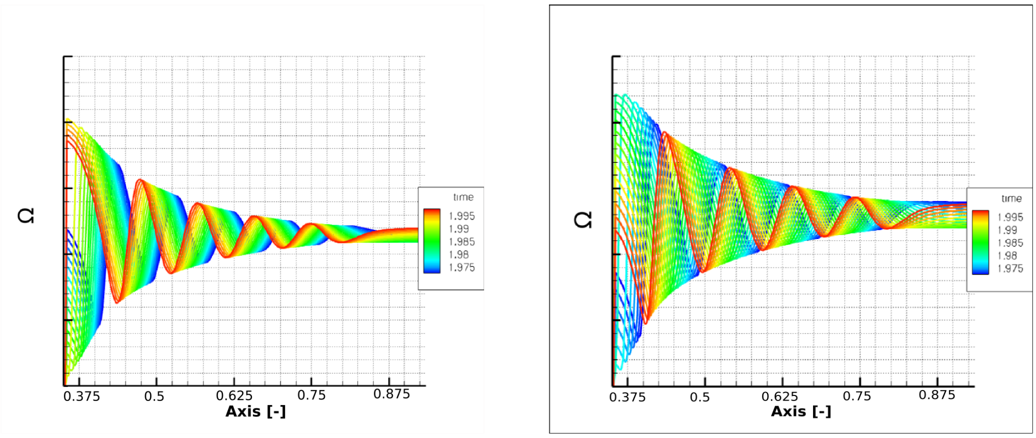

(c) M_{in}=0.44 (d) M_{in}=0.55

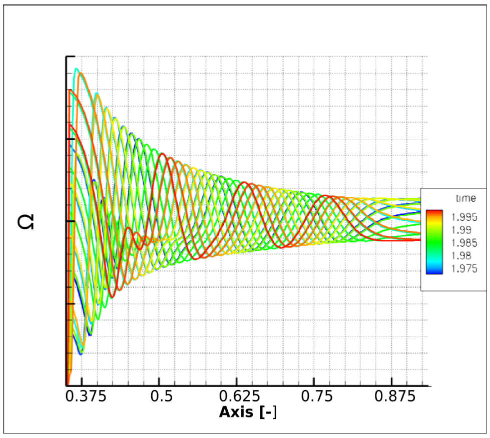

(e) M_{in}=0.7

Figure 4.13: Ω distribution.

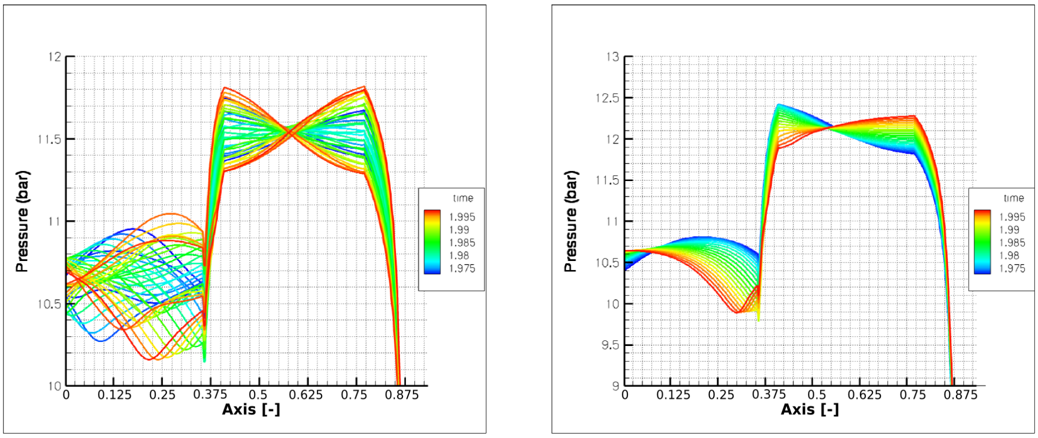

(a) M_{in}=0.25 (b) M_{in}=0.38

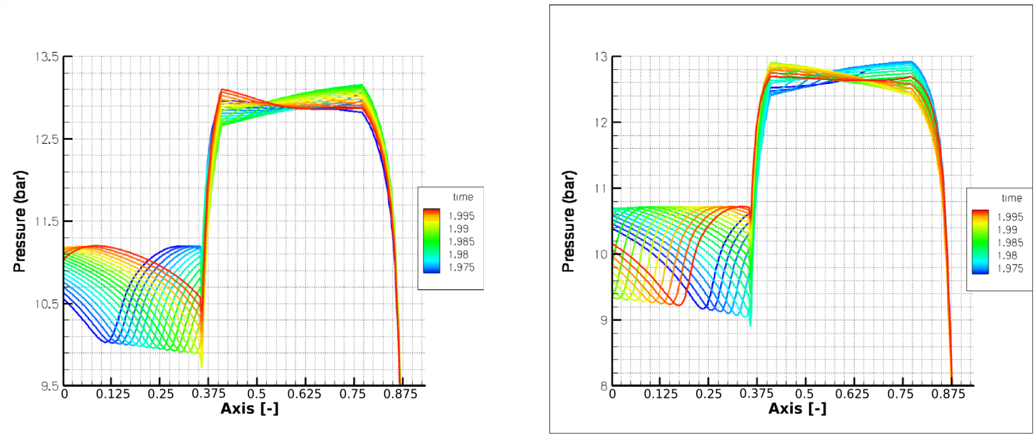

(c) M_{in}=0.44 (d) M_{in}=0.55

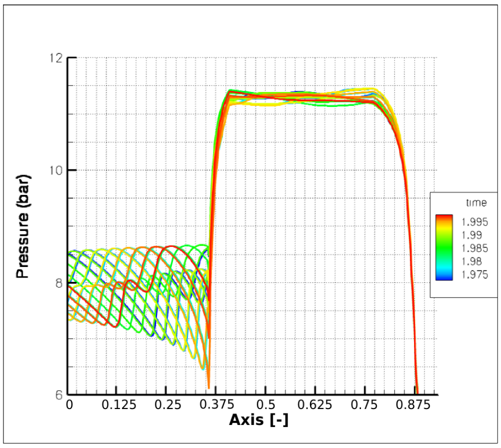

(e) M_{in}=0.7

Figure 4.14: Pressure combustion chamber distribution.

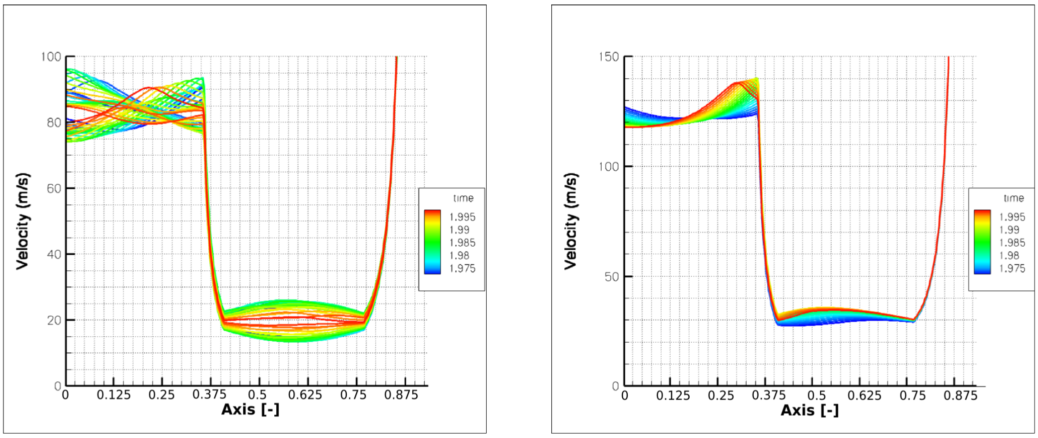

(a) M_{in}=0.25

(b) M_{in}=0.38

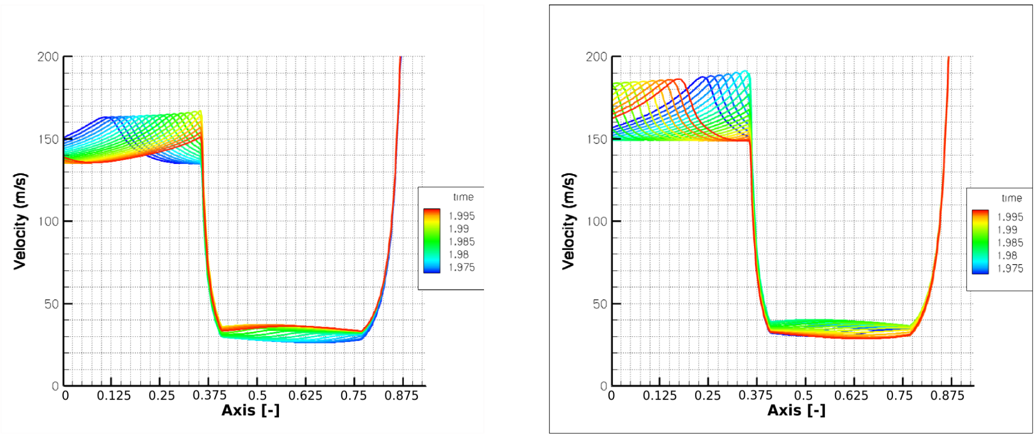

(c) M_{in}=0.44

(d) M_{in}=0.55

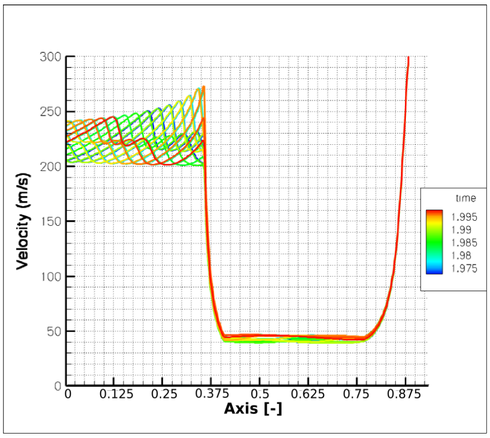

(e) M_{in}=0.7

Figure 4.15: Velocity combustion chamber distribution.

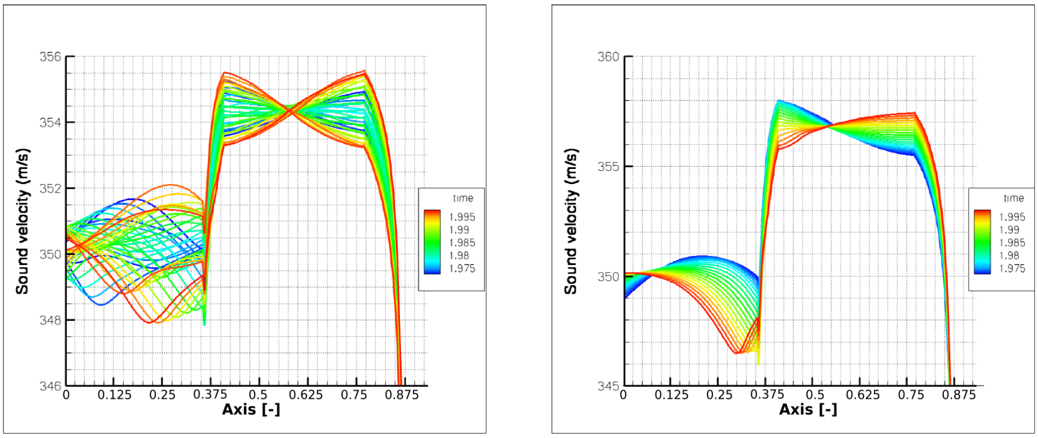

(a) M_{in}=0.25 (b) M_{in}=0.38

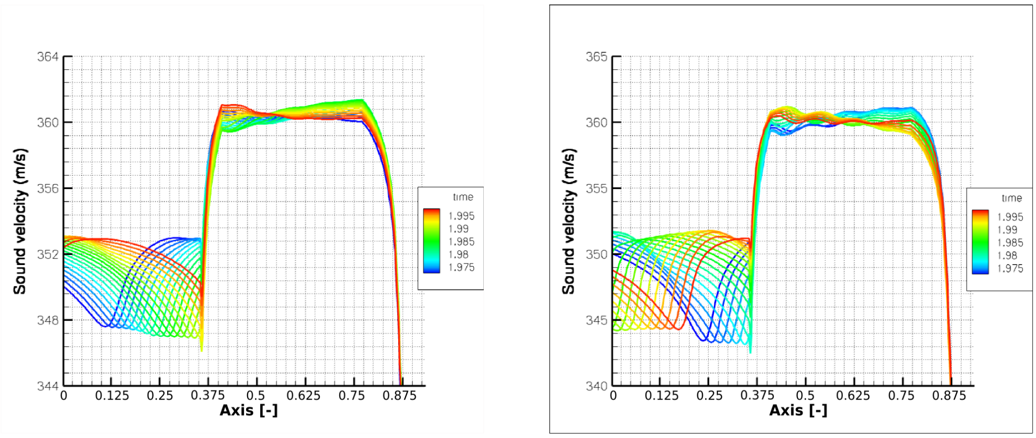

(c) M_{in}=0.44 (d) M_{in}=0.55

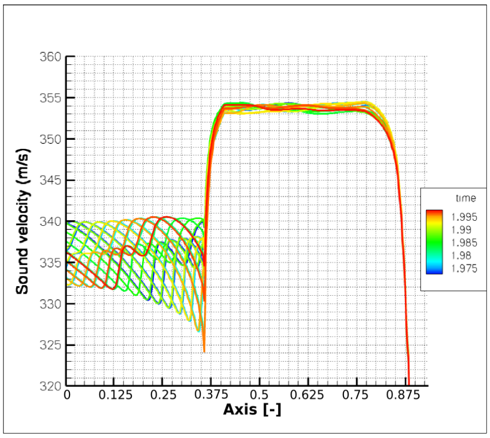

(e) M_{in}=0.7

Figure 4.16: Speed of sound combustion chamber distribution.

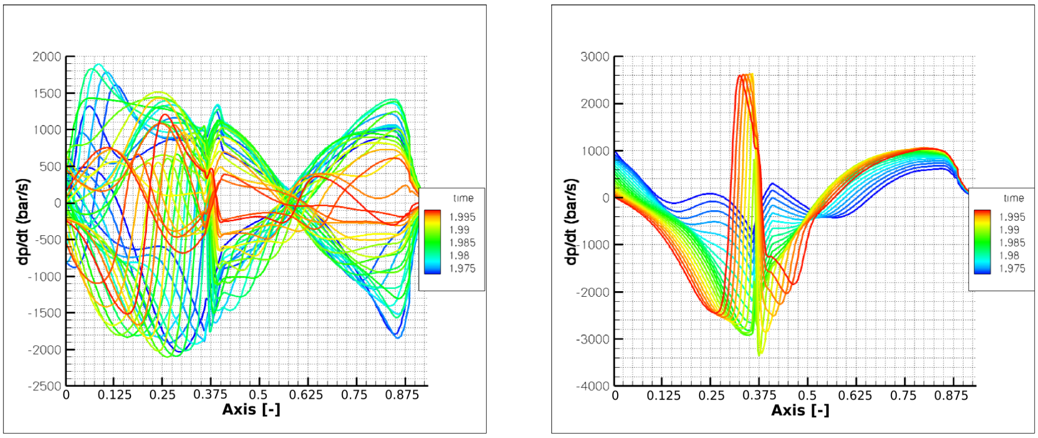

(a) M_{in}=0.25 (b) M_{in}=0.38

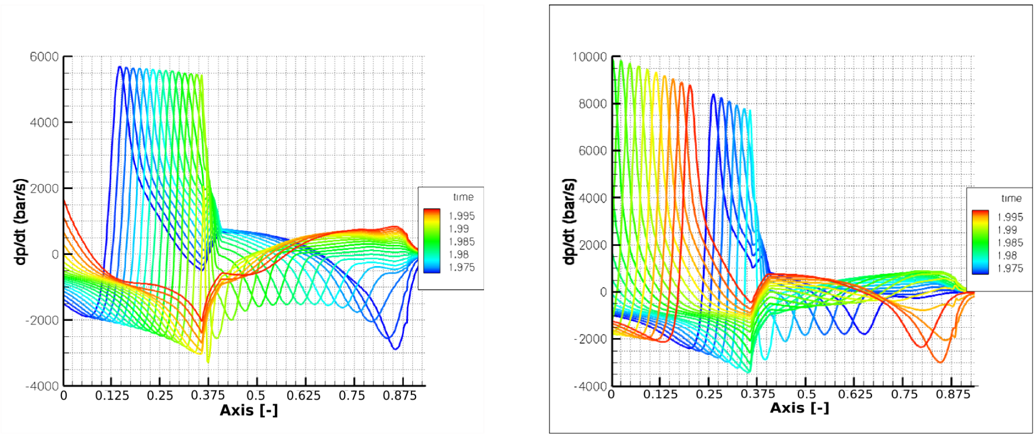

(c) M_{in}=0.44 (d) M_{in}=0.55

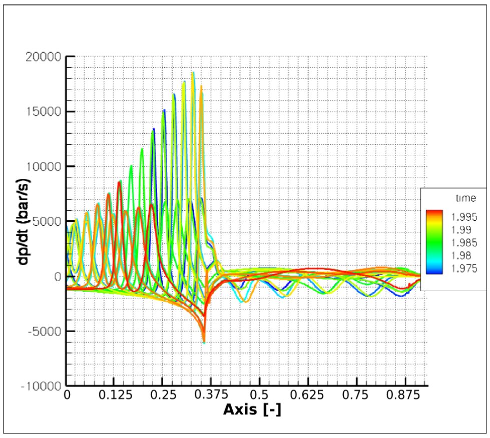

(e) M_{in}=0.7

Figure 4.17: Pressure time derivative combustion chamber distribution.

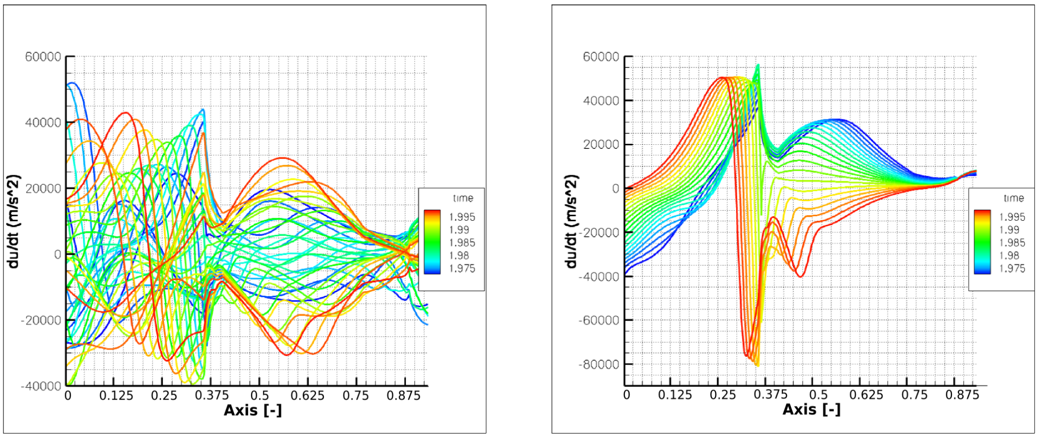

(a) M_{in}=0.25 (b) M_{in}=0.38

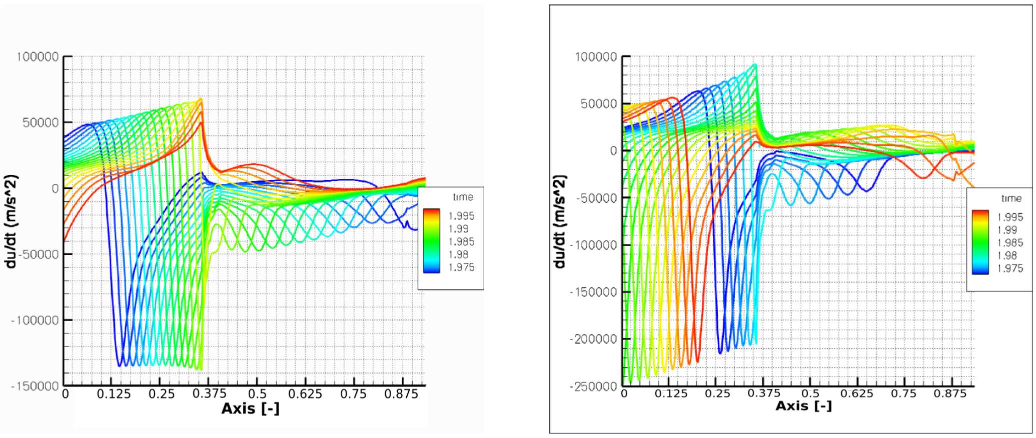

(c) M_{in}=0.44 (d) M_{in}=0.55

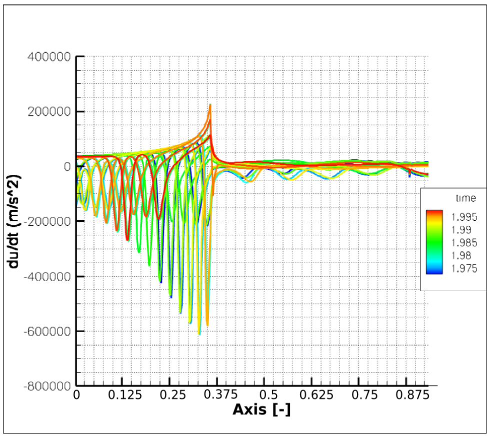

(e) M_{in}=0.7

Figure 4.18: Velocity time derivative combustion chamber distribution.

and at the throat section, but their relative importance is not the same. The dominant contribution is represented by the first acoustic mode both at the step and at the nozzle for M_{in}=0.25, 0.38, 0.44, 0.55. Also for M_{in}=0.55 a dominant first acoustic mode is shown, but at the nozzle the second mode increases its relative importance. This effect is amplified for M_{in}=0.7, where an energy passage from the first to the second mode, makes the last one the nozzle dominant contribution.

The test cases M_{in}=0.32, 0.25 show different frequency components related to the acoustics and to the vortex shedding. The vortex shedding is characterized by two peaks at ~ 330 and ~ 980 Hz. The existence of this peaks shows that the system is not in resonant condition.

The simulations for M_{in}=0.38, 0.44, 0.55 exhibit the resonant coupling condition, so that the only visible peaks are that related to the resonant behavior.

The M_{in}=0.7 case appears to be described by a typical resonance condition, but a detailed analysis of the vorticity (Ω) field frequency content shows an increasing importance of the frequencies at ~ 130 and ~ 1050 Hz, because of the system shift from resonant configuration.

The resonant frequency decreases with the M_{in} increase, with a greater effect for the second than for the first acoustic mode.

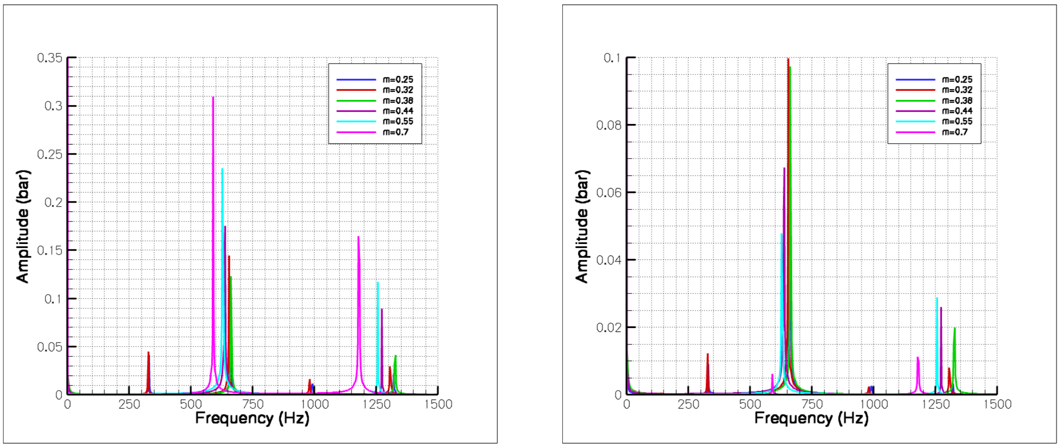

(a) Base of the step

(b) Nozzle throat section

Figure 4.19: Pressure spectrum.

4.3.5 COMMENTS

The analysis here performed shows that a M_{in} increase determines a system shift from a non-resonant condition (M_{in}=0.25, 0.32) to a resonant one (M_{in}=0.38, 0.44, 0.55), and then to a non-resonant again (M_{in}=0.7).

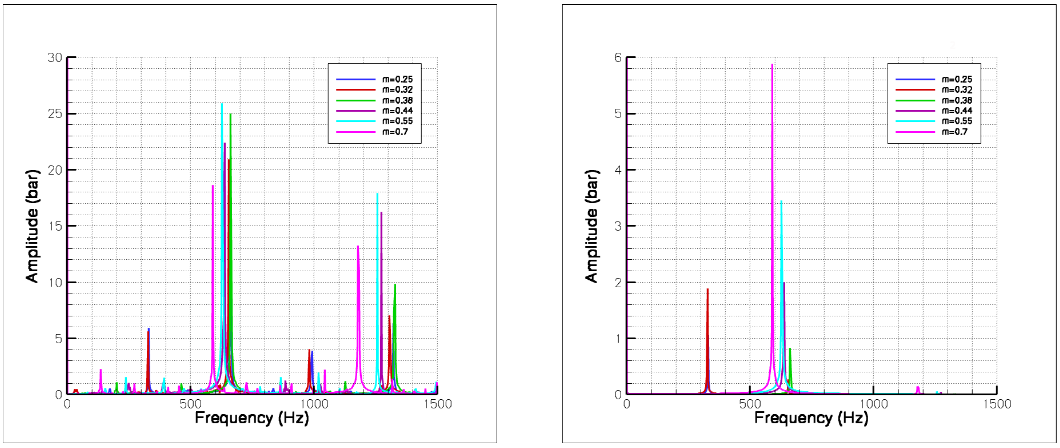

(a) Step (b) Nozzle throat section

Figure 4.20: Ω spectrum

The resonant frequency decreases with M_{in}, and each test case is characterized by different configurations in terms of flow conditions and number of vortices.

The fundamental acoustic frequency is represented by the first mode for M_{in}=0.25, 0.32, 0.38, 0.44; from M_{in}=0.55, with the vortex convection there is an energy passage from the first to the second mode, that becomes the dominant throat section contribution.

The pressure oscillation spectrum, at the base of the step, and the vorticity spectrum, at the nozzle inlet, for M_{in}=0.32 and M_{in}=0.4, are the results directly comparable with Jou and Menon's analysis. They showed that for M_{in}=0.44 the system is moving towards resonant condition, notwithstanding it is not fully reached. AGAR simulation, on the contrary, presents a resonance configuration already from $M_{in} = 0.38$. The origin of this difference is quite difficult to identify, because of the assumptions introduced in the test case simulation (e.g.: the nozzle geometry, the total pressure value).

4.4 CONCLUSIONS

Jou and Menon's test case simulation shows AGAR model capability to describe the main phenomena characterizing the aeroacoustic coupling. Moreover, the model describes the system adjustment to resonant condition and then its return to non resonant one.

The results obtained for M_{in}=0.32 are in agreement with Jou and Menon's analysis, as for the qualitative than for the quantitative description. For M_{in}=0.44, AGAR correctly describes the systems moving towards resonant configuration.

5

PRESSURE OSCILLATIONS IN P80 SRM

The simulation of the aeroacoustic coupling of a solid rocket motor is here proposed. The P80 SRM, first stage of the European Vega launcher, is the solid rocket motor here considered. Four pressure oscillation phases characterize the motor operative life.

The P80 SRM represents a complete test case, because of the existence of all the phenomena that characterize the aeroacoustic phenomenon: grain regression due to the propellant combustion, radial mass addition, corner vortex shedding, ...

The results obtained by AGAR simulation are compared with the experimental static firing tests, realized during the motor development process. Moreover, a description of the obtained results is provided and AGAR capabilities are verified.

5.1 P80 SOLID ROCKET MOTOR

The P80 SRM is the first solid stage of the new European VEGA launcher. It also represents both a technology demonstrator and a new generation of Ariane-5 solid boosters.

P80 SRM development is managed by ESA, and involves staffs from ESA, ASI (Italian Space Agency) and CNES (French space agency), that covers a primary role. The responsible for the motor development program is the French-Italian joint venture Europropulsion (Avio S.p.a. and Snecma Propulsion Solide), delegated by Avio S.p.a. that formally represents the P80 SRM prime contractor. The P80 SRM also represents a technology demonstrator and a new generation of Ariane-5 solid boosters. The propellant casting is realized in the Guyana Propellant Plant in Kourou, the same used for Ariane 5's solid boosters.

A simple scheme of the P80 SRM configuration and some notes, main characteristics and performance, can be seen in fig. 5.1. The combustion chamber has a length of about 10.5 m and a diameter of 3 m. The propellant grain, HTPB propellant, is a single finocyl grain, cylindrical in the head region and with star grain in the aft end, and it has a weight of 88 tons. The motor achieves a Maximum Expected Operating Pressure (MEOP) of 95 bar and it delivers a mean thrust of 3040 kN, with a burn time of 107 s and a specific impulse of 280 s.

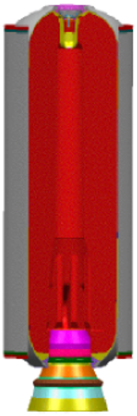

Height: 10.5 m
Diameter: 3 m
Propellant mass: 90 ton
Thrust in vacuum: 3040 kN
Maximum pressure: 95 bar
Nozzle expansion ratio: 16
Vacuum specific impulse: 280 s
Combustion time: 107 s

Figure 5.1: P80 fundamental characteristics and performances.

During the motor development process, two static firing tests have been performed. The demonstration test, indicated as P80 DM, was realized employing helium as pressurizing gas, in order to reduce and to control the pressure oscillations that characterize the ignition transient. On the contrary, for the qualification test, indicated as P80 QM, nitrogen has been used as pressurizing gas. Except for this difference, both P80 DM and P80 QM present the same motor configuration.

Despite their similarities, the two firing tests exhibit different experimental results. The P80 QM shows three pressure oscillation phases, called blows, in the first 50 s of the motor combustion time. For the P80 DM this number increases to four, as shown in fig. 5.2.

Because of the quality of the experimental data, the P80 DM has been taken into account as test case for AGAR simulation.

5.2 P80 DM STATIC FIRING TEST EXPERIMENTAL DATA

The static firing tests provide two head pressure signals, obtained by a static and a dynamic pressure sensor.

In fig. 5.3, the P80 DM head pressure data, for both the static and the dynamic sensor, are shown. The dynamic sensor exhibits four pressure oscillation phases in the first 50 s

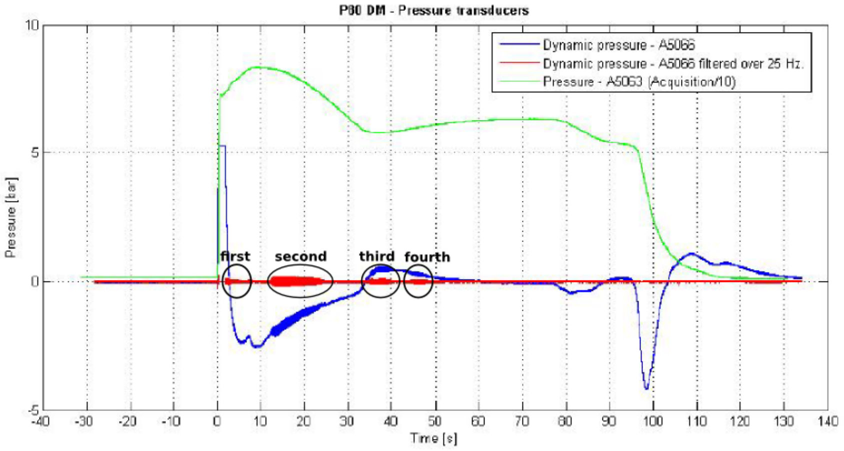

Figure 5.2: P80 DM pressure oscillation.

of the combustion time. Their timing, amplitude and frequency are enumerated in tab. 5.1.

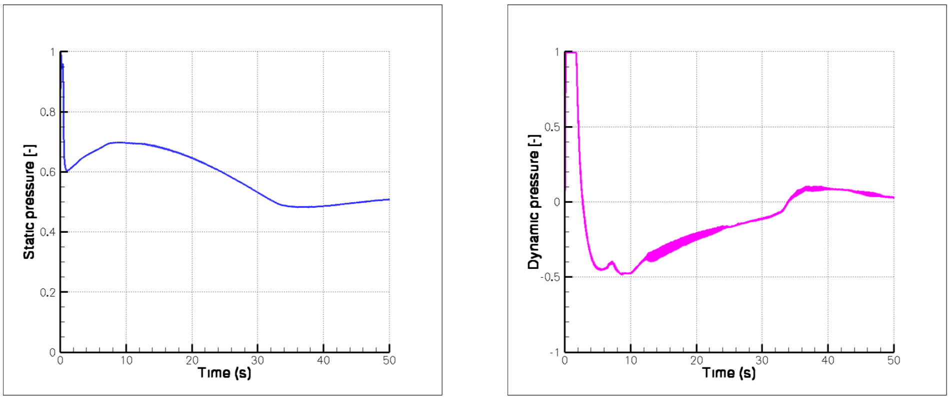

(a) P80 DM static sensor

(b) P80 DM dynamic sensor

Figure 5.3: P80 DM experimental data (10 KHz) - non dimensional head pressure.

5.2.1 ANALYSIS OF THE EXPERIMENTAL HEAD PRESSURE OSCILLATIONS

The pressure oscillation amplitude represents only a few percent of the mean pressure value. A better visualization can be obtained by separating the fluctuating component from the pressure signal. This decomposition is here achieved with a sliding average filter,

blow	Time (s)	Frequency (Hz)	Amplitude (bar)
I	1.6 - 5.9	50	0.217
II	12.6 - 24.4	51	0.209
III	34.5 - 39.5	54	0.112
IV	44 - 48.5	55	0.061

Table 5.1: P80 experimental pressure oscillation blows (10 KHz).

with a smoothing up to 12.5 Hz[1]. The filtered signal and the fluctuating component are shown in fig. 5.4. The dynamic sensor presents a lower noise level than the static sensor, and this makes the four oscillating phases more evident.

The spectra of the oscillating component, of both dynamic and static sensor, is shown in fig. 5.5. Except for the peaks amplitude, both sensors present a similar frequency content. The first and the second acoustic mode can be respectively seen at ~ 50-55 Hz and ~ 110-115 Hz. Other frequency components can be seen at ~ 40, 61, 103 Hz. The static sensor fluctuation exhibits two peaks at ~ 77, 87 Hz, not visible in the dynamic sensor signal.

The first acoustic mode is around ~ 50-55 Hz, and this value corresponds to the resonant frequency. An easier visualization of the resonant coupling oscillation can be obtained by filtering the fluctuating component between ~ 45-65 Hz; the result is visible in fig. 5.6. The two experimental data exhibit analogous results, although an higher noise level of the dynamic sensor. While the first and the second blows show a frequency content in the range ~ 45-65 Hz, the third blow has a major component at ~ 45-55 Hz while the fourth is at ~ 55-65 Hz (the frequency component of ~ 55-65 Hz for the third blow and of ~ 45-55 Hz for the fourth are negligible).

5.2.2 HHT ANALYSIS OF THE EXPERIMENTAL HEAD PRESSURE OSCILLATIONS

The head pressure time evolution of a solid rocket motor is a non periodic, non linear and non stationary datum. In this case the Fourier Transform is not the proper tool for the analysis of the signal frequency content.

The Hilbert-Huang transform (HHT), described in the appendix B, represents the suitable tool that is used for the analysis of the pressure oscillation. The HHT analysis provides a signal description in term of time evolution of both amplitude and frequency. In correspondence of a pressure oscillation blow, an higher or increasing amplitude of the fluctuation is expected, with a frequency close to the acoustic one.

---

[1] The signal has a sampling of 10 kHz and an average over 200 samples is used.

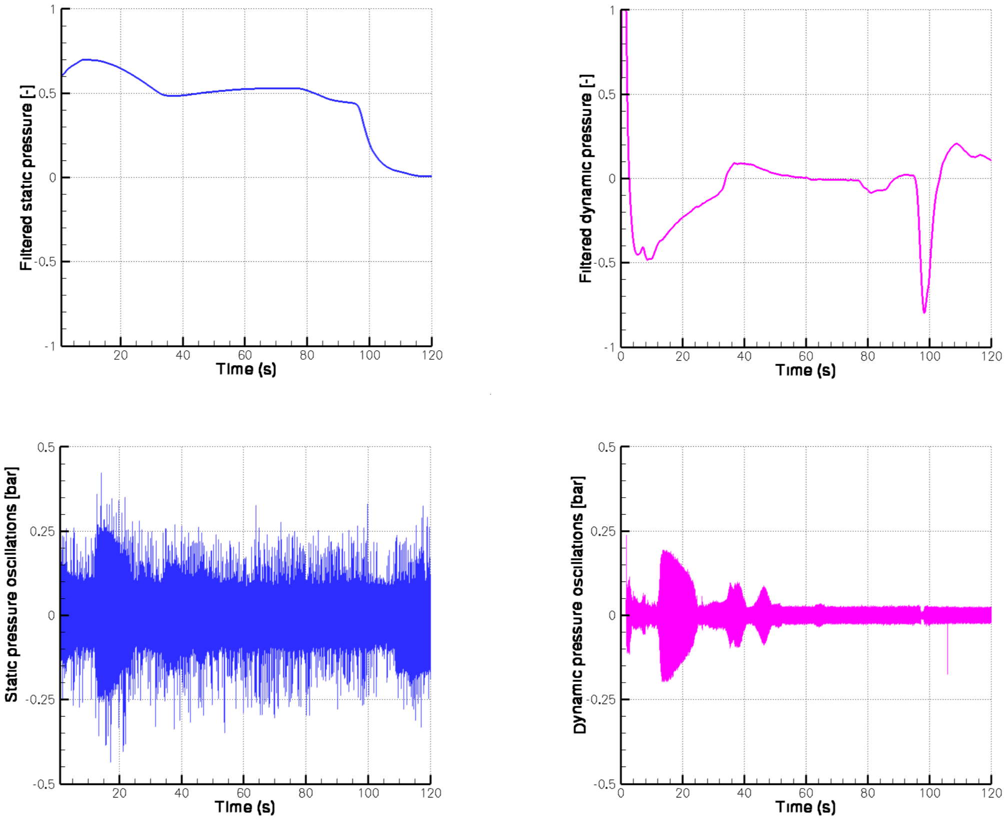

(a) P80 DM static sensor (b) P80 DM dynamic sensor

Figure 5.4: P80 DM experimental data - filtered and oscillating component of the non dimensional head pressure.

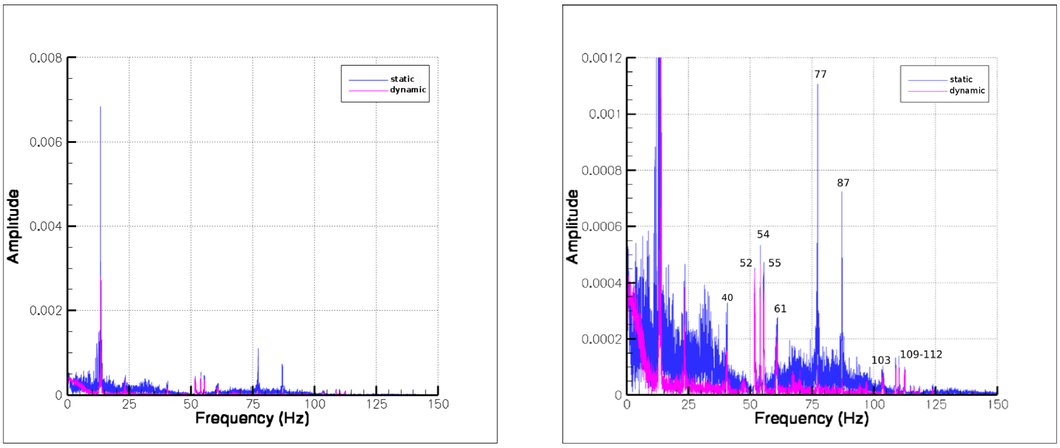

(a) Amplitude [0-0.008]

(b) Amplitude [0-0.0012]

Figure 5.5: P80 DM experimental data - spectra of the oscillating component.

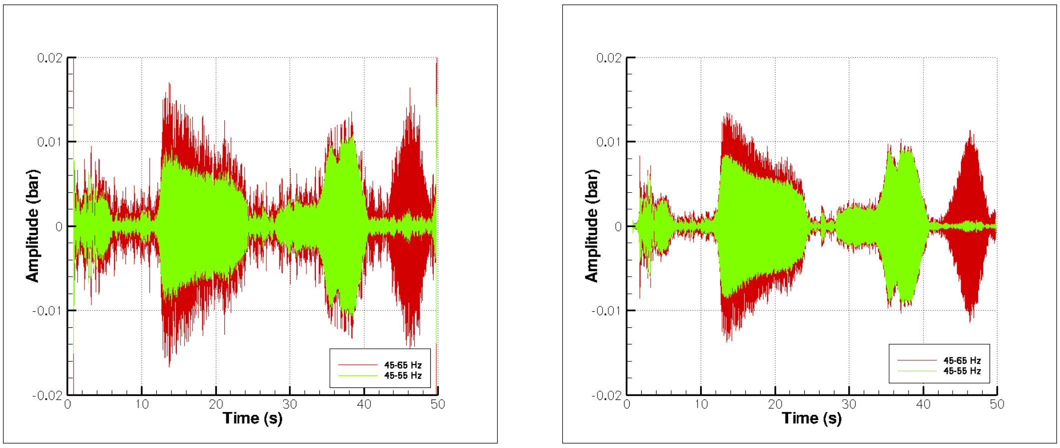

(a) P80 DM static sensor

(b) P80 DM dynamic sensor

Figure 5.6: P80 DM experimental data - windowing of the pressure oscillations 45-65 Hz.

The HHT is then applied to the head pressure fluctuating component of fig. 5.4. The results, split into three time interval 0-11 s, 10-30 s and 30-50 s, are shown in fig. 5.7, 5.8, 5.9.

The HHT shows a frequency of the first acoustic mode slightly increasing, from 50 Hz to 55 Hz, with the combustion time.

For the first blow, its identification is more ambiguous than the others; it appears visible between 2-3.5 s and it is characterized by a resonance frequency of almost 50 Hz (second IMF, green line), as in fig. 5.7. The second blow is clearly visible between 12-24 s and it has a frequency, slightly increasing with time, around 50 Hz, as shown by the first IMF high amplitude (red line) in fig. 5.8. The third and fourth blow are between 35-39.5 and 45.5-47.5 s, and their frequency is increasing towards 55 Hz, first IMF (red line) of fig. 5.9.

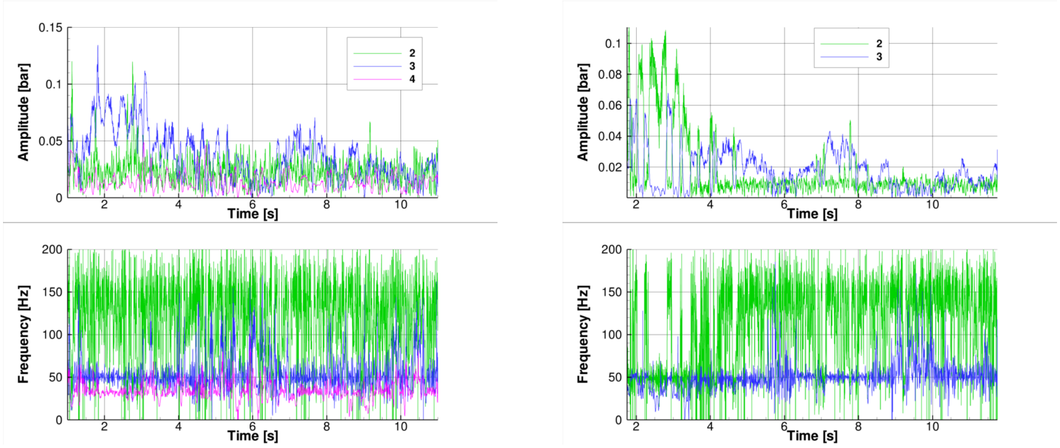

(a) P80 DM static sensor

(b) P80 DM dynamic sensor

Figure 5.7: P80 DM experimental data - pressure oscillations HHT analysis (0-11 s).

5.3 Rossiter's model analysis of P80 DM SRM

Rossiter's model, described in par. 1.6, is here applied to the analysis of the P80 DM. This model allows the determination, for a resonance condition, of the number of vortices in the combustion chamber. This analysis has to be repeated for each oscillating phase exhibited by the motor. Indeed, each blow is characterized by different flow conditions and stand off distance l_i[2].

---

[2] The flow conditions are related to different ´ convection velocity, while l_i changes because of the step position regression.

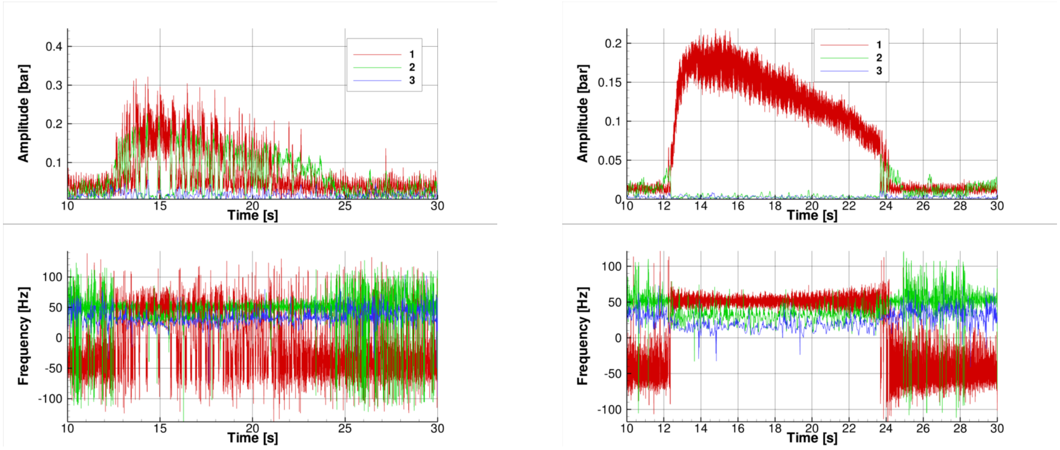

(a) P80 DM static sensor (b) P80 DM dynamic sensor

Figure 5.8: P80 DM experimental data - pressure oscillations HHT analysis (10-30 s).

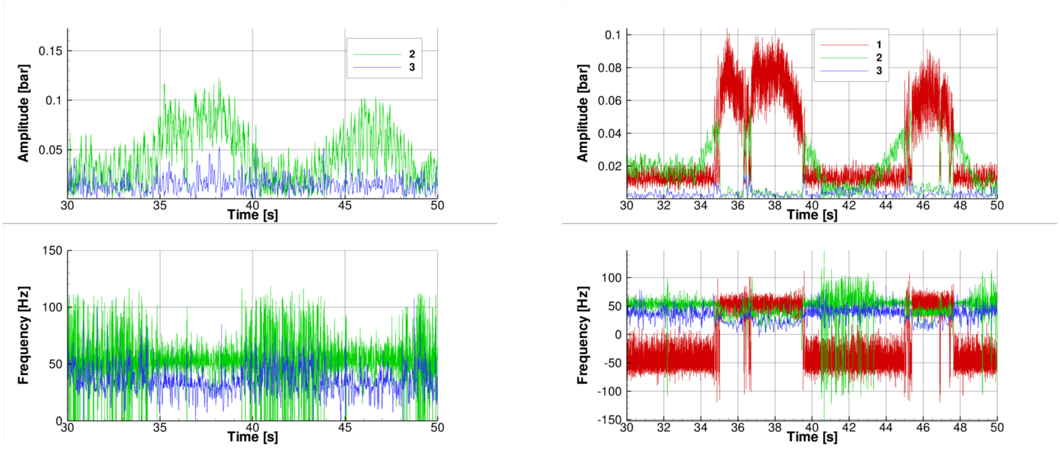

(a) P80 DM static sensor (b) P80 DM dynamic sensor

Figure 5.9: P80 DM experimental data - pressure oscillations HHT analysis (30-50 s).

The acoustic resonance frequency of P80 SRM is already known from the experimental data, and its value is ∼ 50 Hz. From literature, the parameter that describes the vortex convection velocity is assumed $k_R = 0.58$.

The obtained results are listed in tab. 5.2. With the increase of the combustion time, the number of detached vortices, characterizing the resonance condition, passes from 7 to 11. These too high numbers clearly show that Rossiter's model does not identify any possible resonance solution for this motor.

	I	II	III s	IV
l_i	2.6	2.85	2.9	2.9
k	0.58	0.58	0.58	0.58
u	40	30	30	28
m	7	10	10	11

Table 5.2: P80 analysis using Rossiter's model.

Also with the assumption of a $k_R = 1$, the model shows a physically reasonable resonance configuration only for the first blow. The model is unable to obtain reasonable results for the analyzed case.

It has to be remembered that Rossiter's model does not take into account both two phase flow and combustion instabilities.

5.4 AGAR NUMERICAL SIMULATION

The four pressure oscillation phases of the P80 SRM are located in the first 50 s of the combustion time; also for AGAR simulation a time interval of 50 s is then considered.

The k_Γ value, required by the POX submodel, is determined by the comparison between the numerical oscillation amplitude and the experimental one.

The geometrical evolution of the combustion chamber, due to the grain regression, is evaluated in AGAR model by using the GREG model. The combustion chamber, considered from the head to the nozzle throat section, is discretized by a uniformly spaced grid of 400 cells. In fig. 5.10, the port area time evolution is shown in correspondence of each experimental blow.

The P80 SRM is characterized by a finocyl grain, with a cylindrical head region and a star in the aft region. The vortex detachment point is assumed located at the grain corner, the connection point between the two grain shape, 0.75 of the non dimensional axis. Due to the propellant surface regression, this point recedes form 0.758 to 0.718 of the non dimensional axis, as visible in fig. 5.10.

The aft region of the motor presents a submergence region of volume V_s; in AGAR simulation, this region is distributed in the last 8 cells of the combustion chamber (0.955-1

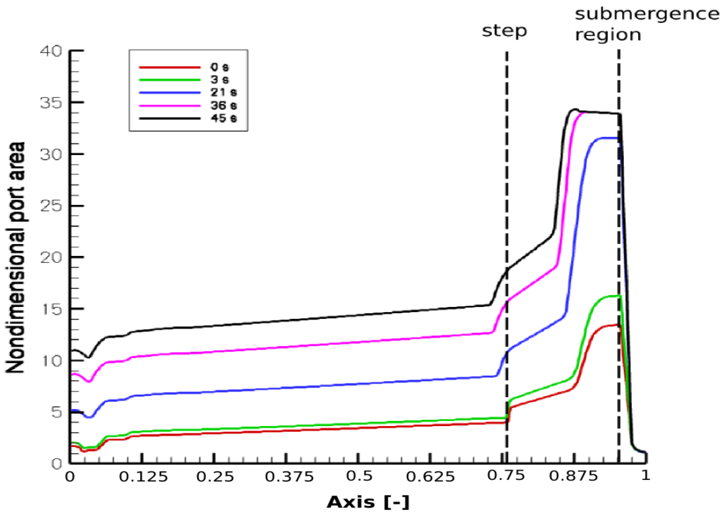

Figure 5.10: Evolution of P80 geometrical configuration.

of non dimensional axis). The volume ratio V_s/V_c, where V_c is the combustion chamber volume without submergence volume, increases with the grain combustion and passes from 11.7 % to 13.4 % of the total combustion chamber volume. The volume characteristics of the combustion chamber are summarized in tab. 5.3.

The submergence volume represents a considerable part of the total combustion chamber volume and this makes the Helmholtz resonator effect not negligible.

	initial configuration	final configuration
V_s/V_c	0.133	0.154
$V_s/(V_s+V_c)$	0.117	0.134
V_{fin}/V_c	0.469	0.390
V_s/V_{fin}	0.283	0.396

Table 5.3: Volume characteristics of P80 combustion chamber (submergence region volume V_s, combustion chamber volume without submergence volume V_c, finocyl region volume V_{fin}).

In the following paragraphs, the only resonant phases are described and analyzed. A description of the results characterizing a non resonant configuration is provided in appendix C.

5.4.1 HEAD PRESSURE

The head pressure time evolution provided by AGAR simulation can be seen in fig. 5.11. A zoom of the head pressure in each time interval of interest, corresponding to each experimental blow, is provided in fig. 5.12.

Pressure and frequency jumps can be noted at ~ 2, 38, 44 and 48.5 s, related to the resonance condition beginning or end. The characterization of each oscillation phase, amplitude and frequency content, is presented in the following paragraphs.

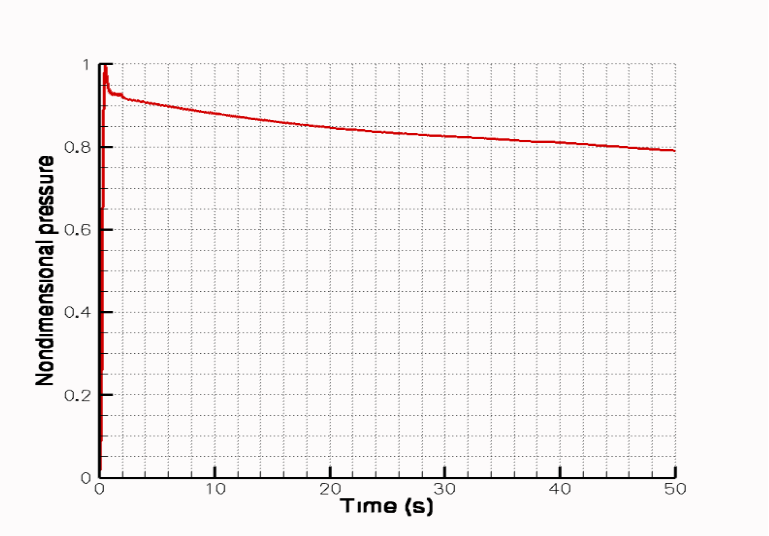

Figure 5.11: P80 DM AGAR simulation - head pressure.

5.4.2 ANALYSIS OF THE HEAD PRESSURE OSCILLATIONS

As for the experimental data, the pressure fluctuation component is separated from the pressure signal by using a sliding average filter, with a smoothing up to 12.5 Hz. The numerical pressure oscillation characteristics, frequency and amplitude, are summarized in tab. 5.4.

A comparison between the numerical fluctuating component and the experimental one, for the static sensor, can be seen in fig. 5.13. As the experimental data, also the numerical simulation exhibits four phases of resonant coupling, in spite of differences on timing and amplitudes. While the amplitude is correctly estimated for the first and the fourth blow, it is underestimated for the second and the third blow. It has to be noted that in fig. 5.13 the data still contain high frequency components, not related to the acoustic coupling (i.e: noise).

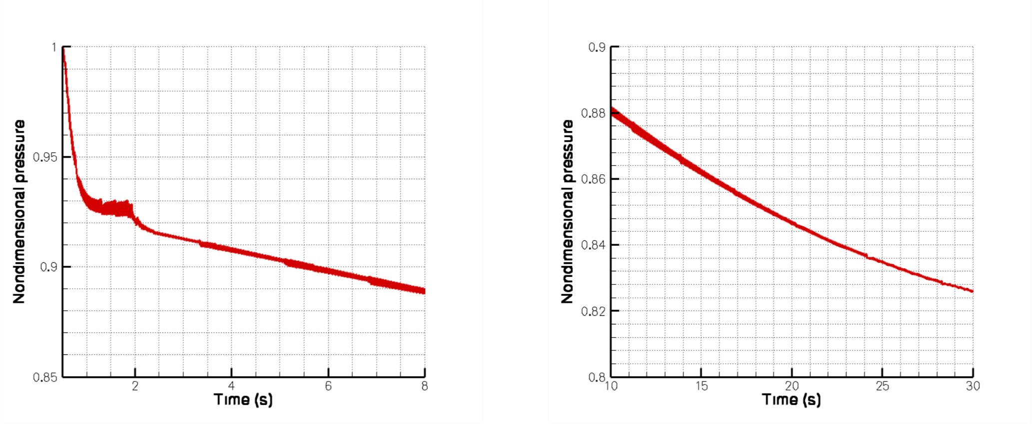

(a) First blow (b) Second blow

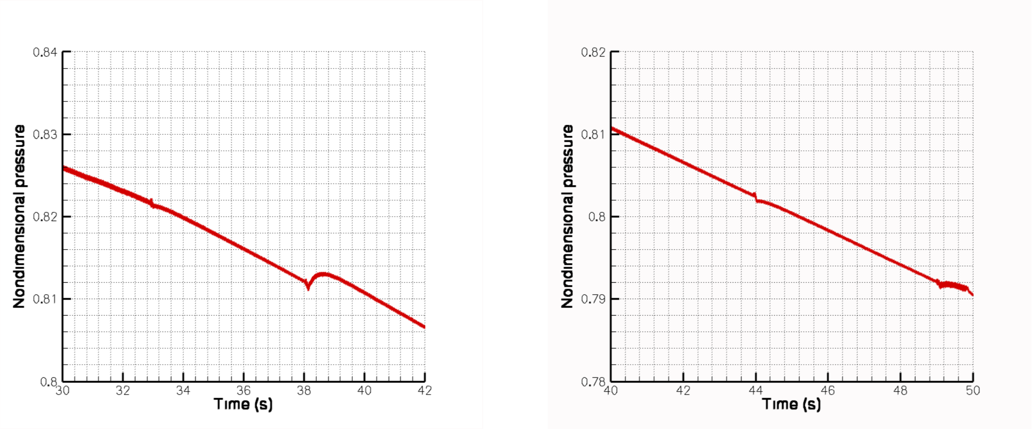

(c) Third blow (d) Fourth blow

Figure 5.12: P80 DM AGAR simulation - head pressure oscillation phases.

blow	time (s)	frequency (Hz)	Amplitude (bar)
I	0.5-2.5	60	0.21
II	20-24	50	0.04
III	33-38	70	0.019
IV	48.5-50	70	0.025

Table 5.4: P80 DM AGAR simulation - pressure oscillations blows characteristics.

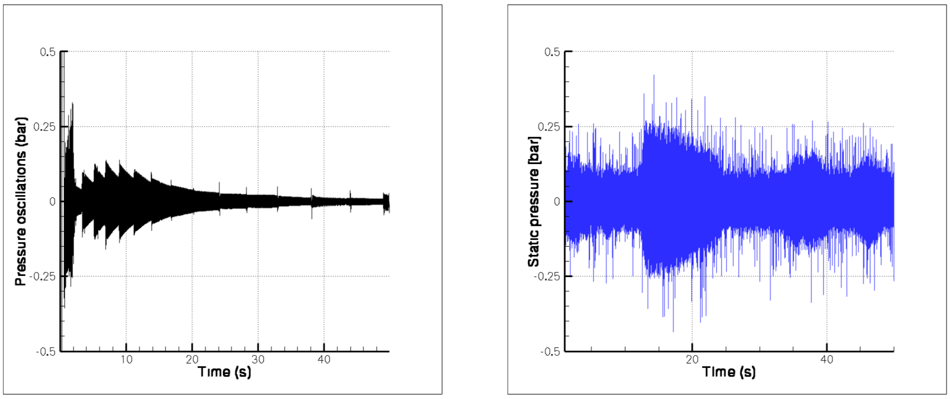

(a) AGAR (b) Experimental data

Figure 5.13: P80 DM AGAR simulation and experimental data (static sensor) - pressure oscillations.

In fig. 5.14, the frequency content of the numerical and experimental head pressure oscillating component is compared. AGAR simulation exhibits the first acoustic mode at ~ 61 Hz; the difference from the experimental value, ~ 50 Hz, is related to the Q-1-D nature of the adopted model.

Other significant frequency peaks are found around ~ 37, 103, 81-84 Hz. The frequency component at ~ 81-84 Hz is related to the acoustic frequency of the grain cylindrical part; its amplitude is reduced if compared with the other frequency components. Because of the grain regression, there is a decrease of the cylinder length with a slight increase of its acoustic frequency, as described by the double peak configuration.

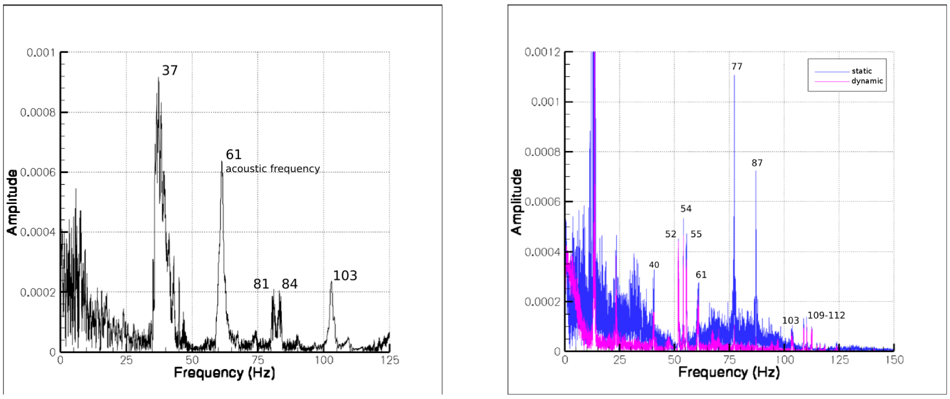

(a) AGAR (b) Experimental data

Figure 5.14: P80 DM AGAR simulation and experimental data (static sensor) - pressure oscillations spectrum.

A more detailed analysis of the pressure oscillation and of its frequency content can be obtained by filtering the signal around specific frequencies. These results, obtained for different frequency intervals, are shown in fig. 5.15. This kind of visualization permits a description of the frequency content as a function of the time evolution. While the first blow is characterized by a resonance frequency of ~ 60 Hz, the second is at ~ 50 Hz and both the third and fourth are at ~ 70 Hz. As already noted for the experimental data, the resonance frequency increases with the time. This increase corresponds to the presence of an higher number of slower vortices in the combustion chamber. This trend is in agreement with the flute-mode behavior.

The numerical oscillation also shows an important frequency contribution at ~ 40 Hz, between 2.5-20 s, and ~ 80 Hz, between 38-48 s; these contributions characterize the non resonant phases.

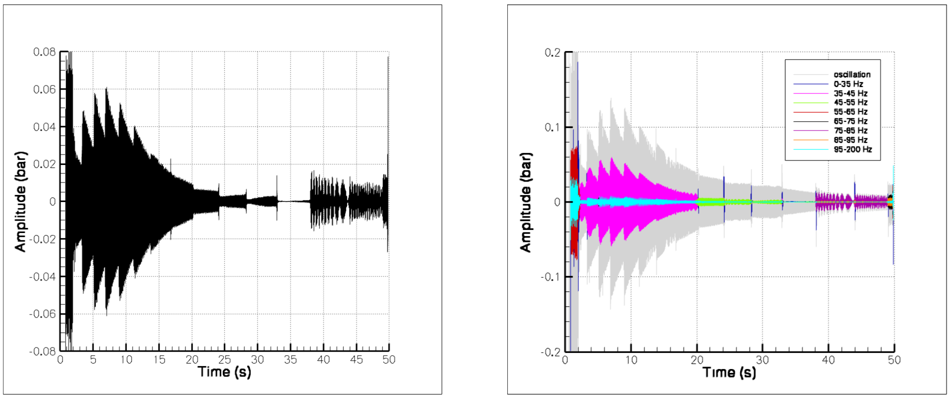

(a) 30-90 Hz (b) 35-85 Hz

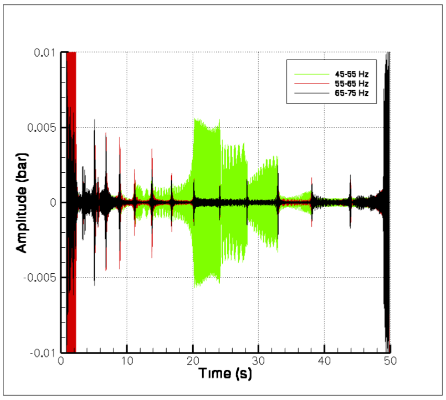

(c) 45-75 Hz

Figure 5.15: P80 DM AGAR simulation - filtered pressure oscillations.

5.4.3 HHT ANALYSIS OF THE HEAD PRESSURE OSCILLATIONS

The head pressure time evolution is not a periodic, linear and stationary signal. As done for the experimental data, the analysis of its frequency content is performed by using the Huang-Hilbert transform method. The HHT analysis provides both the amplitude and frequency time evolution.

The analysis is performed for four different time intervals (0-12 s, 10-30 s, 30-45 s and 40-50 s) covering the whole burning time (50 s).

Also the HHT method exhibits the presence of four different pressure oscillation blows, which properties, in term of amplitude and frequency, are summarized in tab. 5.5. Each blow is described by a constant frequency value; the first blow is characterized by an increasing amplitude, while a constant amplitude is obtained for the other blows.

blow	Time (s)	Frequency (Hz)	Amplitude (bar)
I	0.5-2.5	60	0.2-0.28
II	20-24	50-52	0.01
III	33-38	70	0.005
IV	49-50	70	0.016

Table 5.5: P80 DM AGAR simulation - head pressure HHT analysis.

The results of the HHT analysis for the first time interval (0-12 s) are shown in fig. 5.16. The first blow is described by the first IMF, red line, between 0.5-2.5 s. The amplitude reaches a maximum value of ~ 0.2-0.28 bar at ~ 1.75 s, while the frequency, ~ 60 Hz, slightly decreases. At 2.5 s, a sudden jump of both amplitude and frequency occurs (the second IMF, green line, < 0.02 bar and < 50 Hz), corresponding to the exit from the resonance condition.

The analysis of the second time interval (10-30 s) is visible in fig. 5.17. The second blow is between 20-24 s and it corresponds to the second IMF (green line). Both its amplitude and frequency present a constant value, ~ 0.01 bar and ~ 50 Hz. While the resonance condition is gradually attained, as shown by the slow increase of the second IMF frequency, the exit from this condition is characterized by a sudden jump of the frequency value.

The third time interval 30-45 s, fig. 5.18, shows the third blow between 33-38 s (second IMF, green line). Also in this case, the frequency and the amplitude are characterized by a constant vale, ~ 0.005 bar and ~ 70 Hz.

The HHT analysis of the fourth time interval 40-50 s is shown in fig. 5.19. The fourth blow is shown by the first IMF (red line) between 49-50 s. The frequency and the amplitude are respectively of ~ 70 Hz and ~ 0.016 bar. In this case, the oscillation frequency does not present a change in correspondence of the resonant coupling, but the amplitude shows a sudden increase.

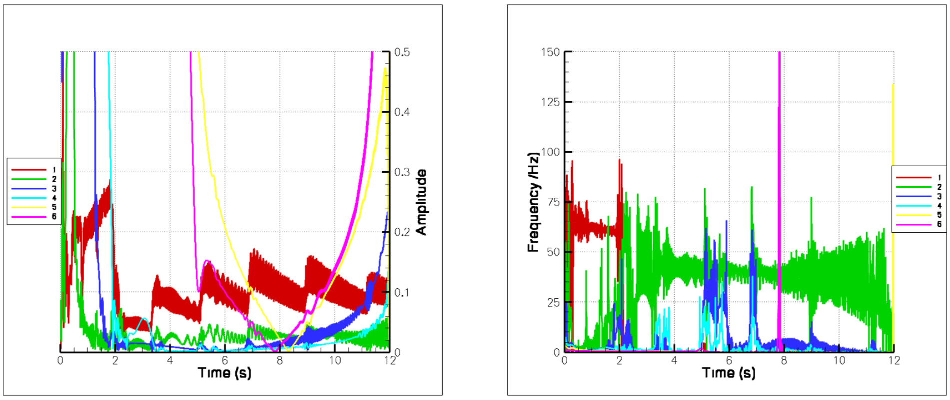

(a) Amplitude (b) Frequency

Figure 5.16: P80 DM AGAR simulation - head pressure HHT analysis, first blow.

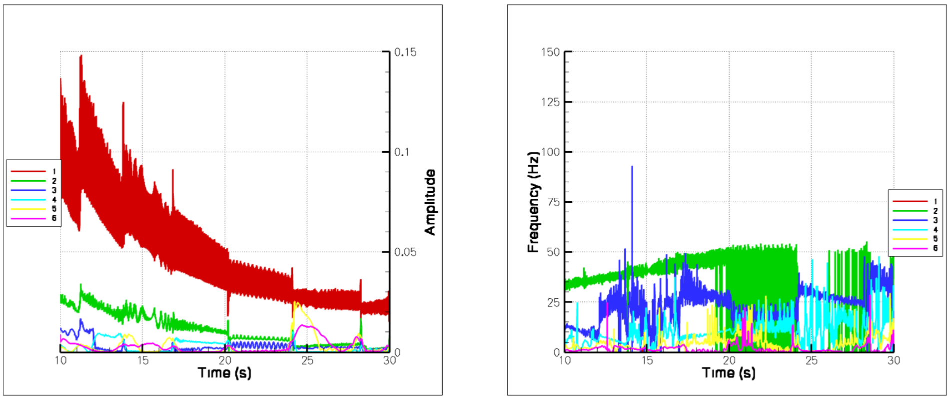

(a) Amplitude (b) Frequency

Figure 5.17: P80 DM AGAR simulation - head pressure HHT analysis, second blow.

5.4.4 THROAT PRESSURE AND VORTICITY (Ω) OSCILLATIONS

The head pressure oscillations exhibit frequency contributions at 37, 61, 81-84, 103 Hz. The origin of these contributions can be obtained by the analysis of the pressure signal, evaluated in the throat section, and of the vorticity (Ω) signal, evaluated at the vortex generation corner.

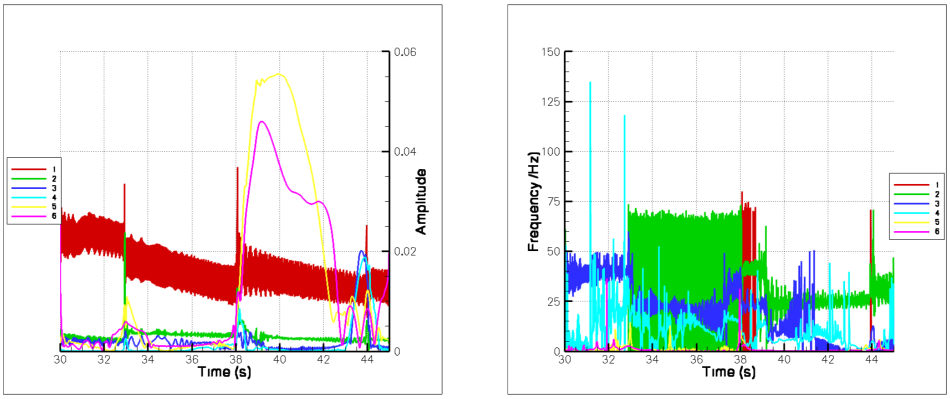

(a) Amplitude (b) Frequency

Figure 5.18: P80 DM AGAR simulation - head pressure HHT analysis, third blow.

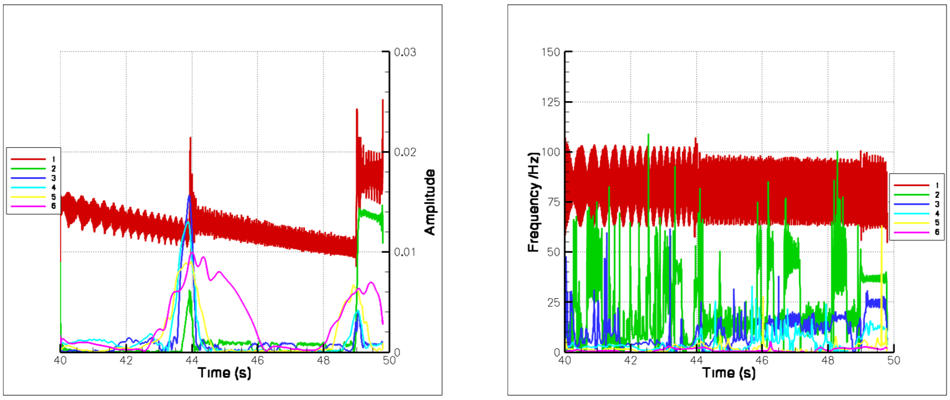

(a) Amplitude (b) Frequency

Figure 5.19: P80 DM AGAR simulation - head pressure HHT analysis, fourth blow.

THROAT PRESSURE OSCILLATIONS

In fig. 5.20 the pressure oscillations, computed at the head and the throat section, are compared. A first note can be done about the considerable damping effect, occurring mainly in the first 20 s, on the oscillation amplitude. Both the pressure oscillations, at the head and at the throat section, exhibit the same blow timing and frequency content.

Also in the throat section the first blow is at ~ 60 Hz, the second and the third are at ~ 50 Hz and the forth is at ~ 70 Hz; the first and the fourth oscillation phase are characterized by comparable amplitude, while the third is almost negligible.

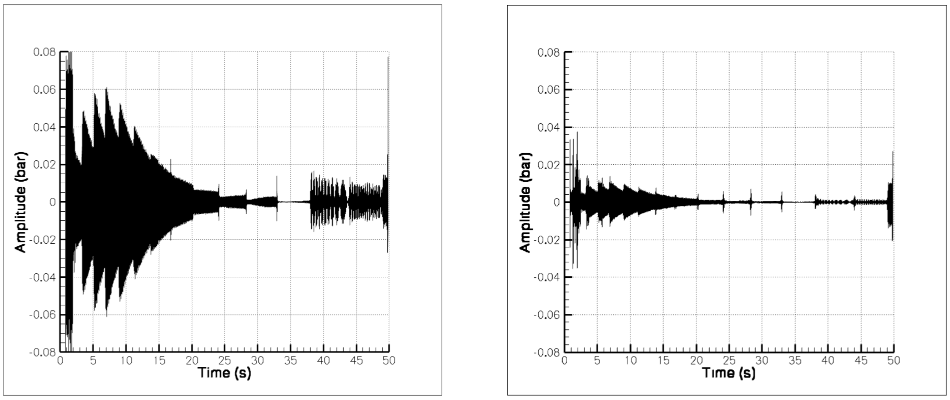

(a) Head - 30-90 Hz (b) Throat - 30-90 Hz

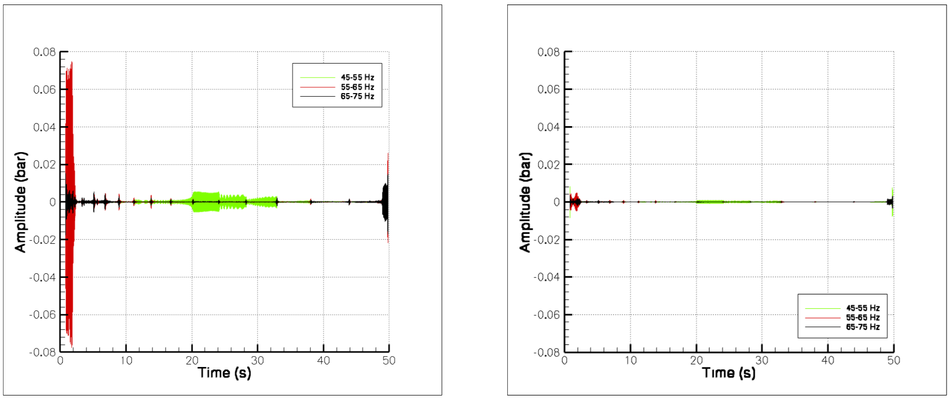

(c) Head - 45-75 Hz (d) Throat - 45-75 Hz

Figure 5.20: P80 DM AGAR simulation - head and throat pressure oscillations.

The spectra of the pressure oscillations here considered can be seen in fig. 5.21. The ~ 103 Hz frequency contribution, visible at the head section, is absent in the throat section. The other components are anyway visible, although they appear damped in the throat section; the peak at ~ 37 Hz remains the most important contribution while, due to the damping, the ~ 61 Hz and the ~ 81-84 Hz amplitudes become comparable.

The ~ 81-84 Hz component is the acoustic frequency of the cylindrical grain, while the ~ 103 Hz peaks is related to the vortex shedding phenomenon.

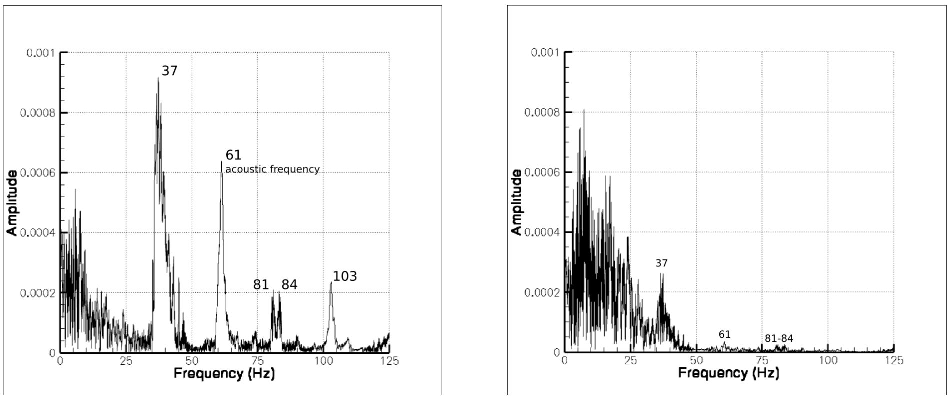

(a) Head

(b) Throat

Figure 5.21: P80 DM AGAR simulation - head and throat pressure oscillation spectrum.

VORTICITY (Ω) OSCILLATIONS

The vorticity (Ω) oscillations, evaluated at the corner and at the throat section, are shown in fig. 5.22. In both these points, four resonant oscillation phases can be distinguished, their timing is the same up to now noted.

At the corner, the amplitude of the first and the fourth blow, that is comparable, is greater than that of the second and the third blow.

The throat section is characterized by a considerable damping effect, and the first and the forth phases remain visible.

The first and the fourth phase of resonant coupling are respectively characterized by a frequency of ~ 60 Hz and ~ 70 Hz; the same frequency values have been noted for the pressure oscillation. On the contrary, the second and the third phase are described respectively by ~ 70 and ~ 60 Hz. This difference describes a possible energy passage from some frequencies to others, because of the acoustic mode excitation by vortex shedding.

The vorticity (Ω) spectra are shown in fig. 5.23. Both the frequency component at ~ 37 Hz and the acoustic frequency of the cylindrical grain (~ 81-84 Hz), visible at the corner position, are absent at the throat section. Two frequencies characterize the vorticity (Ω) both at the corner and at the throat section, the acoustic (~ 61 Hz) and the vortex shedding frequency (~ 103 Hz).

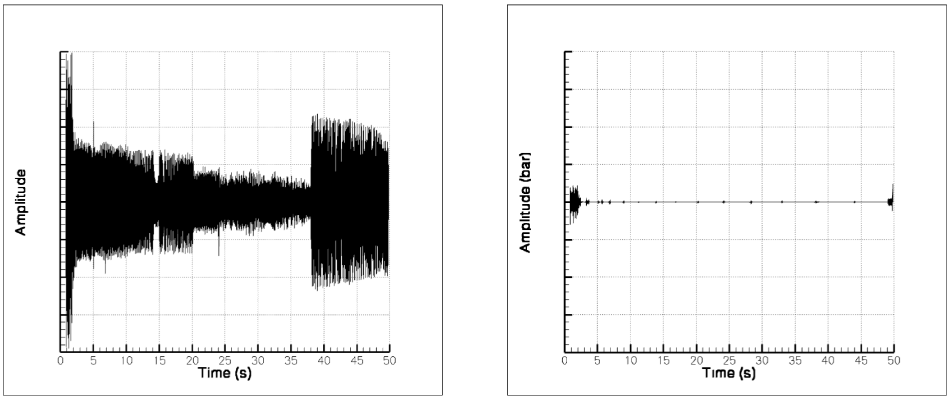

(a) Corner - 30-90 Hz (b) Throat - 30-90 Hz

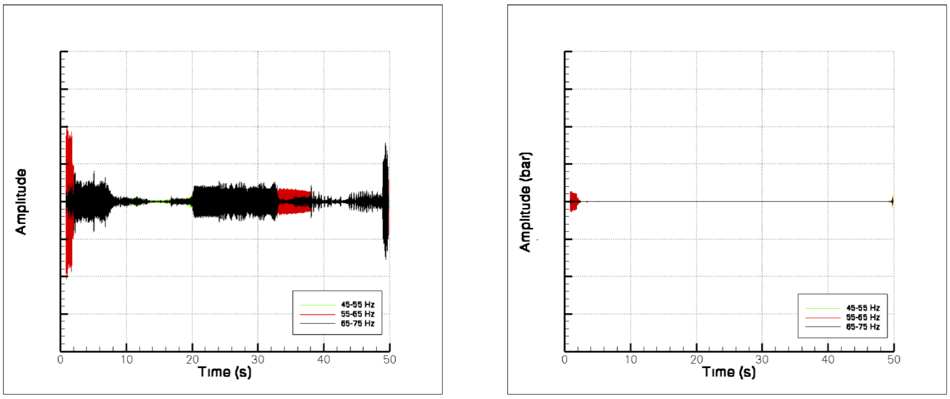

(c) Corner - 45-75 Hz (d) Throat - 45-75 Hz

Figure 5.22: P80 DM AGAR simulation - corner and throat section vorticity (Ω) oscillations.

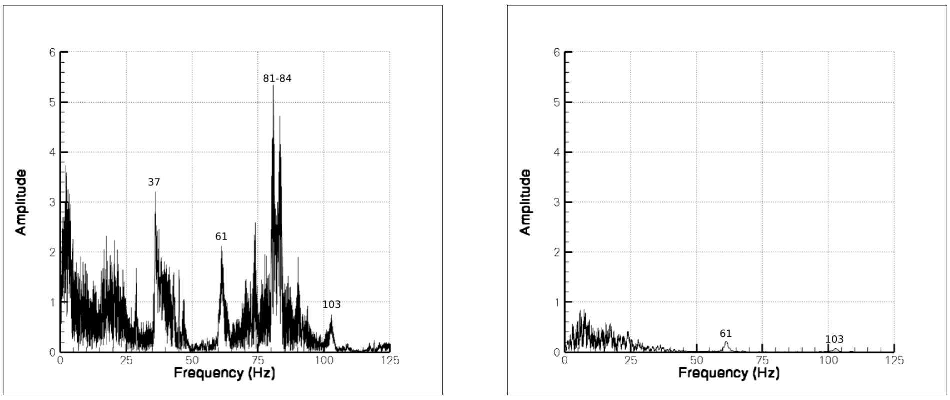

(a) Corner (b) Throat

Figure 5.23: P80 DM AGAR simulation - spectrum of the corner and throat vorticity (Ω) oscillation.

5.4.5 Vortex separation criterion

The vortex shedding point is always assumed at the corner connecting the cylinder and the star grain. The adopted separation criterion has been discussed in par. 3.5.3.

In fig. 5.24, 5.25, 5.26, 5.27 the separation conditions for each resonance phase are shown.

The vortex detachment frequency depends on the flow conditions, so that it changes during the combustion time. AGAR simulation shows that the shedding frequency decreases with the grain combustion and regression: from 128 Hz for the first blow, to 120 Hz for the second, 113 Hz for the third and 80 Hz for the fourth.

The pressure and velocity time evolutions show that a pressure descending node always corresponds to a velocity antinode. For the first three blows the vortices detached in correspondence of a relative velocity maximum (velocity positive antinode); this condition is confirmed by literature results. On the contrary, for the fourth blow the separation occurs in correspondence of a velocity relative minimum (velocity negative antinode).

The time evolution of the pressure second time derivative of the fourth blow exhibits a strong distortion from purely sinusoidal behavior (fig. 5.27); this deformation is higher than that shown by the other three blows (fig. 5.24, 5.25, 5.26).

The dimension of the detached vortices, fig. 5.28, shows that in resonance condition the released vortices are characterized by the same dimension.

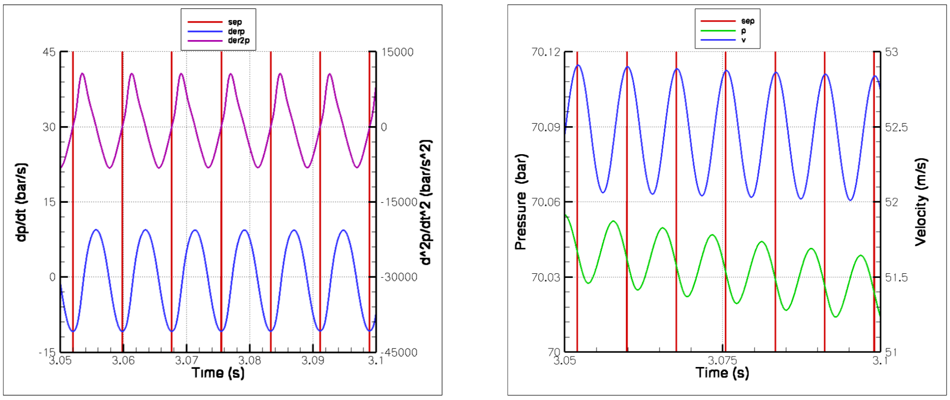

(a) First and second pressure derivative (b) Pressure and velocity

Figure 5.24: P80 DM AGAR simulation - detachment conditions at vortex separation point, first blow.

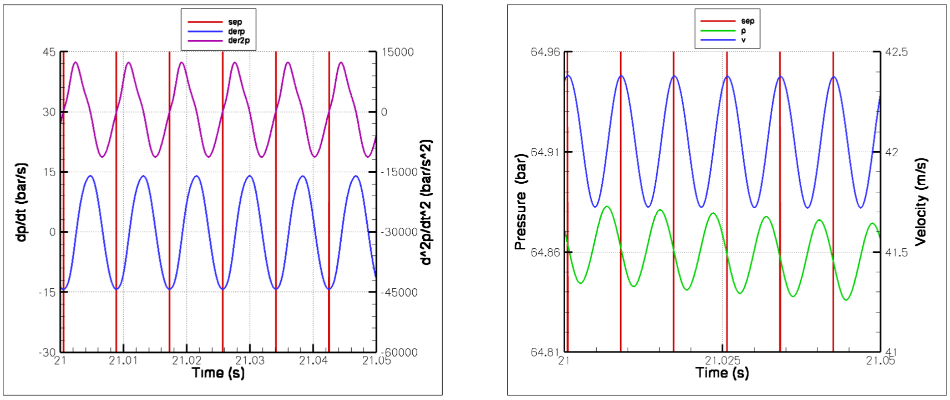

(a) First and second pressure derivative (b) Pressure and velocity

Figure 5.25: P80 DM AGAR simulation - detachment conditions at vortex separation point, second blow.

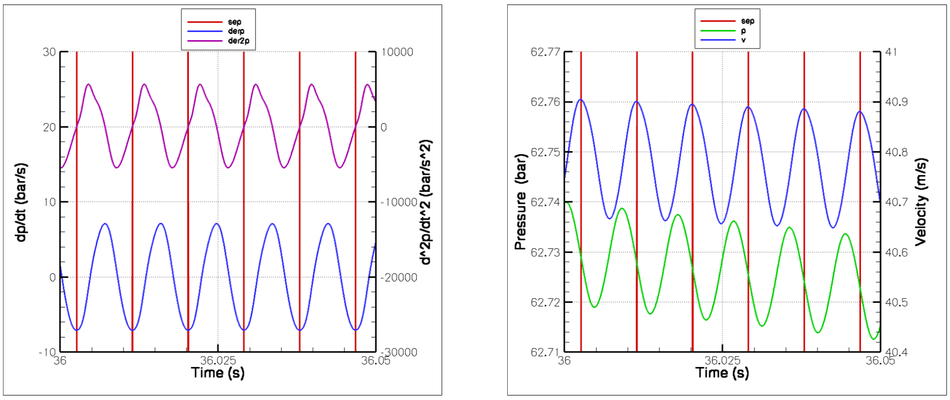

(a) First and second pressure derivative (b) Pressure and velocity.

Figure 5.26: P80 DM AGAR simulation - detachment conditions at vortex separation point, third blow.

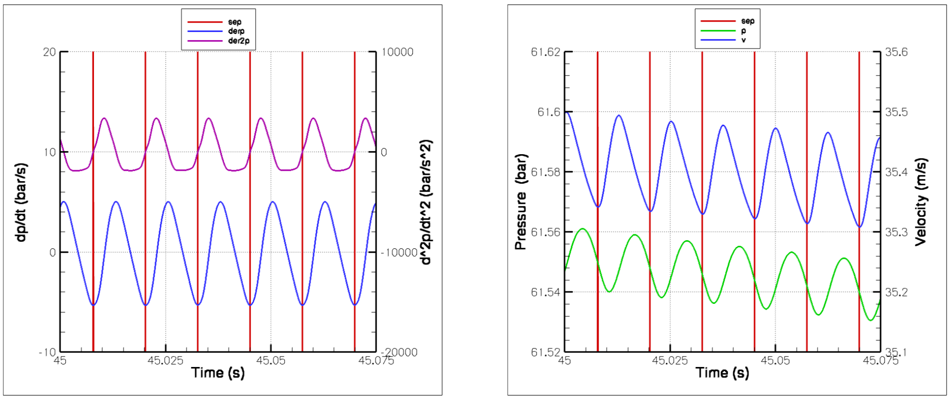

(a) First and second pressure derivative (b) Pressure and velocity

Figure 5.27: P80 DM AGAR simulation - detachment conditions at vortex separation point, fourth blow.

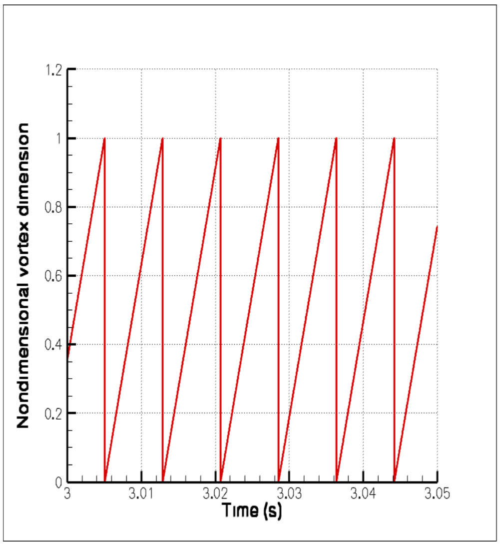

Figure 5.28: P80 DM AGAR simulation - non dimensional vortex dimension in resonant condition.

5.4.6 POX MODEL SOURCE TERMS ANALYSIS

The vorticity convection equation of the POX model, eq. 3.50, has a source term, modeled as in eq. 3.51, that is defined only at the vortex detachment point.

In fig. 5.29, the distribution of the vorticity equation source term along the combustion chamber is shown; it is clearly visible that it exists only in correspondence of the step position (0.75 of non dimensional axis).

The momentum and energy equations source terms, eq. 3.56, are defined in all that points characterized by $\frac{dA_p}{dx} \neq 0$. As noticeable in fig. 5.29, the acoustic field excitation, related to the vortex interaction with geometrical variations, is active from the corner to the nozzle throat; the most important contribution is due to the nozzle nose and to the submergence region.

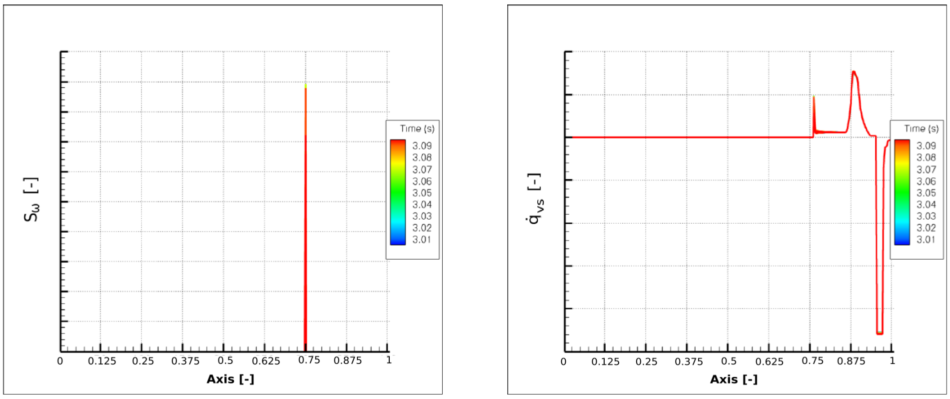

(a) Vorticity equation source term (b) Momentum equation source term

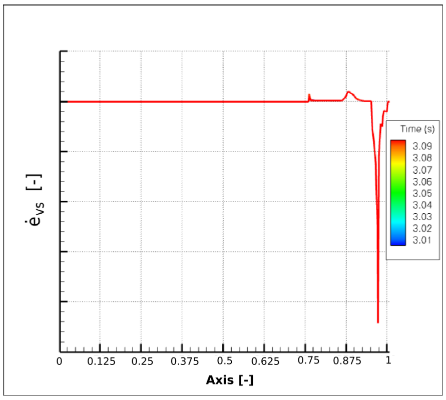

(c) Energy equation source term

Figure 5.29: P80 DM AGAR simulation - POX model source terms.

5.4.7 VORTICITY (Ω) DISTRIBUTION

The presence of a vortex in the combustion chamber corresponds to a relative maximum of the vorticity (Ω) distribution.

The vorticity (Ω) distribution that characterizes each resonant phase is shown in fig. 5.30. The number of vortices in the combustion chamber increases with time, from four of the first blow to five-six of the fourth. With the grain regression, the core flow velocity decreases, and the combustion chamber presents an higher number of slower vortices.

With the convection towards the nozzle, the vorticity (Ω) is gradually damped. As shown in fig. 5.30, the resonance condition is characterized by a regular vorticity (Ω) envelope, due to the detachment of vortices, with the same dimension and intensity, at the same frequency.

5.4.8 PRESSURE AND VELOCITY DISTRIBUTION

The pressure and the velocity distribution in the combustion chamber, for each considered time interval, are shown in fig. 5.31, 5.32, 5.33, 5.34. Their time derivative is also displayed to facilitate the description of the field structure and the identification of the position of nodes and antinodes.

The velocity and pressure distribution underlines a decrease, from the first to the fourth blow, of the oscillation amplitude.

The head section always corresponds to a velocity node, always characterized by a zero velocity value. Each analyzed time interval, with the only exception of the fourth, is described by a similar configuration in the combustion chamber: two pressure nodes and a velocity antinode, corresponding to the step position.

In the following, the node and the antinode position is indicated with respect to the non dimensional axis.

The first blow, fig. 5.31, exhibits two pressure nodes at 0.293 and 0.815, each one corresponding to a velocity antinode. A velocity node, in addition to the head section, is at 0.545.

The second blow, fig. 5.32, presents a pressure node position variable with the time. The first pressure node is slightly moving between 0.295-0.3, and the second between 0.8-0.825. The velocity node is almost fixed at 0.57. If compared with the first blow configuration, each node seems shifted towards the throat section.

In fig. 5.33, the third blow presents a first pressure node around 0.308-0.318, while the second has a not precise position. The velocity node is at 0.593.

As shown in fig. 5.34, the fourth blow exhibits two velocity nodes, corresponding to the head and to the throat section. Any other feature is difficult to be determined, and the field structure is quite different if compared to the other resonant cases.

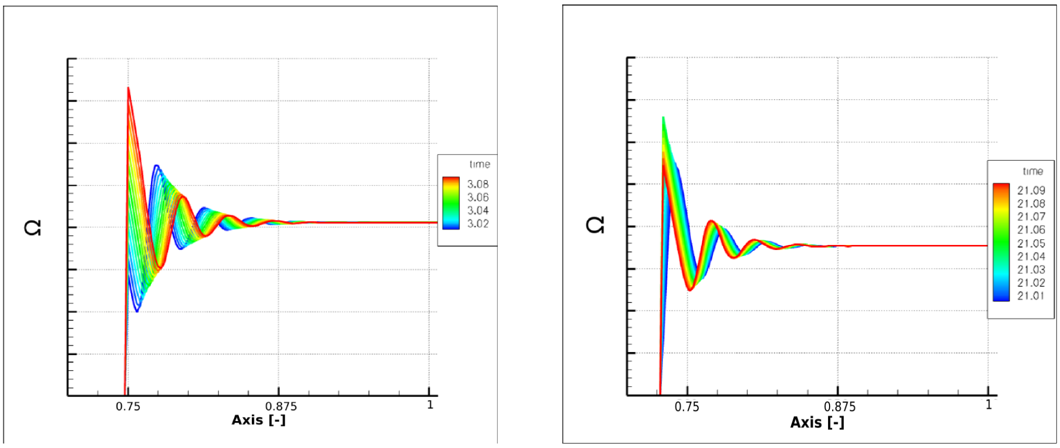

(a) First blow (b) Second blow

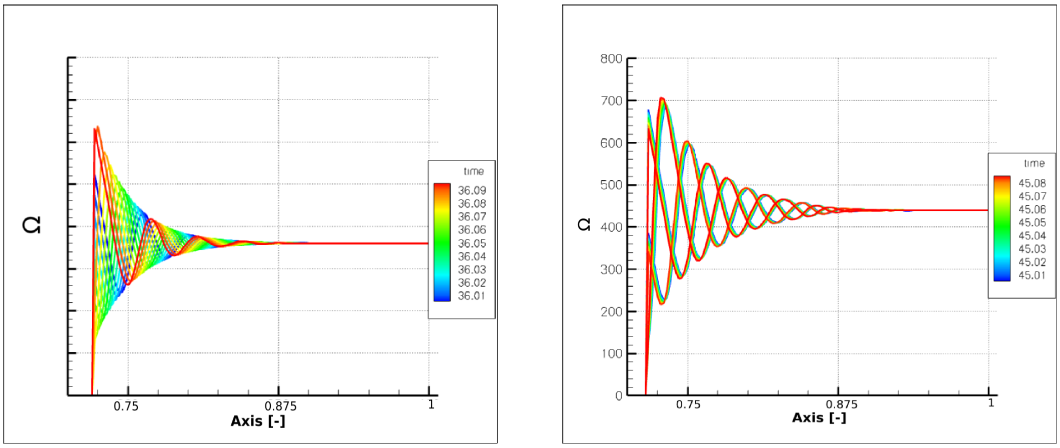

(c) Third blow (d) Fourth blow

Figure 5.30: P80 DM AGAR simulation - vorticity (Ω) distribution.

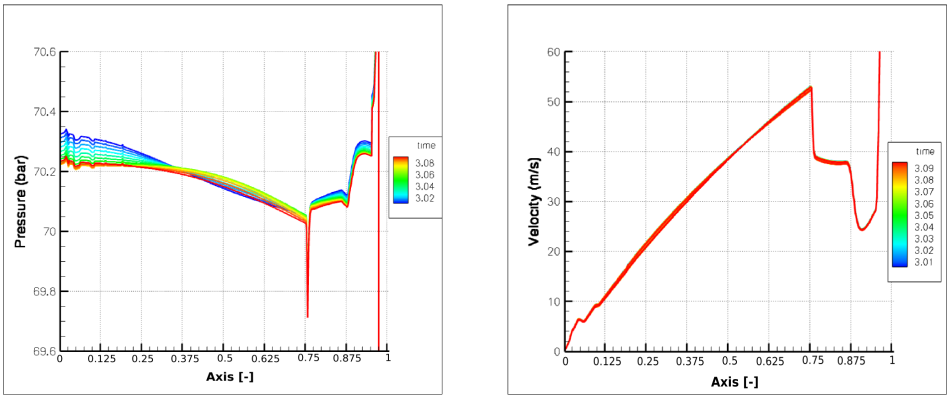

(a) Pressure (b) Velocity

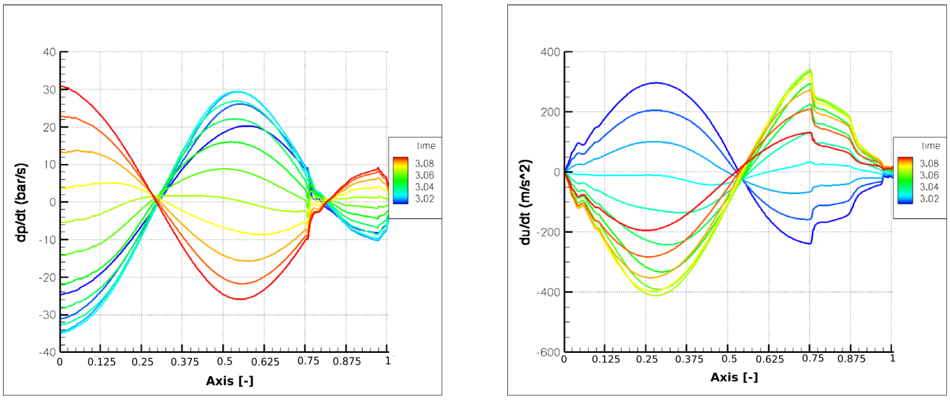

(c) Pressure time derivative (d) Velocity time derivative

Figure 5.31: P80 DM AGAR simulation - pressure and velocity distribution, first blow.

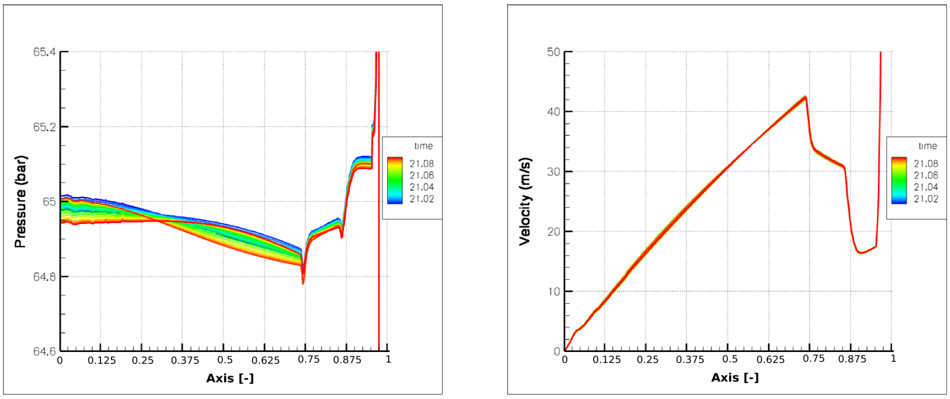

(a) Pressure (b) Velocity

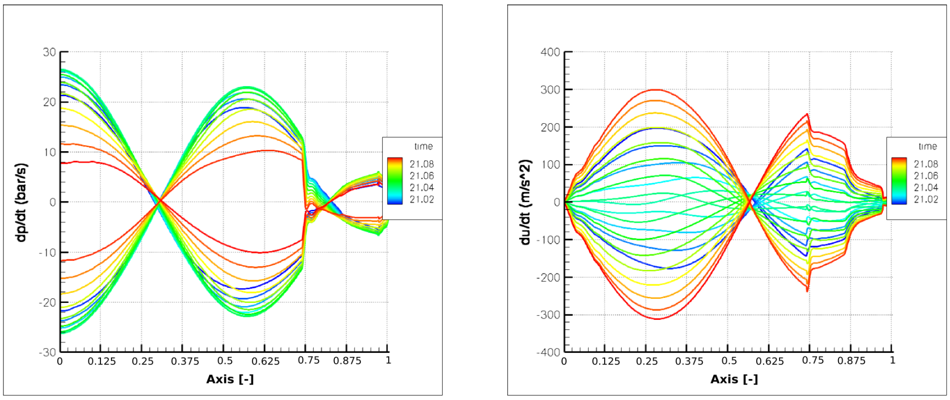

(c) Pressure time derivative (d) Velocity time derivative

Figure 5.32: P80 DM AGAR simulation - pressure and velocity distribution, second blow.

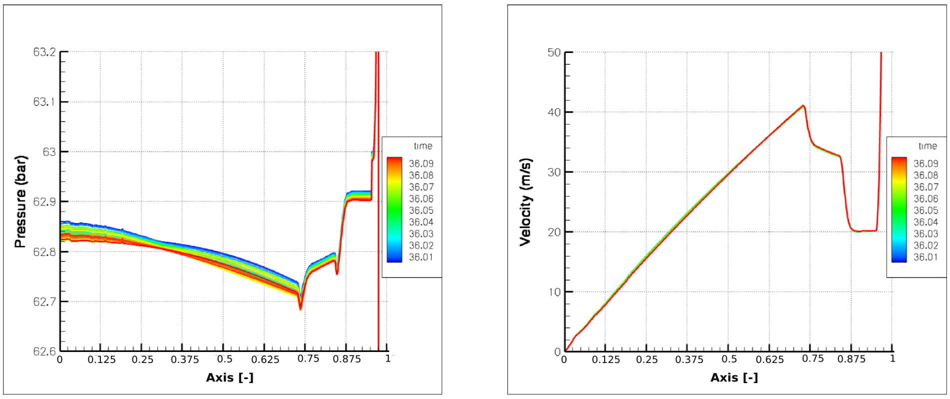

(a) Pressure (b) Velocity

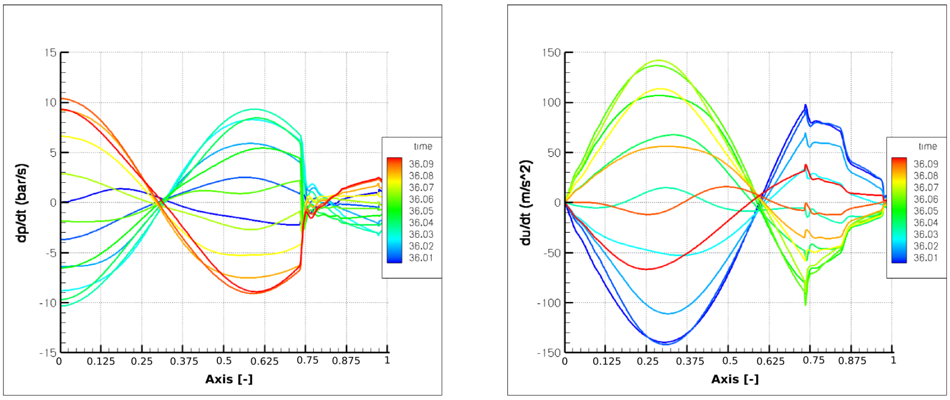

(c) Pressure time derivative (d) Velocity time derivative

Figure 5.33: P80 DM AGAR simulation - pressure and velocity distribution, third blow.

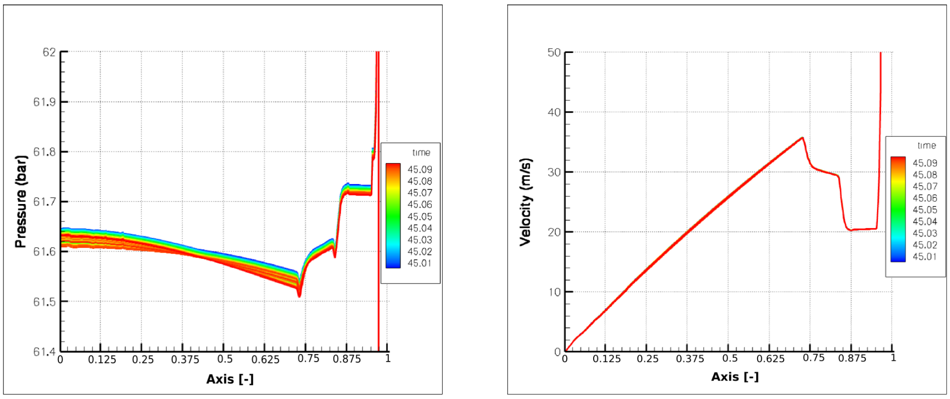

(a) Pressure

(b) Velocity

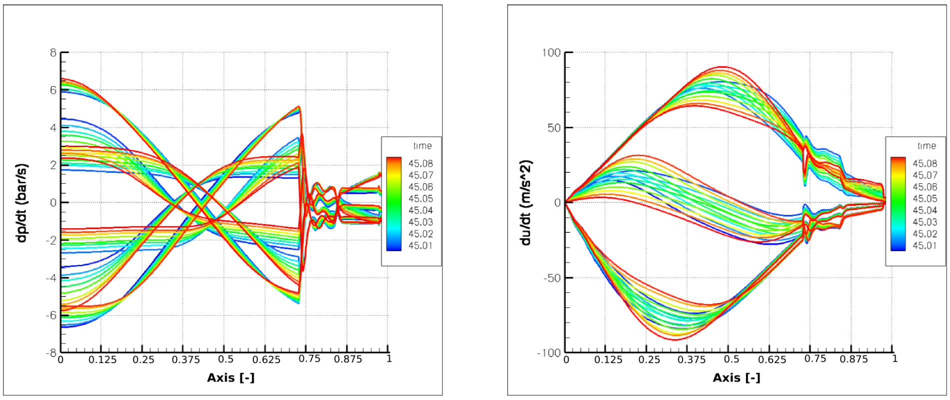

(c) Pressure time derivative

(d) Velocity time derivative

Figure 5.34: P80 DM AGAR simulation - pressure and velocity distribution, fourth blow.

5.5 CAVITY EFFECT

The P80 DM geometrical configuration is characterized by a significant submergence region volume; during the combustion time, the volume ratio $\left(\frac{V_s}{V_c + V_s}\right)$ increases from 0.117 to 0.134. Because of this cavity volume, the Helmholtz resonator effect can not be neglected.

AGAR model has been used to study the cavity response of the P80 DM solid rocket motor.

Three different cases are here considered for the analysis of the cavity effect. The first case is represented by the P80 DM combustion chamber without any submergence region. In addition, the P80 geometrical configuration is analyzed with two different cavity response. The cavity model has been described in par. 3.7.3; the cavity response is calibrated by the α_{cav} parameter. A reference value of $\alpha_{cav} = 0.02$ is typically used, derived from earlier studies on the model. In this case, an higher response of the cavity has been obtained with an $\alpha_{cav} = 0.04$, while a lower response with an $\alpha_{cav} = 0.005$. The absence of the cavity is described by using an $\alpha_{cav} = 0$.

The head pressure time evolution, obtained for each case, is shown in fig. 5.35.

The $\alpha_{cav} = 0.04$ clearly indicates that there is a stability limit to the increase of the cavity response. This instability corresponds to the burst visible at ~ 30 s, the low frequency explosion in fig. 5.36. Obviously, this unstable behavior makes the obtained solution useless.

The absence of cavity is characterized by a lower head pressure value, because of the large cavity mass addition (fig. 5.35).

When the submergence grain is completely burned, the head pressures obtained for each case collapse on the same value.

Despite the cavity presence or response, the vortex shedding phenomenon is anyway present, and it is described by similar fundamental characteristics. The analysis of the frequency content of the pressure oscillations can be seen in fig. 5.36, 5.37.

The first and more pronounced effect of the cavity presence, and then of its response, is the oscillation amplitude modulation; the obtained results are in agreement with literature results.

Two frequency components, almost not visible if the cavity is not considered, are strongly amplified, ~ 60 and ~ 103 Hz; the peaks at ~ 37 and ~ 81-84 Hz are anyway present. The frequencies that describe the motor aeroacoustic coupling do not exhibit any variation.

The cavity model here considered has been developed focusing on the submergence effects during the ignition transient. Although its correct description, the development of a suitable model, accounting for the stationary phase phenomena, represents a useful task.

This improvement does not affect the physical description of the aeroacoustic coupling, but it can provide a better quantitative accuracy on the amplitude evaluation.

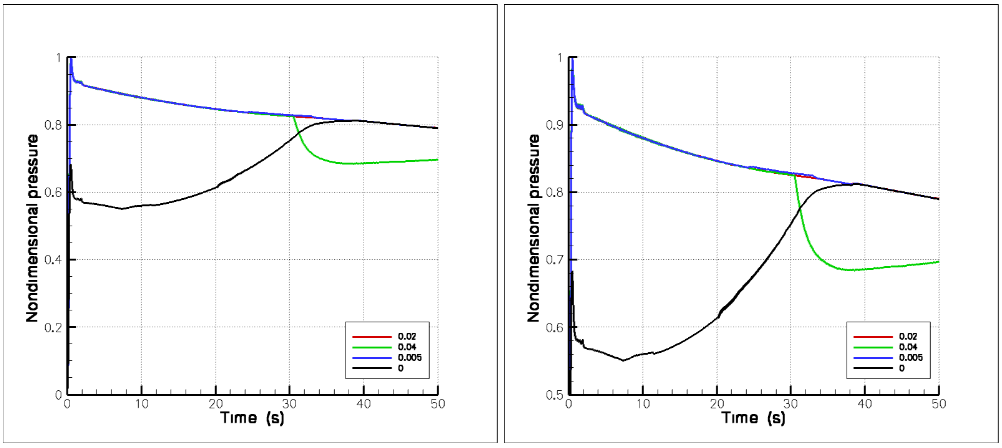

Figure 5.35: P80 DM AGAR simulation - cavity effects on the head pressure evolution.

5.6 CONCLUSIONS

In this chapter, the AGAR numerical simulation of the P80 DM solid rocket motor has been presented. The geometrical evolution of the combustion chamber is evaluated, with the assumption that the only corner vortex shedding occurs and neglecting the two phase flow and combustion instability effects. AGAR model only describes the vortex shedding term related to the radial addition, here modeled as the addition due to the presence of a corner. Both compressibility and deformation effects are not accounted.

For the P80 SRM, AGAR model describes a vorticity formation in correspondence of the grain corner, at the connection between the cylindrical and the star grain. The first loop is related to the distance between the corner and the nozzle throat, the second loop is a function of the chamber length. AGAR simulation shows the existence of four resonant phases for the P80 SRM. Their characteristics, compared with the experimental data, are summarized in tab. 5.6.

Coherently with the static firing test results, four different resonant phases can be identified in the first 50 s of the combustion time.

Except for the last, that presents a slight time shift, the numerical blows are included in the experimental time intervals, and this indicates a good agreement with the experimental blow timing.

AGAR simulation shows a good amplitude estimation for the first and the fourth blow amplitude; an underestimation of one order degree is instead exhibited for the second and the third resonant phase.

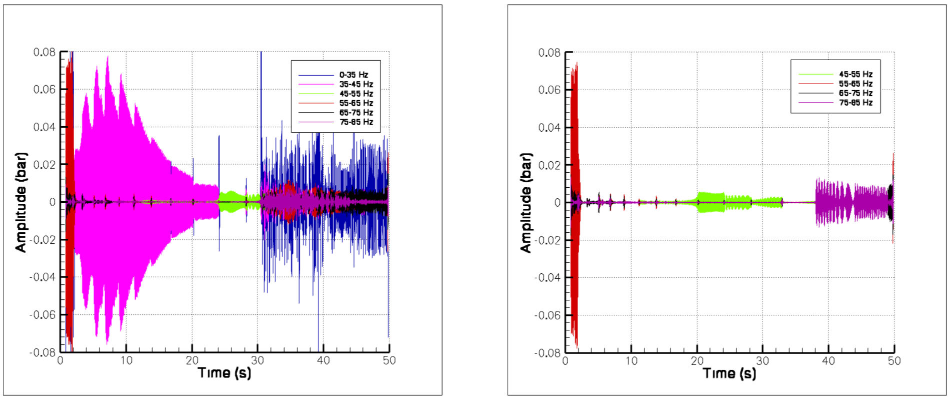

(a) α_{cav}=0.04

(b) α_{cav}=0.02

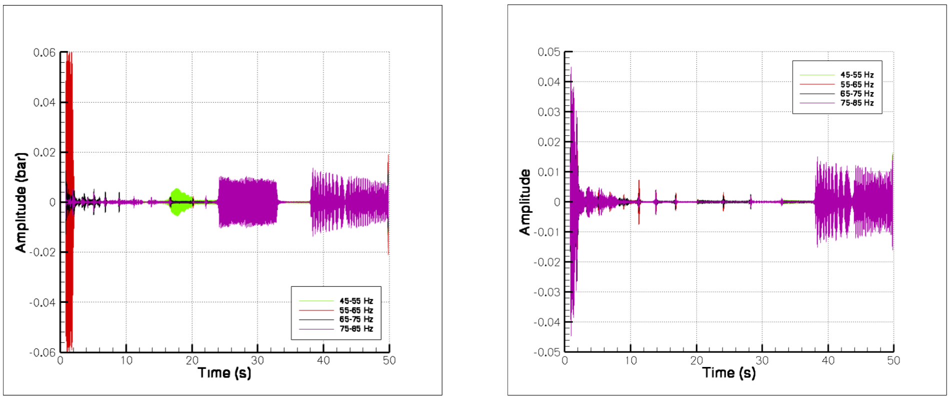

(c) α_{cav}=0.0025

(d) α_{cav}=0

Figure 5.36: P80 DM AGAR simulation - filtered head pressure oscillation.

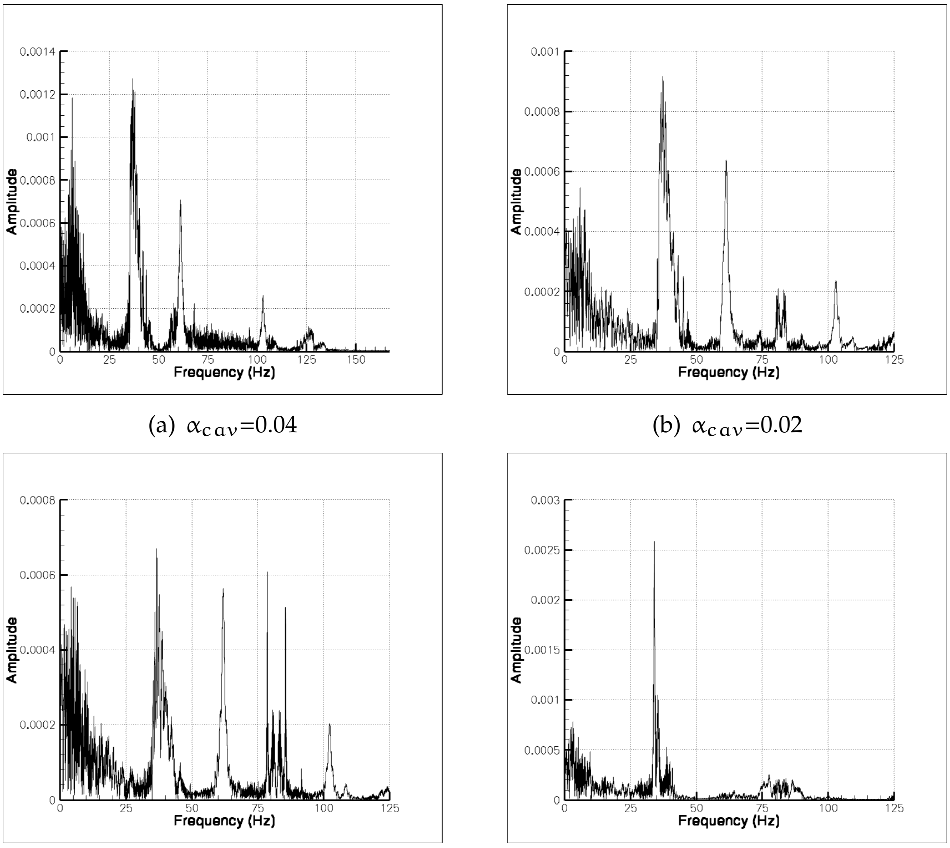

(a) α_{cav}=0.04

(b) α_{cav}=0.02

(c) α_{cav}=0.0025

(d) α_{cav}=0

Figure 5.37: P80 DM AGAR simulation - the head pressure oscillation spectrum.

	Experimental data	AGAR results
I - timing	1.6 - 5.9	0.5 - 2.5
I - frequency	50	60
I - amplitude	0.217	0.2-0.28
II - timing	12.6 - 24.4	20 - 24
II - frequency	51	50-52
II - amplitude	0.209	0.01 - 0.04
III - timing	34.5 - 39.5	33 - 38
III- frequency	54	70
III - amplitude	0.112	0.005 - 0.019
IV - timing	44 - 48.5	48.5 - 50
IV - frequency	55	70
IV - amplitude	0.061	0.016 - 0.025

Table 5.6: P80 DM experimental data and AGAR simulation results.

AGAR correctly describes the general trend of the increasing oscillation frequency. The Q-1-D nature of the adopted model determines a difference on the acoustic frequency evaluation, related to a difference on the frequency value of each resonant phase.

Despite some quantitative difference, AGAR model appears capable of providing a good phenomenological description of the aeroacoustic coupling mechanism, as confirmed by the experimental data. In particular the model describes the system adjustment to resonance condition and the following exit.

In addition to the experimental data, also the Rossiter's model is used for a comparison with AGAR results. While Rossiter's analysis shows that any resonance solution can be found for the P80 DM configuration, AGAR simulation correctly determines the presence of four resonant phases.

The qualitative differences on the obtained results seems to suggest that the neglected phenomena, such as two phase flow and combustion instabilities, can influence the aeroacoustic coupling mechanism.

The development of a proper cavity model for the stationary phase represents a useful task to improve the oscillation amplitude evaluation,.

CONCLUSIONS

In the present work a new model, named AGAR, for the simulation of acoustic resonance of solid rocket motor has been presented. The system of governing equations is written in quasi-one dimensional form. The model provides a description of the pressure, and thrust, resonant oscillations that can affect the quasi steady state of a SRM. The analysis of the obtained pressure signal, makes it possible to obtain a complete characterization of the oscillations in terms of frequency and amplitude.

An unsteady Eulerian model with mass, momentum and energy addition and a geometrical evolution, both in space and time, is considered. Two phase flow effects are neglected and a mixture of non reacting perfect gases is considered. The thermophysical properties of the mixture of ideal gases are variable in space and time; they are evaluated using a thermodynamic standard model for mixtures. Moreover, the grain combustion reactions are supposed to occur in an ideal thin layer on the grain propellant surface. The effects related to combustion instability are not considered.

The governing equations that have to be considered are the mass, momentum and energy conservation equations, plus a vorticity equation. The three dimensional form, expressed in cylindrical coordinates for an axisymmetric flow and averaged on the normal sections, allows to obtain a quasi-one dimensional model. As far as the vorticity equation is concerned, neglecting the compressibility effect and the deformation contribution, the radial addition due to a propellant corner is the only considered vortex shedding phenomenon.

A proper model describes the vortex creation and growth, accounting for the acoustically forced vortex generation. The vortex dynamics description is completed by a vortex detachment criterion, and a quasi-one dimensional equation that describes the vorticity convection by the flow. The acoustic mode excitation by vortex impingement is modeled with the introduction of source terms in the Euler's equations.

AGAR model is made of: a gasdynamic model, a model to evaluate the combustion rate of ignited propellant grain (evaluation of the mass addition from burning surface), a model to determine the evolution of chamber geometry and an aeroacoustic model. SPINBALL (Solid Propellant rocket motor INternal BALListics) is the adopted quasi-1D unsteady gasdynamic model, while the used 3D grain burn back model is GREG (Grain

REGression). The developed aeroacoustic model, here presented, is the POX model (it's not an acronym); it is composed by: a model to determine the vortex dynamics (creation, growth, convection and destruction), a model to evaluate the acoustic field excitation by vortex shedding, a model to estimate the acoustically forced vortex generation. A quasi-1D equation describes the vorticity convection by the flow. The acoustic mode excitation by vortex impingement is modeled with the introduction of source terms in the gasdynamic model.

A first test case, proposed for AGAR validation, is the simulation of cold flow in an axisymmetric ramjet combustor, a simple case that allows a description of pure aeroacoustic coupling; the same test case performed by Jou and Menon has been considered. AGAR simulation exhibits main flowfield features in accordance with Jou and Menon's results, as shown by the system non resonant conditions and by the pressure node position. The system fundamental frequencies, for both acoustics and vortex shedding, are correctly evaluated, and the pressure and vorticity spectrum show that their interaction is correctly described. A low frequency peak, visible in Jou and Menon's simulation can not be seen in AGAR results.

In order to describe and to analyze the possible coupling between the acoustics and the vortex shedding, different initial flowfield conditions are considered. Each analyzed case presents a correct phenomenological description of the interaction between acoustics and vortex shedding; the frequency content of the pressure oscillations is properly reconstructed and the nature of each frequency peak is identified. AGAR model describes resonant and non resonant conditions, and the system adjustment towards the acoustic coupling. One of these cases is directly comparable with Jou and Menon's results. Both the simulations show a system moving towards resonant condition, but while they obtain only a movement towards this condition, AGAR shows the attainment of a complete resonant case.

AGAR is then used for the simulation of the acoustics of a solid rocket motor. The P80 DM SRM, first stage of the new European small launcher Vega, has been considered as test case.

In agreement with the experimental static firing tests, the P80 DM numerical simulation exhibits four phases of resonant pressure oscillations in the first 50 s of the combustion time. With the exception of the last phase, presenting a slight time shift, the simulation shows a good agreement with the experimental oscillation timing. AGAR simulation shows a good estimation of the first and the fourth phase amplitude, while the second and third resonant phase present an underestimation of one order degree.

The Q-1-D nature of the adopted model determines a difference on the acoustic frequency evaluation, corresponding to a difference on the resonant frequency of each phase. Anyway, AGAR correctly describes the general trend of the increasing oscillation frequency.

Despite some quantitative difference, AGAR appears capable of a good phenomenological description of the aeroacoustic coupling mechanism, as confirmed by the experimental data. The model describes the system adjustment to resonance condition and the following exit.

The aeroacoustics of a solid rocket motor is a quite complex subject, that involves several different phenomena.

The model here presented shows a good description of the main aspects related to the aeroacoustic coupling, but it can be considered a first step. A deepening of the model analysis appears necessary, combined with the improvement of the adopted model, and the possible introduction of some phenomena until now neglected (i.e: two phase flow effects,...). These activities have to be obviously combined with the model application to other solid rocket motors that exhibit pressure oscillations.

THE END

E quindi uscimmo a riveder le stelle.

Dante Alighieri,La Divina Commedia, Inferno XXXIV

A

FOURIER TRANSFORM

The *Fourier Transform* (FT) is the common approach in spectrum analysis.

The Fourier Transform is based on a globally defined orthogonal basis and requires a periodic and linear function; it reduces the analyzed signal into harmonic components and provides an amplitude vs. frequency description of the analyzed data.

A.1 THE FOURIER TRANSFORM

The FT can be applied to a function $f(x)$ characterized by a finite number of discontinuities and with integrable $|f(x)|$ and $|f(x)|^2$. The function have to be periodic, of period T $[f(x+T) = f(x)]$.

The *Fourier transform* $\hat{f}(\omega)$ is defined as the complex function:

$$\hat{f}(k) = \Im_f(k) = \frac{1}{2\pi}\int_{\Re} f(x)e^{-jkx}dx \tag{A.1}$$

while the *inverse Fourier transform* $F(x)$ corresponds to the following expression:

$$F(x) = \Im_{\hat{f}}^{-1}(x) = \int_{\Re} \hat{f}(k)e^{jkx}dk \tag{A.2}$$

If $\hat{f}(k)$is the Fourier transform of $f(x)$, under sufficiently general conditions, the following expression is verified:

$$F(x) = f(x) \tag{A.3}$$

A.2 THE FOURIER SERIES

For the periodic and integrable[1] function $f(x)$, the *Fourier series* is defined as:

$$F_S = \sum_{k=-\infty}^{\infty} \hat{f}_k e^{jk\frac{2\pi}{T}x} \tag{A.4}$$

---

[1] This condition is required for the definition of the Fourier coefficient.

where the $\hat{f}_k$ coefficients are expressed as:

$$\hat{f}_k = \frac{1}{T}\int_0^T f(x)e^{-jk\frac{2\pi}{T}x} \tag{A.5}$$

The Fourier serie is equivalent to the Fourier transform of periodic generalized function.

A.3 THE FAST FOURIER TRANSFORM

The *Fast Fourier Transform* algorithm is the standard numerical implementation for the calculation of a Fourier transform. It represent an efficient tool to evaluate the Discrete Fourier Transform, especially if N is a power of 2.

A data set of $N + 1$ uniformly spaced points is considered:

$$f_i = f(x_i) \tag{A.6}$$

$$x_i = (i-1)\,\Delta x \tag{A.7}$$

where $i = 1, ..., N$ and $N = 2^n$.

The Fourier coefficient can be expressed as:

$$\tilde{f}_k = \frac{1}{N}\sum_{i=1}^{N} f_i e^{-jk\frac{2\pi}{N}i} \tag{A.8}$$

that allows to write the *Discrete Fourier transform* (DFT) as:

$$f(x) \sim \sum_{k=-N/2}^{N/2-1} \tilde{f}_k e^{jk\frac{2\pi}{T}x} \tag{A.9}$$

where the approximation is due to the truncation of the serie and to the approximation of the Fourier coefficient. If this expression is evaluated in the x_i points, it is possible to obtain:

$$f_i \sim \sum_{k=-N/2}^{N/2-1} \tilde{f}_k e^{jk\frac{2\pi}{T}i} \tag{A.10}$$

that reproduce exactly the f value in the x_i nodes.

If x_i represents the time domain data, $\tilde{f}_k$ is the representation in frequency domain. The frequency data can be expressed as an amplitude spectrum:

$$A_k = \frac{2}{N}|\tilde{f}_k| \tag{A.11}$$

or as a power spectrum:

$$P_k = \frac{|\tilde{f}_k{}^2|}{N} \tag{A.12}$$

where $k = 0, .., N/2$.

B

HILBERT-HUANG TRANSFORM

The *Hilbert-Huang transform* HHT allows the spectrum analysis of nonlinear and non stationary data.

The HHT provides a data description in terms of both amplitude and frequency time evolution.

B.1 THE HILBERT-HUANG TRANSFORM

The most important aspect of the HHT analysis is the capability to treat nonlinear and non-stationary data.

The Hilbert-Huang transform (HHT) is composed by two steps:

1. the empirical mode decomposition (EMD) process, that decomposes the signal into a set of intrinsic mode functions (IMFs)

2. the Hilbert spectral analysis (HSA), that extracts the frequency vs. time information from each IMF

This method is based on an adaptive basis, and the frequency is defined through the Hilbert transform.

B.1.1 THE EMPIRICAL MODE DECOMPOSITION PROCESS

The *empirical mode decomposition* assumes that a signal is composed by the superimposition of different coexisting modes. These *intrinsic mode functions* (IMFs), in general not strictly orthogonal, represents a simple oscillation. Each IMF oscillatory mode is variable with time in both amplitude and frequency; the following properties characterize an IMF:

- the number of extrema and the number of zero crossings differ at most by one

- the mean value of the envelopes defined by the local maxima and the local minima is zero

The first extracted IMF contains the highest frequencies of the signal; each subsequent IMF is described by lower frequency components.

The signal is decomposed into IMFs with a *sifting process*.

A discretely sampled signal $x(t)$ is considered. The cubic spline connection of the all local maxima defines the local extrema $x_{max}(t)$ (upper envelope); the same process is used for the local minima $x_{min}(t)$ (lower envelope). These envelopes include the all data. The mean value of the spline is expressed as:

$$m(t) = \frac{x_{max}(t) - x_{min}(t)}{2} \tag{B.1}$$

Once defined the $m(t)$, it is possible to evaluate the $h(t)$ component as:

$$h(t) = x(t) - m(t) \tag{B.2}$$

If the obtained $h(t)$ does not correspond to the criteria that defines an IMF, the sifting has to be repeated; for the next step, $h(t)$ is treated as original data. If it does, the IMF is defined as:

$$IMF_n(t) = h_{nk}(t) = h_{n(k-1)}(t) - m_{nk}(t) \tag{B.3}$$

One of the sifting stop criterion is based on the choice of a pre-selected S-number; the sifting process is stopped after S consecutive times. The selection of S number is *ad hoc*; a typical number of iterations is $S = 4 - 8$.

Once that the IMF_n is obtained, it is separated by the signal and the first residual is evaluated:

$$r_n = x(t) - IMF_n \tag{B.4}$$

r_n is treated as the new data subjected to the sifting process. This procedure is repeated until the residual r_N contains useful frequency informations; the last r_N is a monotonic function from which no more IMF can be extracted.

The original signal can be then expressed as a function of the N IMF and of the final residual r_N:

$$x(t) = \sum_{n=1}^{N} IMF_n(t) + r_N(t) \tag{B.5}$$

B.1.2 THE HILBERT TRANSFORM

The second step of the HHT analysis is the extraction from each IMF of the frequency and the amplitude.

The computation of the Hilbert transform is a convolution of 1/t with an IMF, $x(t)$. This operation emphasizes the local properties of $x(t)$, preserving the signal time structure of both amplitude and frequency.

For any real valued function $x(t)$, the complex conjugate $y(t)$ can be determined by:

$$y(t) = H[x(t)] = \frac{1}{\pi} PV \int_{-\infty}^{\infty} \frac{x(\tau)}{t-\tau} d\tau \tag{B.6}$$

where the PV is the principal value of the singular integral.

So the analytical signal can be expressed as:

$$z(t) = x(t) + i\, y(t) = A(t) e^{i\, \theta(t)} \tag{B.7}$$

where $A(t)$ is the instantaneous amplitude and θ is the phase function. The instantaneous frequency is expressed as:

$$f = \frac{d\theta}{dt} \tag{B.8}$$

B.1.3 THE HILBERT SPECTRAL ANALYSIS

The Hilbert transform is applied to each IMF.

The original data can be expressed as:

$$x(t) = \Re \left[\sum_{j=1}^{n} A_j(t)\, e^{i \int f_j(t) dt} \right] \tag{B.9}$$

that for each component gives both the amplitude and the frequency as a function of the time. The frequency-time distribution of the amplitude is designed as the *Hilbert spectrum* $H(f,t)$.

The IMF represents a generalized Fourier expansion. The amplitude and the instantaneous frequency allows to consider nonlinear and non stationary data; further, the amplitude and frequency modulations are clearly separated.

C

Numerical simulation results for non resonant condition

The results presented in the 5 chapter only describe the resonant conditions obtained by AGAR simulation of the P80 SRM.

In this appendix, the results that describe a non resonant configuration are presented. The non-resonant phase occurring at ~ 5 s is here considered and it can be seen in fig. C.1.

The frequency of vortex detachment does not reach a constant value, as shown in fig. C.2, where each vortex separation is underlined by a red line. Moreover, the detached vortices are characterized by different dimensions, as visible in fig. C.3.

Pressure, velocity, sound velocity and Mach number combustion chamber distributions do not show any sensible difference with respect to the resonant case (fig. C.4). Some irregular behavior can instead be seen in pressure and velocity time derivative distributions (fig. C.5).

The vorticity (Ω) distribution clearly underlines a non resonance configuration, fig. C.6; it loses the regular envelopment seen for the resonant cases.

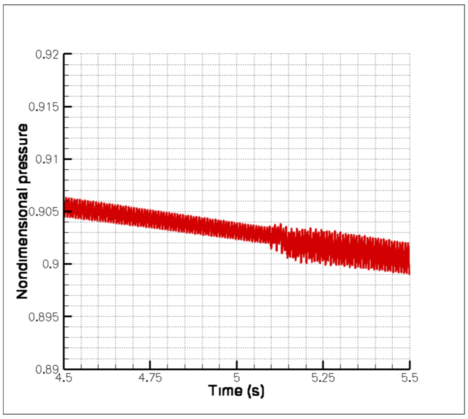

Figure C.1: Nondimensional head pressure.

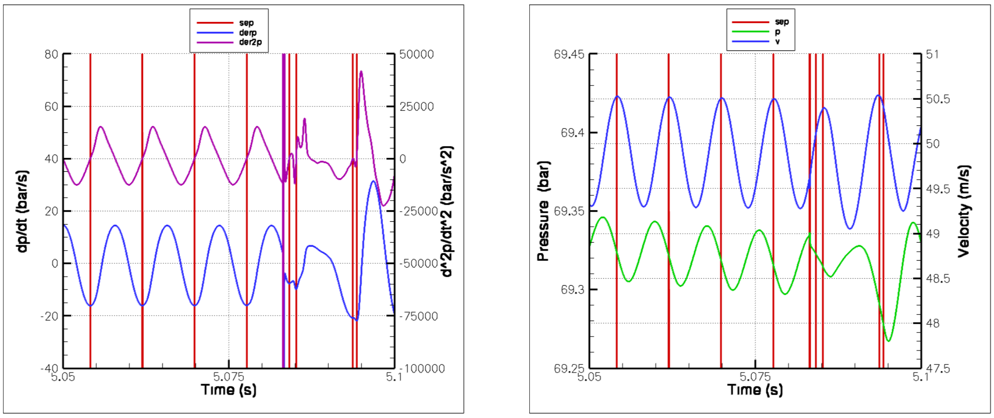

(a) Pressure time derivatives.

(b) Pressure and velocity.

Figure C.2: Vortex detachment conditions.

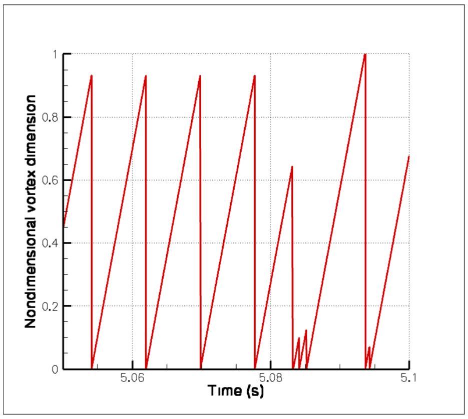

Figure C.3: Non dimensional vortex dimension.

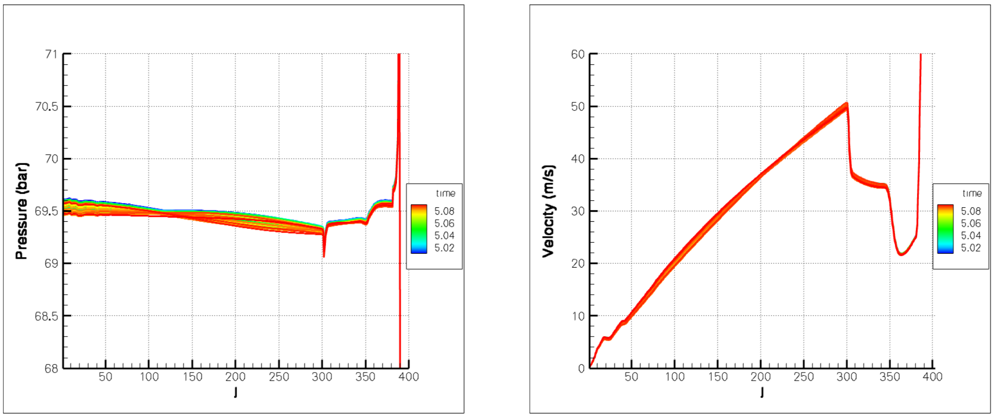

(a) Pressure.
(b) Velocity.

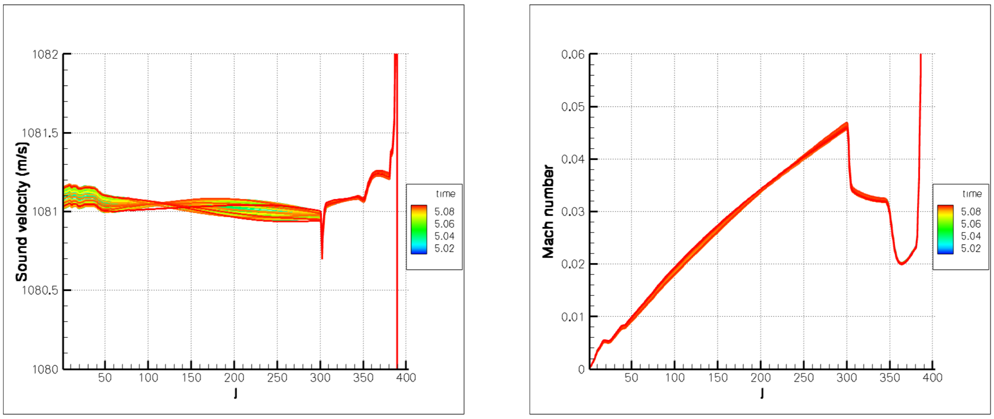

(c) Sound velocity.
(d) Mach number.

Figure C.4: Combustion chamber distributions.

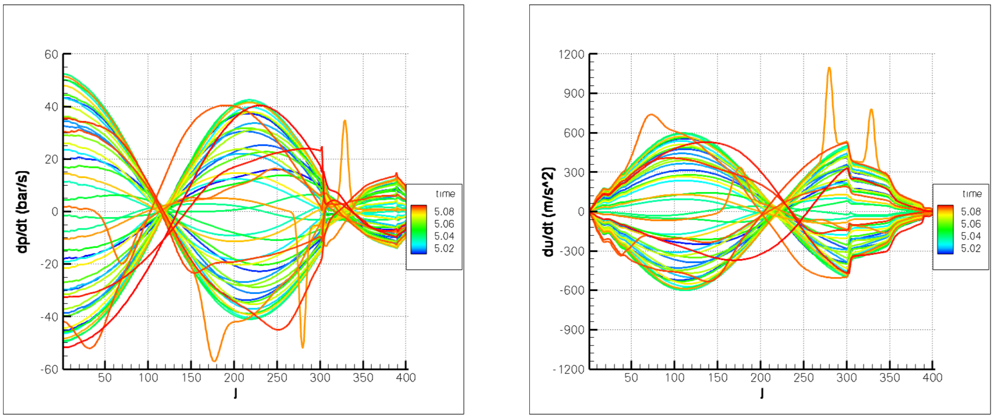

(a) Pressure derivative.

(b) Velocity derivative.

Figure C.5: Pressure and velocity time derivative distributions.

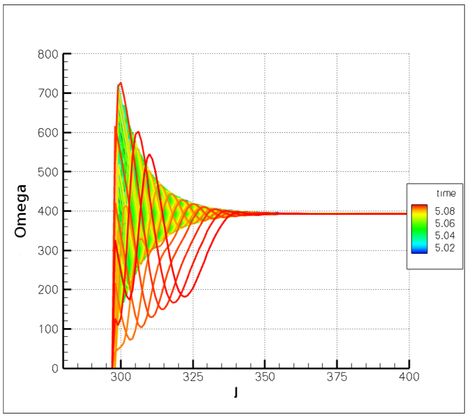

Figure C.6: Vorticity (Ω) distribution.

BIBLIOGRAPHY

[1] Anderson. *Fundamentals of Aerodynamics*. McGraw-Hill, 2001.

[2] Anthoine, J. *Experimental and numerical study of aeroacoustic phenomena in large solid propellant boosters*. PhD thesis, Universite libre de Bruxelles-von Karman institute, 2000.

[3] Anthoine, J., Buchlin, J. M., and Guery, J. F. Experimental and numerical investigations of nozzle geometry effect on the instabilities in solid propellant booster. *AIAA Paper 2000-3560*, 2001.

[4] Anthoine, J., Buchlin, J. M., and Hirschberg, A. Theoretical modelling of the effect of the nozzle cavity volume on the resonance level in large solid rocket motors. *AIAA Paper 2001-2102*, 2001.

[5] Anthoine, J., Buchlin, J. M., and Hirschberg, A. Effect of nozzle cavity on resonance in large SRM: theoretical modeling. *Journal of propulsion and power*, 18, 2002.

[6] Anthoine, J., Mettenleiter, M., Repellin, O., Buchlin, J.-M., and Candel, S. Influence of adaptive control on vortex-driven instabilities in a scaled model of solid propellant motors. *Journal of sound and vibration*, 262, 2003.

[7] Arnald, D., Habiballah, M., and Coustols, E. Théorie de l'instabilité laminaire et critères de transition en écoulement bi et tri dimensionnel. *La Recherche Aérospatiale*, 1984-2, 1984.

[8] Auregan, Y., Maurel, A., and Pagneux, V. *Sound-flow interactions*. Springer, 2002.

[9] Avalon, G. Etudes expérimental des instabilités naturelles d'un écoulement avec injection a la paroi. campagne d''essais vecla assm7. March 1999. Rapport Technique no. 4/6163 DSNA/Y/DEFA.

[10] Ballereau, S., Godfroy, F., Guery, J. F., and Ribereau, D. Assessment on analysis and prediciton method applied on thrust oscillations of Ariane 5 Solid Rocket Motor. *AIAA Paper 2003-4675*, 2003.

[11] Ballereau, S., Godfroy, F., Orlandi, O, and Ballion, D. Numerical Simulations and Searching Methods of Thrust Oscillations for Solid Rocket Boosters. *AIAA Paper 2006-4425*, 2006.

[12] Betchov, R. and Criminal, W. O. Stability of parallel flow. Academic, New York, 1967.

[13] Blevins, R. D. *Flow-induced vibrations*. Van Nostrand, New York, 1977.

[14] Brooks, K. P. and Beckstead, M. W. Dynamics of aluminum combustion. *Journal of Propulsion and Power*, 11(4), 1995.

[15] Brown, R. S., Blackner, A. M., Willoughby, P., and Dunlap, R. Vortex-generated sound in cavities. *AIAA Paper 86-0531*, 1986.

[16] Brown, R. S., Dunlap, R., Young, S. W., and Waugh, R. C. Vortex shedding as a source of acoustic energy in segmented solid rockets. *Journal of Spacecraft*, 18(4), 1981.

[17] Bruggeman, J. C., Hirschberg, M. E. H., van Dongen, A. P. J., and Gorter, J. Flow induced pulsations in gas transport systems: analysis of the influence of closed side branches. *Journal Fluids Engeeniring*, 111, 1986.

[18] Casalis, G., Avalon, G., and Pineau, J. Spatial instability of planar channel flow with fluid injection through porous wall. *Physics of Fluids*, 10:2558, 1998.

[19] Cavallini, E. *Modeling and numerical simulation of solid rocket motor internal ballistic*. PhD thesis, Dipartimento di Ingegneria Aerospaziale e Astronautica, Sapienza, Università di Roma, 2009.

[20] Cavallini, E., Favini, B., Di Giacinto, M., and Serraglia, F. Srm internal ballistic numerical simulation by spinball model. *AIAA Paper 2009-5512*, aug 2009. 45^{th} AIAA/ASME/SAE/ASEE Joint Propulsion Conference & Exhibit, 2-5 August 2009, Denver, Colorado.

[21] Cavallini, E., Favini, B., Di Giacinto, M., and Serraglia, F. Internal ballistics simulation of nawc tactical motors with spinball model. *AIAA 2010-7136*, July 2010. 46^{th} AIAA/ASME/SAE/ASEE Joint Propulsion Conference & Exhibit, 25-28 July 2010, Nashville, TN.

[22] Cavallini, E., Favini, B., Di Giacinto, M., and Serraglia, F. Srm q1d unsteady internal ballistics simulation using 3d grain burnback. *Space Propulsion 2010*, 2010. 3-6 May, San Sebastian, Spain.

[23] Chu, B.-T. and Kovasznay, L. S. G. Nonlinear interactions in a viscous heat-conducting compressible gas. *Journal of fluid mechanics*, 3, 1958.

[24] Clements, R. R. An inviscid model of two dimensional vortex shedding. *Journal of Fluid Mechanics*, 57, 1973.

[25] Couton, D., Plourde, F., and Doan, S. Analysis of energy transfers of a sheared flow generated by wall injection. *Experiments in Fluids*, 26(3), 1999.

[26] Culick, F. E. C. Acoustic oscillations in solid propellant rocket chambers. *Astronautica Acta*, 12(2), 1966.

[27] Culick, F. E. C. Rotational axissymmetric mean flow and damping of acoustic waves in a solid propellant rocket. *AIAA Journal*, 4, 1966.

[28] Culick, F. E. C. The stability of one dimensional motions in a rocket motor. *Combustion Science and technology*, 7, 1973.

[29] Culick, F. E. C. Combustion instabilities in propulsion system. *proceedings of the NATO Advanced Study Instituteon unsteady cmbustion*, 1993.

[30] Culick, F. E. C. and Magiawala, K. Exitation of acoustic modes in chamber by vortex shedding. *Journal of Sound and Vibration*, 64(3), 1979.

[31] Delprat, N. Rossiter's formula: A simple spectral model for a complex amplitude modulation process? *Physics of fluids*, 2006.

[32] Di Giacinto, M. and Serraglia, F. Modeling of solid motor start-up. *AIAA Paper 2001-3448*, 2001. 37^{th} AIAA/ASME/SAE/ASEE Joint Propulsion Conference, Salt Lake City, UT.

[33] Di Giacinto, M. and Serraglia, F. Modeling of srm ignition transient: Role of the main phenomena. *AIDAA*, 2001. XVI Congresso Nazionale AIDAA, Palermo, Italy.

[34] Dotson, K. W., Koshigoe, S., and Pace, K. K. Vortex shedding in a large solid rocket motor without inhibitors at the segment interfaces. *Journal of propulsion and power*, 13(2), 1997.

[35] Dunlap, R. and Brown, R. S. Exploratory experiments on acoustic oscilaltions driven by periodic vortex shedding. *AIAA Journal*, 19(3), 1981.

[36] Dupays, J., Godfroy, F., Orlandi, O., Prevot, P., Prévost, M., Gallier, S., Ballereau, S., and Fabignon, Y. Inert condensed phase driving effect of combustion instabilities in solid rocket motor. *AAAF*, 2008.

[37] Favini, B., Cavallini, E., Di Giacinto, M., and Serraglia, F. An Ignition-to-Burn Out Analysis of SRM Internal Ballistic and Performances. *44th AIAA/ASME/SAE/SEE Joint Propulsion Conference & Exhibit*, 21-23 July 2008, Hartford, Connecticut.

[38] Favini, B., Di Giacinto, M., and Serraglia, F. Solid rocket motor ignition transient revisited. *Proc. of the* 8^{th} *Int. Workshop on Combustion and Propulsion*, 2002. Pozzuoli, Italy.

[39] Favini, B., Serraglia, F., and Di Giacinto, M. Modeling of flowfield features during ignition of solid rocket motors. *AIAA Paper 2002-3753*, 2002. 38^{th} AIAA/ASME/SAE/ASEE Joint Propulsion Conference, Indianapolis, Indiana.

[40] Feraille, T. Instabilitiés de l'écoulement interne des moteurs à propergol solide. *Thesis, ENSAE*, 2004.

[41] Ferretti, V. and Favini, B. Pox q-1-d modeling of srm aeroacoustic. Technical report, Internal Report for ESA-ESRIN, Frascati, Italy, 2009.

[42] Ferretti, V., Favini, B., Cavallini, E., Serraglia, F., and Di Giacinto, M. Quasi 1-D modeling of SRM aeroacoustics. Space Propulsion Conference, 2010, San Sebastian, Spain.

[43] Ferretti, V., Favini, B., Cavallini, E., Serraglia, F., and Di Giacinto, M. Numerical simulations of acoustic resonance of Solid Rocket Motor. *AIAA-2010-6996*, 2010. 46th AIAA/SAE/ASME/ASEE Joint Propulsion Conference and Exhibit, Nashville, TN, July 25-28, 2010.

[44] Flandro, G. A. AGARD consulting mission to ONERA, 1986.

[45] Flandro, G. A. Vortex driving mechanism in oscillatory rocket flows. *Journal of Propulsion and Power*, 2(3), 1986.

[46] Flandro, G. A. and Jacobs, H. R. Vortex-generated sound in cavities. *AIAA Paper 73-1014*, 1973.

[47] Flatau, A. and Van Moorhem, W. Prediction of vortex shedding responses in segmented solid rocket motors. *AIAA Paper 90-2073*, 1990.

[48] Flechter, N. H. and Rossing, T. *The physics of musical instruments*. Springer-Verlag, 1998.

[49] E. Gizzi. Il fenomeno aeroacustico negli endoreattori a propellente solido. Master's thesis, Università di Roma La Sapienza, 2009.

[50] J. Griffond. Instabilité pariétale et accrochage aéroacoustique dan les conduits à parois débitantes simulant les moteurs à propergol solide d'ariane 5. Master's thesis, ENSAE, 2001.

[51] Hart, R. W. and McClure, F. T. Theory of acoustic instability in solid propellant rocket combustion. *10th International symposiumon combustion, The combustion Inst.*, 1965.

[52] Hirschberg, A. and Rienstra, S. W. *An Introduction to Acoustic*. Eindhoven University of Technology, 2004.

[53] Hirshberg, A., Hulshoff, S., van Hassel, R. R., and Anthoine, J. Vortex-acoustic interaction in internal flow: the whistler-nozzle, human whistling and the solid propellant rocket motor. In *Proceedings of the 3th colloque ReT CNES-ONERA, Ecoulement internes en propulsion solide*, 1998.

[54] Hourigan, K., Welsh, M. C., and Thompson, M. C. Aerodynamic sources of acoustic resonance in a duct with baffles. *Journal of Fluids and Structure*, 4, 1990.

[55] Howe, M. S. Contributions to the theory of aerodynamic sound, with application to excess jet noice and the theory of the flute. *Journal of Sound and Vibration*, 71, 1975.

[56] Howe, M. S. The dissipation of sound at an edge. *Journal of Sound and Vibration*, 70, 1980.

[57] Howe, M. S. On the absorption of sound by turbulence and other hydrodynamic flows. *Journal of Applied Mathematics*, 32, 1985.

[58] Howe, M. S. Acoustics of fluid-structure interactions. Cambridge University Press, 1998.

[59] Huang, X. Y. and Weaver, D. S. On the active control of shear layer oscillations across a cavity in the presence of pipeline acoustic resonance. *Journal of Fluids and Structures*, 5, 1991.

[60] Hulshoff, S. J., Hirschberg, A., and Hofmans, G. C. Sound production of vortex-nozzle interactions. *Journal of Fluids Mechanics*, 439, 2001.

[61] Hulshoff, S. J., Hoeijmakers, H. W. M, and Mulder, J. A. Prediction of aircraft longitudinal response using time-accurate Euler computation. *AIAA paper 1996-2485*, 1996.

[62] Hussain, F. A. K. M. Coherent structures and turbulence. *Journal of Fluids Mechanics*, 173, 1997.

[63] Jou, W. H. and Menon, S. Modes of oscillation in a nonreacting ramjet combustor flow. *Journal of Propulsion and Power*, 6(5), 1990.

[64] Kourta, A. Instability of Channel Flow with Fluid Injection and Parietal Vortex Shedding.

[65] Kourta, A. Vortex shedding in segmented solid rocket motors. *Journal of Propulsion and Power*, 12(2), 1996.

[66] Kourta, A. Shear layer instability and acoustic interaction in solid propellant rocket motors. *Interational Journal of Numerical Fluid Mechanics*, 25, 1997.

[67] Krasny, R. Computation of vortex sheet roll-up in the Treffetz plane. *Journal of Fluid Mechanics*, 184, 1987.

[68] Kuentzmann, P. Combustion instabilities. AGARD LS 180, 1991.

[69] Lighthill. On Sound Generated Aerodynamically, I. *Proc. Roy. Soc. A*, Vol. 211, 1952, pp 564-587, 1952.

[70] Lighthill. On Sound Generated Aerodynamically, II. *Proc. Roy. Soc. A*, Vol. 222, 1954, pp 1-32, 1954.

[71] Lin, C. C. The theory of hydrodynamic stability. Cambridge Univ. Press., Cambridge, England, 1955.

[72] Lugt, H. J. *Vortex Flow in Nature and Technology*. Wiley, 1983.

[73] Lupoglazoff, N. and Vuillot, F. Analyse du vortex shedding par simulation numérique 2D dans un propulseur solide et calculus de pousée instationnaire. Colloque CNES-ONERA,Châtillon, 1992.

[74] Lupoglazoff, N. and Vuillot, F. Numerical simulation of vortex shedding phenomenon in 2D test case solid rocket motors. *AIAA Paper 92-0776*, 1992.

[75] Lupoglazoff, N. and Vuillot, F. Simulation numerique bidimensionelle des ecoulements instationnaires dans les propulseurs a propergol solide. *La Recherche Aerospatiale*, 1992-2, 1992.

[76] Lupoglazoff, N. and Vuillot, F. Comparison between firing tests and numerical simulation of vortex shedding in 2D test solid rocket motor. *AIAA Paper 93-3066*, 1993.

[77] Mason, D. R., Folkman, S. L., and Behring, M. Thrust oscillations of the Space Shuttle solid rocket booster motor durinf static test. *AIAA Paper 79-1138*, 1979.

[78] Matveev, K. I. Reduced-oder modeling of vortex-driven excitation of acoustic modes. Acoustic research letters online, 2004.

[79] Matveev, K. I. Vortex -acoustic instability in chambers with mean flow and heat release. Technical acoustics, 2004.

[80] Matveev, K. I. and Culick, F. E. C. A model for combustion instability involving vortex shedding. *Combust. Sci. and Tech.*, 175, 2003.

[81] Menon, S. and Jou, W.-H. Numerical simulations of oscillatory cold flows in an axisymmetric ramjet combustor. *Journal of Propulsion*, 6, 1990.

[82] Michalke, A. The instability of free shear layers: a survey on the state of art. *Progress in aerospace Sciences*, 12, 1972.

[83] Nesman, T. RSRM - Chamber pressure oscillations: full scale ground and flight test summary and air flow test results. In *Proceedings of the AIAA/SAE/ASME/ASEE Solid rocket motor combustion instability workshop, 31st Joint Propulsion Confence*. AIAA Solid rocket technical committee, AIAA, 1995.

[84] Nomoto, H. and Culick, F. E. C. An experimental investigation of pure tone generation by vortex shedding in a duct. *Journal of Sound and Vibration*, 84(2), 1982.

[85] Powell, A. Theory of vortex sound. *Journal of Acoustical Society of America*, 36(1), 1964.

[86] Price, E. W. Comments on the role of aluminum in suppressing instability in solid propellant rocket motors. *AIAA Journal*, 9(5), 1971.

[87] Prévost, M., Vuillot, F., and Traineau, J. C. Vortex shedding driven scilations in a subscale motor for the Ariane 5 MPS solid rocket motors. *AIAA 96-3247*, 1996.

[88] Rienstra, S. W. and Hirschberg, A. *An Introduction to Acoustic*. Eindhoven University of Technology, 2006.

[89] S. K. Robinson. A review of vortex structures and associated coherent motions in turbolent boundary layer. *Proceedings of the second IUTAM symposium on structural turbulence and drag reduction*, Zurich, 1989.

[90] Rossiter, J. E. The effect of cavities on the buffeting of aircraft. Royal Arircraft Establishment, Technical memo, 1962.

[91] Rossiter, J. E. Wind tunnel experiments on the flow over a rectangular cavities at subsonic and transonic speeds. Aeronautical research council, Ministry of Aviation, Reports and memoranda 3438, 1964.

[92] Schachemann, A. and Rockwell, D. Self-sustained oscillations of turbulent pipe flow terminated by an axisymmetric cavity. *Journal of Sound and Vibration*, 73(1), 1980.

[93] Scippa, S., Pascal, P., and Zanier, F. Ariane 5 - MPS - Chamber pressure oscillations full scale firing results analysis and further studies. *AIAA Paper 94-3068*, 1994.

[94] Serraglia, F. *Modeling and numerical simulation of ignition transient of large solid rocket motors*. PhD thesis, Scuola di Ingegneria Aerospaziale, La Sapienza, Università di Roma, 2003.

[95] Summerfield, M. and Krier, H. Role of aluminum in suppressing instability in solid propellant rocket motors. *Problems of hydrodynamics and continuum mechanics*, 1969. Sixtieth anniversary volume, Society for indipendent and applied mathematics.

[96] Sutton, G. P. and Ross, D. M. *Rocket Propulsion Element*. Wiley and Sons, 1976.

[97] Temkin, S. and Dobbins, R. A. Attenuation and sispersion of sound particle-relaxation processes. *Journal of the acoustical society of america*, 40(2), 1966.

[98] M. Tennenini. Oscillazioni di pressione nei motori a propellente solido. Master's thesis, Iniversità di Roma, La Sapienza, 2010.

[99] Tissier, P. Y., Godfroy, F., and Jaquemin, P. Simulation of three dimensional flows inside solid rocket motors using a second order finite volume method - Application to the study of unstable phenomena. *AIAA Paper 92-3275*, 1992.

[100] Traineau, J. C., Prevost, M., Vuillot, F., Le Breton, P., Cuny, J., Preioni, N., and Bec, R. A subscale test program to assess the vortex shedidng driven instabilities in segmented solid rocket motors. *AIAA Paper 97-3247*, 1997.

[101] B. Ugurtas. Etudes numérique et espérimentale des instabilités hydrodynamiques et du couplage aéro-acoustique dans un écoulement de taylor. Thesis dissertation, Paris, 2000.

[102] Varapaev, V. N. and Yagodkin, V. I. Flow stability analysis in a channel with porous wall. *Izvetiya Akademii Nauk SSSR, Mekhanika Zhidkosti i Gaza*, 4(5), 1969.

[103] Verge, M. P., Causé, R., Fabre, B., Hirschberg, A., Wijnands, A. P. J., and Steenbergen, A. Jet oscillations and jet drive in recorder-like instruments. *Acta Acustica*, 2, 1994.

[104] Vuillot, F. Vortex-shedding phenomena in solid rocket motors. *Journal of Propulsion and Power*, 11(4), 1995.

[105] Vuillot, F. and Casalis, G. Internal aerodynamics in solid rocket propulsion, Motor flow instabilities - Part 1. RTO AVT/VKI Special Course, 2002.

[106] Vuillot, F., Lupoglazoff, N., Prevost, M., and Traineau, J. Improved modelisation for numerical simulation of oscillatory solid rocket motors. In *Proceedings of the AIAA/SAE/ASME/ASEE Solid rocket motor combustion instability workshop, 31st Joint Propulsion Conference*. AIAA Solid rocket technical committee, AIAA, 1995.

[107] Vuillot, F., Traineau, J., Prevost, M., and Lupoglazoff, N. Experimental validation of stability assessment methods for segmented solid propellant motors. *AIAA Paper 93-1883*, 1993.